

Brunnhilde Ponsi

Development of a realistic human spine phantom to mimic static B_0 field inhomogeneity in the cervical spinal cord

Master's thesis in Master of Science in Physics (MSPHYS)

Supervisor: Johanna Vannesjo

Co-supervisor: Laura Beghini

May 2023



Brunnhilde Ponsi

Development of a realistic human spine phantom to mimic static B_0 field inhomogeneity in the cervical spinal cord

Master's thesis in Master of Science in Physics (MSPHYS)
Supervisor: Johanna Vannesjo
Co-supervisor: Laura Beghini
May 2023

Norwegian University of Science and Technology
Faculty of Natural Sciences
Department of Physics



Summary

Background: Magnetic resonance imaging (MRI) is a powerful imaging technique that offers superior soft tissue contrast compared to other techniques used in the clinical practice. Innovation in MRI requires frequent testing, commonly done scanning homogeneous phantoms, especially at an early stage. These phantoms, however, fail to represent the challenges encountered in vivo. For instance, magnetic susceptibility differences across tissues lead in vivo to field inhomogeneities causing signal loss in the images. This is particularly true for spinal cord imaging at 7T where data are heavily affected by B_0 field inhomogeneity, due to susceptibility difference between the vertebrae and the surrounding tissues. Slice-wise shimming techniques have been proposed to reduce the distortion and signal drop-out but substantial artifacts typically persist. An anthropomorphic MRI phantom of the human cervical spine mimicking the static B_0 field distribution could then be used to optimize advanced shimming and acquisition techniques for 7T spinal cord MRI.

Methods: An initial phantom prototype consisting of 3D printed vertebrae C3-to-C5 in a spherical container was built. Various ingredients and printing materials were tested to tune the susceptibility difference between the vertebrae and the solution, along with the relaxation time T_2^* of the solution. Subsequently, a more advanced phantom version was developed, consisting of a 3D printed phantom shell in the shape of a human head and thorax containing vertebrae from C1 to C7. Field maps and gradient echo (GRE) multi-echo sequences of the phantoms were acquired at 7T on a Siemens MAGNETOM Terra System.

Results: The phantom components approximately matched the in vivo susceptibility difference between the vertebrae and surrounding tissues, as well as the spinal cord T_2^* value. Measured field maps of the phantom were compared with field simulations, showing similar features in the field distortion. The phantom also exhibited a spatially periodic pattern of signal drop-out around the intervertebral junctions in multi-echo GRE images, similar to what is commonly observed in in vivo data. The signal drop-out arises in regions with higher field inhomogeneities.

Conclusion: This phantom demonstrates the feasibility of 3D printing an adaptable, non-toxic anthropomorphic phantom that accurately reproduces B_0 field patterns from the spine and may serve to test new acquisition strategies and post-processing strategies to address the persistent challenge of static B_0 field distortion in spinal cord imaging.

Sammendrag

Bakgrunn: Magnetisk resonanstomografi (MR) er en effektiv avbildningsteknikk som gir overlegen kontrast i bløtvev sammenlignet med andre teknikker som brukes i klinisk praksis. Nye metoder innen MR krever hyppig testing, og særlig tidlig i utviklingsprosessen blir denne testingen vanligvis gjennomført ved skanning av homogene fantomer. Disse fantomene fanger imidlertid ikke opp utfordringene som oppstår in vivo. For eksempel kan forskjeller i magnetisk susceptibilitet på tvers av vev in vivo føre til feltinhomogeniteter, som videre kan forårsake signaltap i bildene. Dette gjelder spesielt for ryggmargsavbildning ved 7T, hvor data er sterkt påvirket av B_0 feltinhomogenitet, grunnet susceptibilitetsforskjeller mellom ryggvirvlene og det omkringliggende vevet. “Slice-wise shimming”-teknikker har blitt foreslått for å redusere signalforvrengning og signaltap, men disse fjerner vanligvis ikke framtrepende signalartefakter. Et antropomorft MR-fantom av den menneskelige cervicalcolumna som etterligner den statiske B_0 feltfordelingen, kan deretter brukes til å optimalisere avanserte shimming- og innhentingsmetoder for 7T MR-avbildning av ryggmargen.

Metoder: En første fantomprototype bestående av 3D-printede ryggvirvler C3 til C5 ble bygget og plassert i en sfærisk beholder. Ulike ingredienser og produksjonsmaterialer ble testet for å finjustere følsomhetsforskjellen mellom ryggvirvlene og løsningen, i tillegg til løsningens relaksasjonstid T_2^* . Deretter ble en mer avansert fantomversjon utviklet, bestående av et 3D-printet fantomskall i form av et menneskehode og thorax med ryggvirvler fra C1 til C7. Feltkart og gradient ekko (GRE) multi-ekkoekvenser av fantomene ble kartlagt ved 7T på et Siemens MAGNETOM Terra System.

Resultater: Det ble observert en omtrentlig samsvar mellom fantomkomponentene, in-vivo følsomhetsforskjellen mellom ryggvirvlene og omkringliggende vev, og ryggmargens T_2^* -verdi. Observerte feltkart av fantomet ble sammenlignet med feltsimuleringer, der disse presenterte lignende trekk med hensyn til egen feltforvrengning. Fantomet viste også et rommessig periodisk mønster av signaltap rundt de intervertebrale kryssene i multi-ekko GRE-bildene, i likhet med det som ofte observeres i in vivo-data. Signaltapet oppsto i områder med høyere feltinhomogenitet.

Konklusjon: Dette fantomet viser at det er mulig å 3D-printe et tilpasningsdyktig, ikke-toksisk antropomorft fantom som nøyaktig gjengir B_0 -feltmønstre fra ryggraden og kan benyttes til å teste nye anskaffelsesstrategier og etterbehandlingsstrategier for å løse den vedvarende utfordringen med statisk B_0 -feltforvrengning i ryggmargsavbildning.

Preface and Acknowledgments

I am pleased to present my master's thesis, completed during the academic year of 2022-2023, within the Department of Physics at NTNU. This thesis aimed to build an anthropomorphic MRI phantom that would reproduce the static B_0 field inhomogeneities in spinal cord imaging.

But before all, I would like to thank these people without whom nothing would have been possible:

I would like to express my sincere gratitude to my supervisor Prof. Johanna Vannesjo for her support, expert advice, and guidance throughout this project. I am especially grateful for the trust she placed in me by giving me the opportunity to write an abstract, and for the extra time she dedicated to helping me. Thank you, Johanna, for your mentorship and belief in my potential.

I would also like to thank Laura for her dedication to help me throughout this year and this master's thesis. Thank you for encouraging me when I didn't have confidence in myself, thank you for taking the time to answer and support me, both professionally and personally, and even outside working hours. Finally, thank you for having been not only my co-supervisor, but also my friend.

I then need to thank Annelen for the work she did last year, and for allowing me to read her master's thesis, which was of great assistance to me in understanding the fundamentals of MRI.

I would like to say thank you to Jan-Magne, for his printing work, and for the time and attention to detail he brought to our reflections, always ready to help find solutions.

Then, I want to thank Marc-Antoine for his advice, his calm, his sense of humor and for all the conversations in French that may have enraged Laura.

I thank Pierre, who supported me, helped me, advised me with his PhD experience, encouraged me, scolded me when I grumbled too much, and who never stopped believing in me.

Thank you to Le Moulin, which has made my life during this year noisy, animated, sometimes explosive but never boring.

Finally, thank you to my family for their unconditional support. I love you.

Table of Contents

Summary	i
Sammendrag	ii
Preface	iii
Table of Contents	vii
List of Tables	ix
List of Figures	xiv
Abbreviations	xv
1 Introduction	1
2 Theory	3
2.1 Nuclear Magnetic Resonance and MRI basics	3
2.1.1 Introduction to MRI	3
2.1.2 Excitation Process	4
2.1.3 Relaxation Process	5
2.1.4 Bloch Equation	7
2.2 Spatial Encoding in MRI	7
2.2.1 Slice Excitation	7
2.2.2 Fourier Encoding	7
2.2.3 Spatial Conventions	8
2.3 Acquisition Sequences in MRI	9
2.3.1 Gradient-Echo (GRE)	10
2.3.2 Multi-Echo GRE (ME-GRE)	11
2.3.3 Spin-Echo (SE)	12
2.4 Magnetic Susceptibility	15
2.4.1 Definition	15
2.4.2 Magnetic Susceptibility Artifacts	15
2.4.3 Field-Mapping	16
2.4.4 Simulation of the Field Inhomogeneities	16
2.5 Spinal Cord Imaging	17
2.5.1 Anatomy and Function	17
2.5.2 High-Field MRI of the Spinal Cord	20

2.6	Correction of the Artifacts	20
2.6.1	Sequence and Parameters Optimization	20
2.6.2	B_0 Shimming	21
2.6.3	Slice-Wise Shimming	21
2.6.4	Post-Processing	21
2.7	Phantom Building (3D Printing)	21
2.7.1	General Principles and Benefits of 3D Printing	22
2.7.2	Advantages and Disadvantages of a 3D Printed Phantom Compared to a Cadav- eric One	22
2.7.3	Existing 3D Printed MRI Phantoms of the Cervical Spine	23
2.7.4	Doping Agents to Match Tissues Properties	23
3	Methods	25
3.1	Choice of the printing material	25
3.1.1	Experimental Set-up	25
3.1.2	Field Map Acquisitions and Analysis	26
3.2	Testing additives to the solution	28
3.2.1	Solution Ingredients and Experimental Set-ups	28
3.2.2	Field Maps Acquisitions and Analysis	29
3.2.3	Multi-Echo GRE Acquisitions and Analysis	30
3.3	Spherical phantoms	31
3.3.1	Building the Phantoms	31
3.3.2	Field Maps	32
3.3.3	Multiecho GRE acquisition	33
3.3.4	Signal loss comparison	34
3.4	Final C1 to T1 phantom	34
3.4.1	Building the Phantom	34
3.4.2	Field Map Acquisition and Analysis	37
3.4.3	Multi-Echo 2D GRE Acquisition and Analysis	37
4	Results	39
4.1	Choice of the printing material	39
4.1.1	Material and 3D printers	39
4.1.2	Field Map Analysis	39
4.2	Testing different additives to the solution	41
4.2.1	Field Map Acquisitions	41
4.2.2	Multi-Echo GRE Analysis and T_2^* Values	44
4.3	Spherical Phantoms	45
4.3.1	Building the Phantoms	45
4.3.2	Analysis of the Field Maps	46
4.3.3	Multi-Echo GRE Analysis	53
4.3.4	Signal Loss	56
4.4	Final C1 to T1 Phantom	57
4.4.1	Building the Phantom	57
4.4.2	Field Map Analysis	58
4.4.3	Multi-Echo GRE Analysis	63

5 Discussion	67
5.1 Phantom Design	67
5.1.1 Vertebrae Design	67
5.1.2 Shell Design	68
5.2 3D Printing Process	69
5.2.1 Printing of the Vertebrae	69
5.2.2 Printing of the Shell	70
5.3 Selection of Materials for Printing the Vertebrae	71
5.4 Shell Preparation	71
5.5 Tuning the Solution	72
5.6 Pre-Acquisition Preparations and Phantoms Set-ups	73
5.7 Analysis of the Data	74
5.7.1 Field Maps	74
5.7.2 Multi-echo GRE	76
5.8 Innovative Contributions of this Phantom	76
6 Future Work	79
7 Conclusion	81
Bibliography	83
Appendix	89

List of Tables

2.1	Comparison of the advantages and drawbacks of using a 3D printed phantom or a cadaveric phantom	23
3.1	Main characteristics of the tested 3D printing materials.	26
4.1	Susceptibility of the tested materials compared to water, found by linear regression with a Fourier-based simulation. The simulation was run on a perfect sphere with a higher resolution than what was acquired, and was then reshaped to obtain an array of similar dimensions. The slope a is used to calculate the susceptibility according to equation (3.1). R^2 is the correlation coefficient.	41
4.2	Susceptibility of Standard White Resin compared to the external solutions containing various amounts of soap, found by linear regression with a Fourier-based simulation. The simulation was run on a perfect sphere with a higher resolution than what was acquired, and was then reshaped to obtain an array of similar dimensions. The slope a is used to calculate the susceptibility according to equation (3.1). R^2 is the correlation coefficient.	42
4.3	Susceptibility of Standard White Resin compared to the external solutions containing various amounts of soap, found by linear regression with Fourier-based simulations. The simulations were run on a mask based on the magnitude of the images acquired in each case, defining each sphere using a threshold $s = 200$. The slope a is used to calculate the susceptibility according to equation (3.1). R^2 is the correlation coefficient.	42
4.4	Susceptibility difference $\Delta\chi$ of the eight tested solution compared to the external one, with their corresponding correlation coefficient.	44
4.5	Computed mean T_2^* values of the eight tested solutions and of the external solution. Each T_2^* value was calculated between voxels of one selected slice inside a circular ROI of radius $r = 10$ voxels centered in the middle of the examined tube, excluding all values with a coefficient of determination inferior to the chosen R_{min}^2 . The standard deviation, and the number and percentage of selected voxels inside the studied ROI are respectively given by Std, N_{R^2} and $N\%$	45
4.6	Mean T_2^* -value on one slice, and its associated standard deviation Std. The values were computed for $R^2 > R_{min}^2$	65

List of Figures

2.1	In the absence of a magnetic field, the spins of the nuclei are randomly oriented in space (a). But when a field B_0 is applied, they align in its direction, either parallel or antiparallel (b). Figure inspired from Dance (2014).	4
2.2	In the rotating reference frame, when applying a short RF pulse in the transverse plane, the net magnetization vector is tipped by an angle α from the longitudinal axis. After the application, \vec{M} slowly comes back to its equilibrium position while rotating around the z-axis at ω_0 . Due to the main B_0 field, only the transverse signal can be acquired. The detection of the oscillating M_{xy} signal is possible through a receiving coil in the transverse plane. The acquired signal is known as the Free Induction Decay (FID).	5
2.3	Illustration of the loss of phase coherence between the spins. As the dephasing increases, the transverse magnetization vector decreases (Fortin, 2021).	6
2.4	Orientation conventions. The sagittal plane is orthogonal to the x-direction, defined as the direction from the right (R) to the left (L) of the patient. The y-direction, from the anterior (A) to the posterior (P) part of the body, cut the y-direction. B_0 , from the feet to the head, follows the z-direction. The transverse plane is orthogonal to the inferior (I) - superior (S) direction.	9
2.5	Illustration of a basic GRE sequence.	10
2.6	In GRE sequences, to fill one line in k-space, the phase gradient and the prephase frequency gradient are applied simultaneously (lines in dots), before reading a line with the readout gradient. The blue and the red arrows are two examples of a line readout.	11
2.7	Illustration of a multi-echo GRE sequence. Multiple echoes can be acquired with only one excitation pulse. Each frequency readout is used as a prephase gradient for the next echo.	12
2.8	Illustration of a basic SE sequence.	13
2.9	Rephasing of the spins in SE. a) The first 90° RF-pulse flips the magnetization vector to the transverse plane. Right after the excitation, all the spins are synchronized. b) The spins then start to dephase due to both static and dynamic inhomogeneities. c) At $TE/2$, the 180° pulse inverses the order of the spins, decreasing the phase shift. d) The echo is finally acquired at TE , when all the spins are back together, and M_{xy} maximum.	14
2.10	The SE sequence is similar to the GRE sequence, except that a refocusing pulse is used instead of a refocusing gradient, resulting in a movement in k-space to the conjugate position.	14
2.11	Cross-section of the spine, in the cervical region (KindPNG.com, 2022). (a) Cross-section of the spinal cord and vertebra. (b) Light micrograph of cross-section through spinal cord (x8). The Grey Matter in the center, in light purple, is surrounded by the White Matter, in dark purple.	18

2.12	Regions of the spine (KindPNG.com).	19
3.1	Set up of the first experiment: choice of the printing material. The sphere of the material to be tested is hung by two threads in the center of a plastic sphere filled with water, salt and soap. The assembly is closed by a reusable IKEA silicon lid and a rubber band to ensure water-tightness.	26
3.2	Field map in hertz of PLA. The intersection of the red lines determines the center of the sphere. A line plot of the inhomogeneities in the three directions was then plotted, centered on this sphere. The line plots then describe the inhomogeneities along the red lines.	27
3.3	Set-up of the second experiment. The four tubes to be tested were inserted in a two-layer plastic film in the center of the plastic sphere, which was filled by a solution of salt, soap and distilled water.	29
3.4	Illustration of the determination of a mask. a) A threshold $s = 400$ was defined on the acquired magnitude image to extract b) a mask of the studied component.	30
3.5	Workflow of the first C3 to C5 phantom building from CT images to acquired data. In the second phantom, sugar and mouthwash were also added to the solution, and the lamp cover was covered with epoxy and fiberglass.	32
3.6	3D Slicer visualization of the segmented C1 to T1 vertebrae. The transversal (top left), coronal (bottom left) and sagittal (bottom right) are shown in addition to the resulting 3D model (top right).	34
3.7	The designed shell was divided into several parts as in a jigsaw puzzle. These parts were printed separately and then assembled and glued together by the online printing company.	35
3.8	Workflow of the final anthropomorphic phantom building from CT images and CAD to acquired data.	36
4.1	Comparison of the inhomogeneities of frequencies generated by the tested material samples along (a) horizontal axis, (b) vertical axis and (c) slice axis.	40
4.2	Field maps (Hz) of the eight tested solutions of mouthwash without (M_2) and with (M_1) alcohol, soap, various concentration of sugar, and the combined solution (Mix) of sugar, M_1 , and salt. The blank solution shows the effect of the plastic tube on the field.	42
4.3	Comparison of the field inhomogeneities generated in one slice of the tested solution of concentration C_1 of sugar and a simulated cylinder. The linear regression between those two slices is presented in a). c) represents the histogram of the error $f(x_i) - y$, with y the acquired value, and $f(x_i)$ the approximate linear value obtained from the simulation using the coefficients of the linear regression. The right part of the figure represents the slice of the field map in which the linear regression was run, for both the simulation (b) and the acquired field map (d).	43
4.4	(left) Exponential fit of the T_2^* -value in one voxel of the solution with a concentration C_1 of sugar. The voxel is given by the intersection of the blue lines in the representation of the first echo ($TE = 7.40$ ms) in the right.	45
4.5	Comparison of the quality of the spinal cord canal between two different printing orientation choices. In a), the C3 to C5 vertebrae were printed horizontally, to minimize the printing time, whereas in b), they were printed upright making it easier to access the support and remove it.	46
4.6	Original acquired FM of the first C3 to C5 phantom (a), and the various tested correction methods to remove the background inhomogeneities.	47

4.7	a) Linear regression between the simulated and measured data of the first phantom. The region of interest of the regression was chosen to be the voxels inside the volume defined by the yellow lines in both the sagittal (b) and transversal (d) planes, and which are not inside the vertebrae. c) gives the histogram of error between the linearly predicted $f(x_i)$ and measured data y	48
4.8	Comparison of the simulated and the measured field maps, in a sagittal slice. The simulated field map (a) was computed by assigning a susceptibility difference of 1 ppm between vertebrae and water. It was then rescaled to Hz using the susceptibility value difference between Standard White Resin and the external solution predicted with the analysis of the material in Section 4.1.2.2 . The acquired field map (b) is shown in Hz after background field correction. The values inside the vertebrae are masked.	49
4.9	a) Linear regression between the simulated and measured data of the second C3 to C5 phantom. b) and d) show the sagittal and transversal views of the simulated vertebrae in ppm. The region of interest of the regression was chosen to be the voxels inside the volume defined by the yellow lines in both the sagittal (b) and transversal (d) planes, which are not inside the vertebrae. c) gives the histogram of error between the linearly predicted and measured data.	50
4.10	Comparison of the simulated and the measured field maps of the second C3 to C5 phantom, in a sagittal slice. The simulated field map (a) was computed by assigning a susceptibility difference of 1 ppm between vertebrae and water. It was then rescaled to Hz using the susceptibility value difference between the vertebrae and the external solution found by linear regression between the acquired and simulated FMs, restricted to the spinal cord canal. The acquired field map (b) is shown in Hz after background field correction. The values inside the vertebrae are masked.	51
4.11	Comparison of local field gradients (upper part), and absolute values of the gradients (lower part) along the z-direction for both the simulated (left) and the measured (right) field maps. The simulated gradient has been rescaled to Hz/mm using the susceptibility value difference between Standard White Resin and the external solution predicted with the analysis of the material in Section 4.1.2.2	52
4.12	Comparison of local field gradients (upper part), and absolute values of the gradients (lower part) along the z-direction for both the simulated (left) and the measured (right) field maps of the second vertebral phantom.	53
4.13	Representative slices from an in vivo GRE acquisition (a,c), located mid-vertebra (a) and above an intervertebral junction (c) showing different patterns of signal drop-outs. Corresponding slice locations in the C3 to C5 first phantom (b,d) show increasing signal drop-out with increasing TE, resembling the in vivo pattern. For the phantom data, the difference to the first echo, acquired at $TE_1 = 7.40$ ms, is shown below the magnitude image for each echo. The last echo of the phantom data is shown in a sagittal view (e) demonstrating the periodicity of the signal drop-out.	54
4.14	Illustration of the evolution of the signal of the second phantom, on a transversal slice along the 12 evenly spaced echoes, from $TE_1 = 20.28$ ms to $TE_{12} = 80.00$ ms. The echoes are arranged in ascending order from left to right, row by row. The first one is in the top left corner, and subsequent images follow this order: top row second column, top row third column, top row fourth column, second row first column, and so on. All the echoes are scaled to the same colorbar presented on the right. The represented slice is situated in the top C5, similarly as the one presented in Fig. 4.13 d).	55
4.15	(a) Map of the T_2^* values of the external solution of the second spherical phantom, for one slice, and their associated coefficient of determination R^2 (b).	56

4.16	Comparison of the field gradient (a,b) with the ME-GRE loss (c). Three different transversal slices are shown: from top to bottom of the image, one can see a mid-C3/C4 slice, an upper C4 slice and a mid-C4/C5 slice. Their localization is shown in the sagittal view in a) by the three dotted red lines.	57
4.17	a) Final nylon printed vertebrae. In b), one can see the good quality of the printing. Contrary to the previous resin vertebrae, SLS printing allows having no support to remove, and thus no additional artifacts as observed in Fig. 4.5 . However, to guarantee the solidity of the structure and that the vertebrae were well attached to each other, some intervertebral attachment points were added by the printer (c). Two of them are shown in red.	58
4.18	Pictures of the final shell of the phantom. It is presented before (a) and after (b,c,d,e,f) the epoxy and fiberglass application.	59
4.19	Linear regression between the experimental and simulated field maps (a). The regression was run on the voxels inside the 3D area illustrated by the yellow frame in the sagittal and transversal slices b) and d). c) is the histogram of the error $f(x_i) - y$, with y the acquired value, and $f(x_i)$ the approximate linear value obtained from the simulation using the coefficients of the linear regression.	60
4.20	Simulated (left) and measured field maps, restricted to C3 to C1, and to C6 to C3. The simulated FM was computed in ppm by allowing a susceptibility value of 1 for the voxels inside the vertebrae, and 0 outside, and then rescaled to Hz using the slope of the linear regression. The values inside the vertebrae are masked.	61
4.21	Comparison of local field gradients (upper part), and absolute values of the gradients (lower part) along the z-direction for both the simulated (left) and the measured (right) field maps of the final cervical phantom, from C1 to T1. The simulated gradient was previously rescaled from ppm to Hz using the slope of the linear regression.	62
4.22	Three-color mask (a) of the magnitude of the acquired FM. Outside voxels have been assigned a value of zero, while $-\text{coeff}_{\text{air}} = -1$ was attributed to the voxels inside the vertebrae, and $-\text{coeff}_{\text{air}} - 1 = -2$ the voxels of the solution. The resulting simulated field map is shown in b). The acquired FM before correction is given in c) for comparison. In b) and c), values outside the shell, and inside the vertebrae are masked.	63
4.23	Representative transversal slices of the ME-GRE acquisition on the final phantom (a,b,c). The magnitude images are shown for three echo times, and the difference to the first echo, acquired at $\text{TE}_1 = 4.75$ ms, is shown below the magnitude image for each echo. The localization of the slices (mid-C2/low C1, upper C4 and mid-C5) is illustrated by the red dotted lines in the sagittal view in d). e) and f) are representative slices from an in vivo GRE acquisition, respectively located above an intervertebral junction (C3/C4) and mid-vertebra (mid-C3) showing different patterns of signal drop-outs.	64
4.24	(a) Map of the T_2^* values in the external solution of the final phantom, for one slice, and their associated R^2 (b). White voxels in the R^2 -map are voxels that generated an error in the computation of the T_2^* -value.	65
7.1	A small hole can be observed in the interior, posterior part of the C3 printed vertebrae in Standard White Resin. This imperfection remains sticky even after cleaning the vertebrae, suggesting that an accumulation of sugar is blocked in this area.	89

Abbreviations

BW	=	Bandwidth
CAD	=	Computed aided design
CSF	=	Cerebrospinal fluid
CT	=	Computed Tomography
FDM	=	Fused Deposition Modelling
FID	=	Free Induction Decay
FM	=	Field map
fMRI	=	functional MRI
GM	=	Grey Matter
GRE	=	Gradient-echo
ME-GRE	=	Multiecho Gradient-echo
MRI	=	Magnetic Resonance Imaging
PLA	=	Polylactic acid
qMRI	=	quantitative MRI
RF	=	Radio-frequency
ROI	=	Region of interest
SE	=	Spin-echo
SLA	=	Stereolitography
SLS	=	Selective Laser Sintering
UHF	=	Ultra-High Field
WM	=	White Matter

Introduction

Magnetic resonance imaging (MRI) is a non-harmful and non-invasive technique that, compared to other imaging techniques such as Computed Tomography (CT), does not imply any ionizing radiation (Dance, 2014). Since its emergence in the 1970s with the first images, MRI, which quickly became a key diagnostic and research technology, has experienced and continues to undergo tremendous growth and development (Le Bihan, 1985; Décorps, 2011) due to its superior soft tissue contrast. Apart from the conventional acquisition of qualitative and anatomical information, it is also possible to obtain structural or functional data through advanced imaging techniques such as functional Magnetic Resonance Imaging (fMRI) or quantitative Magnetic Resonance Imaging (qMRI).

MRI is based on the properties of the hydrogen proton. In their natural state, hydrogen atoms each have a spin randomly oriented in space. However, when subjected to a magnetic field B_0 , these spins align to form a magnetic moment. The application of a radio-frequency pulse can then tilt this vector to a transverse plane. After the pulse, the time the vector needs to return to its equilibrium position can be measured, giving rise to the MR-signal. This signal can then be spatially encoded by linear 3D gradients (Weishaupt et al., 2006; Dance, 2014).

One fundamental hypothesis of MRI is the homogeneity of the field. However, any object subjected to a magnetic field distorts this field locally, either positively (paramagnetic or ferromagnetic) or negatively (diamagnetic). The degree to which a material can become magnetized when exposed to a magnetic field is called susceptibility. *in vivo*, the local perturbations induced by the various susceptibilities of the tissues result in image artifacts that obscure or distort the anatomical structures being imaged. This is especially true for high field MRI, as the susceptibility effect is proportional to the strength of the field.

Spinal cord imaging at 7T is made particularly challenging by the high complexity of the spinal cord and of the vertebral column, with considerable variety of susceptibility among the tissues, inside a limited diameter volume (Barry et al., 2018; Tillieux et al., 2018) *in vivo* data are heavily affected by the B_0 static field inhomogeneity, due to differences in susceptibility between tissues. Specifically, the magnetic field inhomogeneity, especially at high magnetic field strengths, causes a periodic pattern of signal loss and geometric distortion around each intervertebral junction. These susceptibility-induced artifacts can severely compromise the accuracy and quality of both anatomical and functional imaging of the spinal cord.

To minimize the magnetic field inhomogeneity that can lead to image artifacts, shimming techniques, combined with parameter optimization, have been developed in MRI. They refer to all the methods that can be used to increase the homogeneity of the field (Finsterbusch, 2014). Some of them, such as slice-wise shimming techniques, have been proposed to reduce the distortion and signal drop-out (Finsterbusch et al., 2012; Islam et al., 2019) but substantial artifacts typically persist. As a result, ongoing research is being conducted to develop more advanced shimming techniques and algorithms to improve the homogeneity of the magnetic field in MRI. Additionally, alternative approaches such as the

use of parallel imaging and post-processing correction methods are also being explored to reduce the impact of residual field inhomogeneity on MRI images.

The development of these advanced shimming and post-processing techniques requires frequent testing of protocols and sequences. First stage testing is mostly done on homogeneous phantoms, as scanning human subjects involves additional costs, as well as safety and ethical concerns. Standard MRI phantoms consist of an oil- or water-filled bottle or sphere. These phantoms, however, fail to represent key challenges encountered in vivo, related to human anatomy and physiology. This is particularly evident in spinal cord imaging sequence development, where variations in static and dynamic magnetic fields are among the main challenges. As a result, the need for anthropomorphic phantoms in MRI research has become increasingly apparent. Some of them have been proposed, such as for example the 3D-printed cervical spine phantom by Clifton et al. (2019) that could reproduce some of the spine's mechanical properties, or the pneumatic phantom by Tillieux et al. (2018), which utilized a real cadaver's spine. However, to our knowledge, only a limited number of anthropomorphic phantoms have been developed with a specific focus on spinal cord imaging, and even fewer have addressed the issue of susceptibility artifacts.

The potential of 3D printing in the building of phantoms was demonstrated by Filippou and Tsoumpas (2018). 3D printing has garnered increasing interest from the scientific and clinical communities, due to its several advantages, such as its affordable cost, and above all the great freedom it offers, due to its variety of technologies, materials, and the possibility to build anthropomorphic models directly based on the clinical CT images. However, some challenges about finding materials with relevant properties still remain, and few fully 3D-printed phantoms are available. They are often tuned, or combined with doping agents.

In this work, our aim is to build a 3D-printed anthropomorphic MRI phantom of the human cervical spine to mimic the static B_0 field distribution encountered in vivo. Such a phantom could then be used to optimize advanced shimming and acquisition techniques for 7T spinal cord MRI. After choosing a 3D-printing material, a first phantom of the vertebrae from C3 to C5 was printed, and its susceptibility properties and T_2^* value were computed on field maps and multi-echo gradient echo (ME-GRE) acquired data. Several doping components were added to the C3-to-C5 phantom to improve its magnetic properties until a final phantom representing all the cervical vertebrae within an anthropomorphic container was built.

Theory

The structure of the first **Sections 2.1 to 2.4** was partly inspired by Dance (2014), Weishaupt et al. (2006), and by the previous master's thesis work of Annelen Dogger Schmidt (2022) in the Prof. Vannesjo research group.

2.1 Nuclear Magnetic Resonance and MRI basics

2.1.1 Introduction to MRI

Magnetic Resonance Imaging (MRI) is a non-invasive and pain-free imaging technique based on the magnetic properties of the atomic nuclei. Since its discovery, it has rapidly become the favorite imaging modality, before others such as Computed Tomography (CT) or X-rays, because it offers a superior soft-tissue imaging quality, while not implying any ionizing radiation (Dance, 2014). In addition to the qualitative and anatomical information which is conventionally acquired, structural or functional data can also be acquired through fMRI (functional MRI) or qMRI (quantitative MRI), shifting the process from a pure "picture-taking" to the acquisition of more specific and relevant data.

MRI is based on the Nuclear Magnetic Resonance (NMR) phenomenon, a property of the nuclei to absorb, and then release, applied radio-frequency (RF) at a certain frequency (Dance, 2014). The spin is an intrinsic property of each subatomic particle (proton, neutron, electron). It denotes the magnetic properties resulting from the angular momentum of a particle and hence relates to its ability to undergo nuclear magnetic resonance (Weishaupt et al., 2006). The nucleus is composed of protons and neutrons with each a spin of $1/2$. The sum of the individual spins of these subatomic particles composes the spin \vec{I} of the nucleus. This spin is not null only if the total number of protons and neutrons in the nucleus is odd. Conveniently, the hydrogen atom H^1 , which has the simplest odd nucleus, a single proton, is also the most common atom in the human body, composed of 60 to 90% water or fat. Apart from a few exceptions, MRI is then focused on the hydrogen properties. Due to their spins, all H^1 nuclei undergo a spinning motion similar to that of a spinning top, and are in addition positively charged, leading to the creation of a nuclear magnetic moment $\vec{\mu} = \gamma\hbar\vec{I}$, where γ is the gyromagnetic ratio, and is specific to the considered nucleus ($\frac{\gamma_{H^1}}{2\pi} = 42.58 \text{ MHz/T}$), and \hbar is the reduced Planck constant.

MRI is therefore based on quantum properties. Luckily, it is possible to understand and study it from a classical point of view. In the absence of an external magnetic field, the magnetic moments of the protons are all oriented in a random direction. Overall, the total magnetization vector of the body \vec{M} , as the sum of all the magnetic moment vectors of the hydrogen atoms, is null. However, when a magnetic field B_0 is applied, the spins align themselves in the direction of the field, either in the same direction (parallel) or in the opposite one (antiparallel), as shown in **Fig. 2.1**. As the parallel direction corresponds to a lower-energy state, more spins will align in the same direction as the field. This distribution between

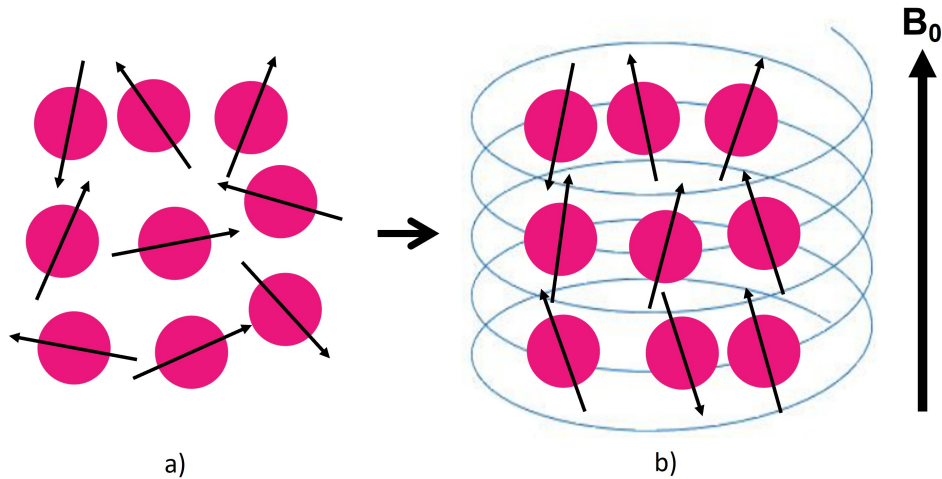


Figure 2.1: In the absence of a magnetic field, the spins of the nuclei are randomly oriented in space (a). But when a field B_0 is applied, they align in its direction, either parallel or antiparallel (b). Figure inspired from Dance (2014).

higher and lower states follows the Boltzmann's probability:

$$\frac{N_+}{N_-} = e^{\frac{\Delta E}{k_b \cdot T}} \quad (2.1)$$

where N_+ and N_- respectively represent the number of parallel and antiparallel spins, ΔE the energy difference, k_b the Boltzmann constant and T the absolute temperature. The total magnetization vector \vec{M} is therefore aligned with B_0 . The B_0 direction is conventionally defined as the z-direction, so at equilibrium, \vec{M} has only a longitudinal component.

As mentioned before, each spinning nucleus interacts with the B_0 field to create a precessional movement of $\vec{\mu}$ around B_0 . The precession is described by the following equation (Nishimura, 1996):

$$\frac{d\vec{\mu}}{dt} = \gamma \vec{\mu} \times \vec{B} \quad (2.2)$$

This equation relates to $\vec{\mu}$ precessing at a frequency $\omega_0 = \frac{2\pi}{T_0}$, called the Larmor frequency:

$$\omega_0 = \gamma \cdot B_0 \quad (2.3)$$

As \vec{M} is aligned in the B_0 direction, it has a stationary equilibrium value \vec{M}_0 , but as soon as other fields will be applied, the net magnetization vector will also precess around the fields (Dance, 2014). To simplify the visualization of the problem, it is common to choose a rotating reference frame at speed ω_0 .

2.1.2 Excitation Process

Applying a time-varying field $B_1(t)$ in the transverse plane, precessing at the Larmor frequency, will cause the net magnetization vector to flip and rotate around the sum of the two magnetic fields $B_0 + B_1(t)$. In the rotating reference frame, $B_1(t)$ is stationary, as it is illustrated **Fig. 2.2**. In clinical applications, the Larmor frequency lies in the radio-frequency (RF) range. Due to its short application time, $B_1(t)$ is

generally referred as the RF pulse. By choosing its strength and length, it is then possible to tip \vec{M} from the longitudinal axis to the transverse plane by an angle α . This angle, called the flip angle, is given by:

$$\alpha = \gamma \cdot B_1 \cdot t_{rf} \quad (2.4)$$

Fig. 2.2 shows the perturbation of \vec{M} by $B_1(t)$, commonly named the excitation phase.

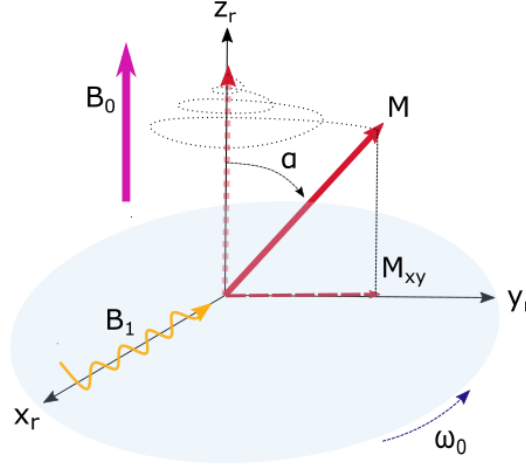


Figure 2.2: In the rotating reference frame, when applying a short RF pulse in the transverse plane, the net magnetization vector is tipped by an angle α from the longitudinal axis. After the application, \vec{M} slowly comes back to its equilibrium position while rotating around the z-axis at ω_0 . Due to the main B_0 field, only the transverse signal can be acquired. The detection of the oscillating M_{xy} signal is possible through a receiving coil in the transverse plane. The acquired signal is known as the Free Induction Decay (FID).

The precessing magnetization vector will then come back to its equilibrium position in the longitudinal plane, while rotating around the z-axis. According to the Faraday's laws, the precession of the M_{xy} component makes it possible to detect the magnetization signal through a coil carefully positioned in the transverse plane. This detected signal is known as the Free Induction Decay (FID) signal.

2.1.3 Relaxation Process

After the excitation process, the magnetization vector progressively returns to its equilibrium position, aligned in the B_0 direction. This relaxation process, from a transverse magnetization to a longitudinal vector, is described by two mechanisms: the desexcitation of the spins and the spin dephasing. These two processes are respectively described by the spin-lattice, or longitudinal (T_1) relaxation time, and the spin-spin, or transverse (T_2) relaxation time.

2.1.3.1 Longitudinal (T_1) Relaxation

The spin-lattice relaxation process corresponds to the restoration of the longitudinal magnetization vector to its equilibrium value M_0 . The excited spins release energy in their surrounding environment to return to their lower energy state, hence the name "spin-lattice". T_1 describes the time needed by the vector to return to 63% of its original value. The longitudinal evolution of the magnetization vector is given by:

$$\frac{dM_z}{dt} = -\frac{M_z - M_0}{T_1} \quad (2.5)$$

corresponding to an exponential evolution. Each tissue possesses a specific T_1 value, which can be used to obtain T_1 -contrasted images, or T_1 -weighted images, by using T_1 -sensitive MR sequences. T_1 is dependent on the field strength. At higher fields, T_1 will be longer, as it requires more energy to exchange with the environment.

2.1.3.2 Transverse (T_2) Relaxation

The transverse relaxation of the magnetization vector is characterized by the spin-spin relaxation time T_2 . In addition to tipping the magnetization vector to the transverse plane, the RF pulse also synchronizes the phase of the spins. The transverse relaxation therefore corresponds to the dephasing of the spins, as illustrated **Fig. 2.3**. Each spin, acting as a small magnet, interacts and slightly modifies the surrounding field, creating small field inhomogeneities. These differences in the environment of the molecules cause variations in the spins precession frequencies, leading to a loss of phase coherence. Furthermore, each process leading to T_1 relaxation also leads to T_2 relaxation, hence $T_2 < T_1$. Indeed, the desexcitations of the spins release thermal energy to the environment, that can modify the angular momentum of the spins, further strengthening the dephasing, and shortening the spin-spin relaxation constant (Nishimura, 1996).

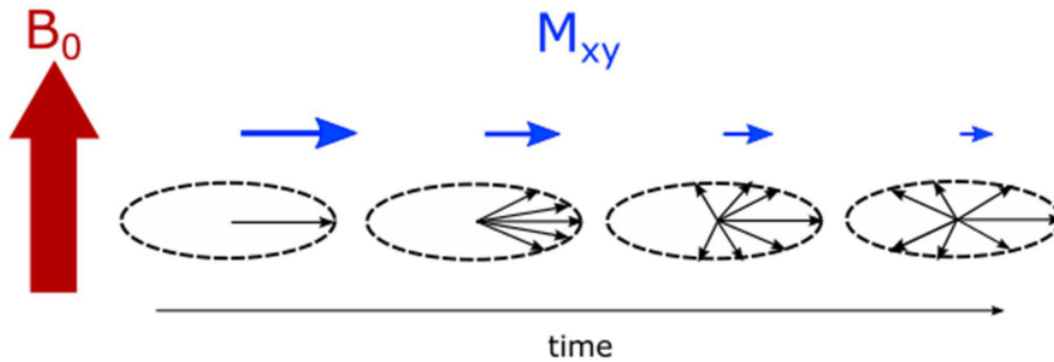


Figure 2.3: Illustration of the loss of phase coherence between the spins. As the dephasing increases, the transverse magnetization vector decreases (Fortin, 2021).

The evolution of the M_{xy} is given by:

$$\frac{dM_{xy}}{dt} = -\frac{M_{xy}}{T_2} \quad (2.6)$$

which leads to an exponential transverse decay. More precisely, T_2 is defined as the time when the magnetization vector has returned to 37% of its value directly after the excitation.

T_2 is an intrinsic relaxation constant which describes the relaxation process in the ideal case of a perfectly homogeneous external field. However, time-independent field inhomogeneities of the external magnetic field introduce an additional static dephasing process, resulting in a faster dephasing than predicted by T_2 . These stationary imperfections in the field, mostly occurring at the tissues boundaries, can be due to imperfect magnetic field generators or susceptibility differences between air, water and the different tissues, as explained in **Section 2.4**. The observed signal decay can also be described by an exponential, but with a smaller time constant T_2^* :

$$\frac{1}{T_2^*} = \frac{1}{T_2} + \frac{1}{T_2'} \quad (2.7)$$

where T_2' is the component due to inhomogeneous field (Dance, 2014; Weishaupt et al., 2006).

As it is not time-dependent, the static dephasing can be reversed by applying a second RF pulse, as it is done in Spin-Echo sequences, but not in GRE sequences. Similarly to the T_1 -contrasted images, T_2 or T_2^* -weighted images can also be acquired using the appropriate MRI sequences. The acquired signal can be enhanced by using contrast agents such as gadolinium to modify both T_1 and T_2 values. Depending on the region of interest and of the clinical reason for the exam, T_1 - or T_2 -weighting can be preferred. T_1 -weighting shows for example great contrast between Gray Matter (GM) and White Matter (WM) and can be used to detect mass or anatomical details, while T_2 -weighting is sensitive to fluids, which is useful for the diagnose of many pathologies (McRobbie et al., 2017).

2.1.4 Block Equation

The evolution of the MR signal can be summed up by the Block equation (Dance, 2014; Nishimura, 1996), which combines the precession movement given in (2.2), with the longitudinal and transverse relaxation processes seen in the equations of the two previous paragraphs (2.5) and (2.7):

$$\frac{d\vec{M}}{dt} = \gamma \vec{M} \times \vec{B} - \frac{M_x \cdot \vec{u}_x + M_y \cdot \vec{u}_y}{T_2} - \frac{(M_z - M_0) \cdot \vec{u}_z}{T_1} \quad (2.8)$$

2.2 Spatial Encoding in MRI

According to the previous sections, spins can be excited by an RF pulse, causing the net magnetization vector to flip to the (x,y) plane. The evolution of the transverse total signal can then be acquired through a receptor coil. However, to finally get an anatomical image, the spatial location of the spins must be encoded to get a differentiation of the local signals. This spatial decomposition of the signal is encoded using slice excitation and Fourier encoding. It is achieved by using independent linear gradients in the x-y-z directions. They slightly modify the local field perceived by the spins, thereby affecting their precession frequency.

2.2.1 Slice Excitation

Even though direct 3D imaging is achievable, most of the MRI methods prefer to reduce the complexity of the problem by treating the volume of interest slice by slice. This transition from three to two dimensions reduces the acquisition time, while allowing a better contrast (Nishimura, 1996).

A so-called 'slice-selective' linear magnetic gradient is applied in addition to the B_0 field in the z-direction, linearly modifying the Larmor frequencies of the spins which become:

$$\omega(z) = \omega_0 + \gamma \cdot G_{SS} \cdot z \quad (2.9)$$

where G_{SS} is the strength of the applied gradient, and z the position along the B_0 -axis (McRobbie et al., 2017). An RF pulse is frequency selective. By simultaneously applying the slice-selective gradient and the RF pulse, only a specific slice of protons is excited, while the rest of the body stays unperturbed. The shape of the selected slice is defined by the Fourier-transform FT of the RF-pulse signal. To get a rectangular profile of the excited protons along the z-direction, a *sinc* $B_1(t)$ field is in general chosen, as the inverse FT of a rectangular function is a *sinc*. The thickness of the slice is then dependent on the bandwidth BW of the RF pulse and of the strength of the z-gradient:

$$\Delta z = \frac{BW}{\gamma \cdot G_{SS}} = \frac{\Delta \omega}{\gamma \cdot G_{SS}} \quad (2.10)$$

2.2.2 Fourier Encoding

The slice-selection process described above allows selecting an in-plane slice of the 3D volume. But to be able to reconstruct a 2D image, the spins also need to be spatially located along the x- and y-axis. As the acquired signal is a complex exponential, spatial information can be encoded in both the frequency and the phase. *Frequency-encoding* and *phase-encoding* are both performed by applying linear magnetic gradients, but with two different timings.

The *phase-encoding* step is performed right after the excitation process. A *phase-encoding gradient* G_{PE} applied along the y-direction during a time τ_{PE} modifies the Larmor frequencies of the spins, creating a phase shift. The induced dephasing is defined by the duration and strength of the gradient,

as well as the physical positions of the protons on the y-axis (Weishaupt et al., 2006; McRobbie et al., 2017):

$$\phi(x) = e^{i\gamma \cdot y \cdot G_y \cdot \tau_{PE}} \quad (2.11)$$

To encode in both in-plane directions, a second encoding process is needed. The *frequency-encoding gradient* G_{FE} is applied in the last orthogonal direction while the signal is acquired, causing the spins to precess with a different speed:

$$\omega(x) = \omega_0 + \gamma \cdot G_{FE} \cdot x \quad (2.12)$$

The acquired signal therefore contains a full spectrum of frequencies, encoding for the position of the spins in the x-direction. The signal acquired can then be expressed as the sum of the local signals:

$$\begin{aligned} S(t) &= \iint_{slice} \rho(x, y) \cdot e^{-i\omega(x, y)t} \cdot dx dy \\ &= \iint_{slice} \rho(x, y) \cdot e^{-i\omega_0 t} \cdot e^{-i\gamma G_{FE} \cdot x \cdot t} \cdot e^{-i\gamma \cdot y \cdot G_{PE} \cdot \tau_{PE}} \cdot dx dy \end{aligned} \quad (2.13)$$

where $\rho(x, y)$ is the spin density and the dependencies in T_1 and T_2 have been ignored to simplify (Dance, 2014). By defining

$$k_i(t) = \frac{\gamma}{2\pi} \cdot \int_0^t G_i(\tau) d\tau \quad (2.14)$$

(2.13) can be rewritten as:

$$S(t) = \iint_{slice} \rho(x, y) \cdot e^{-i\omega_0 t} \cdot e^{-i2\pi(k_{FE} \cdot x + k_{PE} \cdot y)} \cdot dx dy \quad (2.15)$$

which can be recognized as the equation of a 2D Fourier-transform. The information in MRI is therefore not stored in the image space, but in a mathematical Fourier matrix called *k-space*, which represents the spatial frequencies of the MR signal. From there, the image can be obtained by simple inverse Fourier-transform.

G_{PE} and G_{FE} can be seen as ways to navigate inside k-space. In general, it is filled line by line, but the trajectory can also be a zig-zag, or a spiral. In a line-by-line trajectory, the phase encoding gradient is applied to define a k_y value by choosing a certain τ_{PE} and a certain strength, before applying a varying frequency encoding gradient, or *readout* gradient, to browse all the values of k_x , and thus fill one line of the k-space. The process is repeated to cover the whole 2D matrix.

2.2.3 Spatial Conventions

Conventionally, the magnetic field B_0 is set along the z-direction, which is chosen to be the anatomical inferior-superior direction, when the patient is lying down. The patient enters the scanner head first and lies on its back. The horizontal axis, from the right to the left of the patient, is defined as the x-axis, while the vertical axis corresponds to the y-axis. This axis follows the anterior posterior direction, and is then from the top to the back of the patient. **Fig. 2.4** illustrates these orientation conventions. However, attention must be ported to the fact that these conventions can vary from time to time. The orthogonal planes to the x-, y- and z-directions are respectively called the sagittal, coronal and transverse planes.

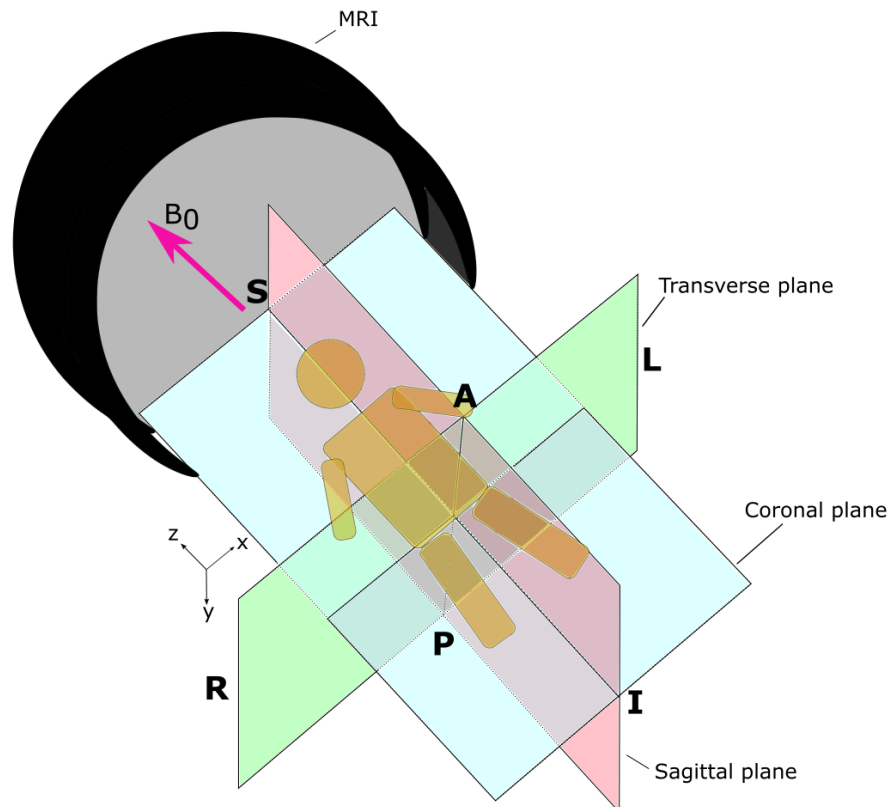


Figure 2.4: Orientation conventions. The sagittal plane is orthogonal to the x-direction, defined as the direction from the right (R) to the left (L) of the patient. The y-direction, from the anterior (A) to the posterior (P) part of the body, cut the y-direction. B_0 , from the feet to the head, follows the z-direction. The transverse plane is orthogonal to the inferior (I) - superior (S) direction.

2.3 Acquisition Sequences in MRI

If slice excitation and phase and frequency encoding are the main components of an MRI acquisition, different types of set of instructions, or *pulse sequences* can be used in MRI. *Gradient Echo* sequences, also called *Gradient-Recalled Echo* sequences (GRE) and *Spin-Echo* sequences (SE) and the two main pulse sequences. In a standard line-by-line filling of k-space, both work on the same principle. The slice of interest is first selected during the RF pulse, before the gradient readout is positioned at the beginning of a line in k-space (at $-k_{xmax}$). This complete line is then acquired, and the process is repeated in order to cover the whole k-space. This process is characterized by two times. The echo time TE is the time between the peak of excitation and the middle of the readout gradient (when $k_x = 0$), while the repetition time TR defines the duration between two excitation pulses (Dance, 2014). TR and TE are chosen depending of the sequence and on the clinical purpose. Short TR and TE will enhance T_1 contrast, while T_1 -weighted images are acquired with long TR and TE. Proton density can also be analyzed through a long TR and a short TE sequence (Micheau and Hoa, 2022).

2.3.1 Gradient-Echo (GRE)

The gradient-echo sequence is one of the simplest pulse sequences, directly using the FID signal. In this sequence described **Fig. 2.5**, a slice-rewinder gradient must be applied after the selective excitation, to rephase the spins. Indeed, the slice excitation gradient results in an accumulation of phases, different for each spin. Thus, the rewinder gradient, applied with an opposite polarity, reverses this dephasing.

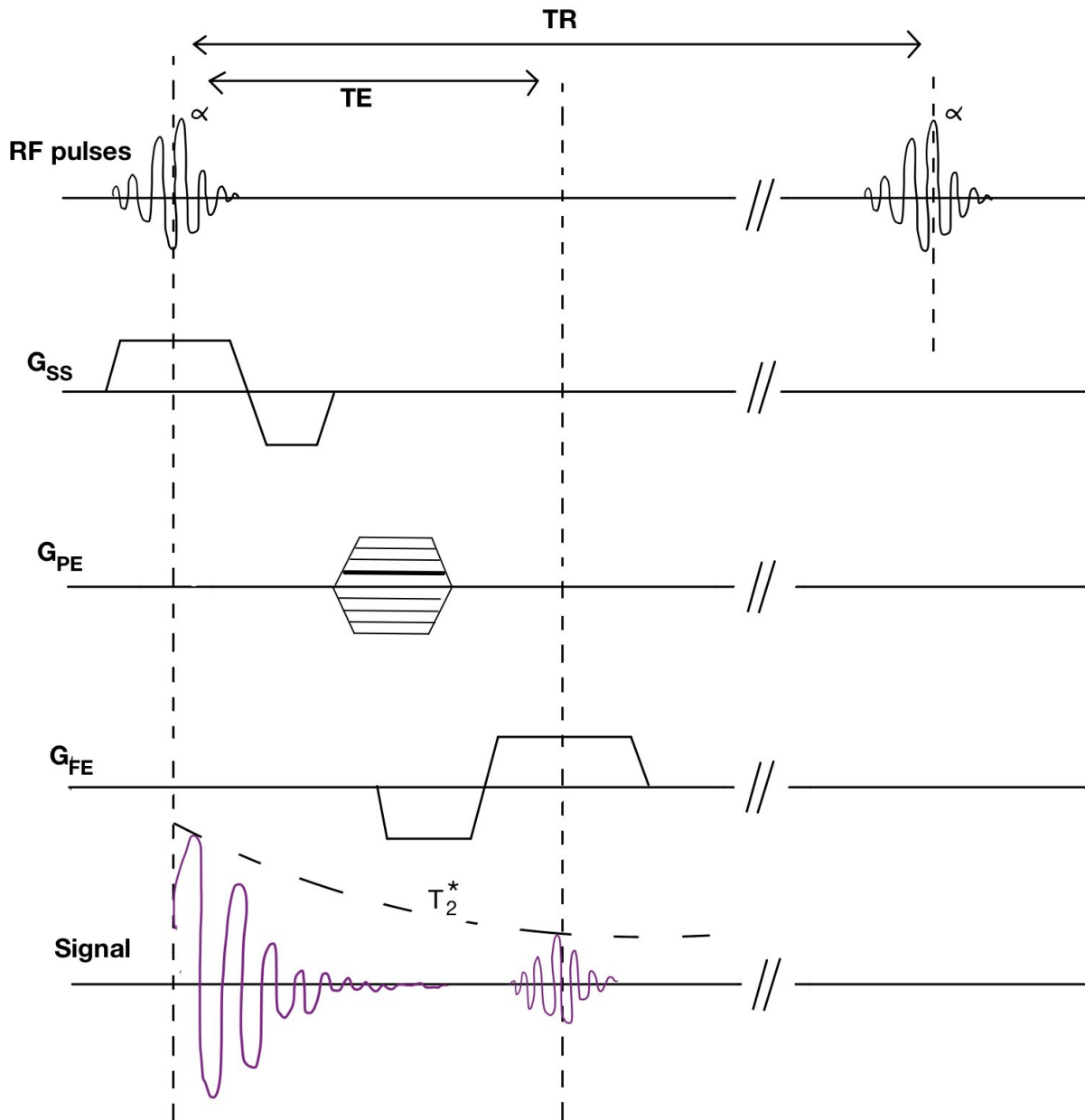


Figure 2.5: Illustration of a basic GRE sequence.

A second reversing gradient must then be applied along the x-direction. The readout *prephase* gradient can be seen as a way to move the readout gradient from the center of k-space ($k_x = 0$) to the extreme end ($+/- k_{xmax}$), in order to acquire a whole line at once, as **Fig. 2.6** shows. The spins shift from each other during the prephase gradient, before being reversed back by the readout gradient, twice as long. The echo signal is generated at TE, in the middle of the readout process, when the magnetization vector has been fully recovered.

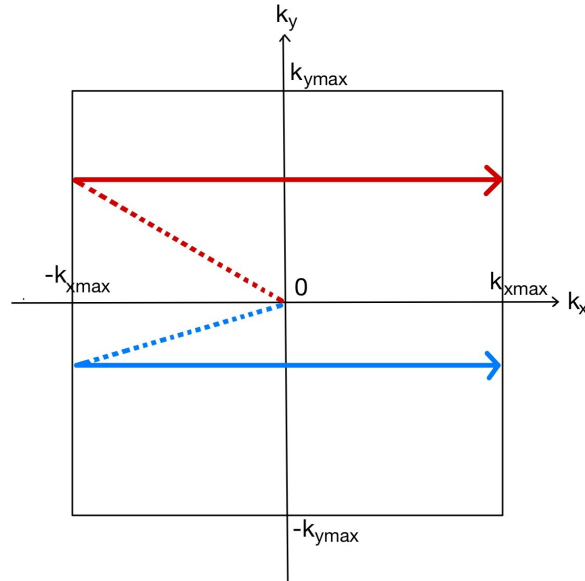


Figure 2.6: In GRE sequences, to fill one line in k-space, the phase gradient and the prephase frequency gradient are applied simultaneously (lines in dots), before reading a line with the readout gradient. The blue and the red arrows are two examples of a line readout.

As a refocusing gradient is preferred to a refocusing pulse in GRE, this sequence does not correct for the coil and susceptibility inhomogeneities. The acquired image is therefore T_2^* -weighted, and can be obtained with a shorter TR than for the SE sequences. This faster acquisition time is one of the main advantages of the GRE sequences, reducing in particular motion artifacts. It is for example used in cardiac imaging or contrast-enhanced MR angiography (Weishaupt et al., 2006; Markl and Leupold, 2012). GRE sequences are also often used in spinal cord imaging, as they offer better contrast than SE acquisitions. Signal intensity can be maximized by using the appropriate flip angle. This optimal flip angle is given by the Ernst relationship:

$$\alpha = \arccos\left(e^{-\frac{TR}{T_1}}\right) \quad (2.16)$$

2.3.2 Multi-Echo GRE (ME-GRE)

It is also possible to acquire many echoes from a single RF excitation pulse. This technique illustrated in **Fig. 2.7** is known as *multi-echo* imaging and is possible with both SE and GRE sequences. In GRE sequences, echoes can be acquired until the full T_2^* relaxation (Elster, 2021). By alternating the polarity of the readout gradient, each line in k-space can be acquired several times, the previous echo being used as a prephase gradient for the next one. This technique can be used to fasten the k-space data acquisition, and to acquire data at different echo times.

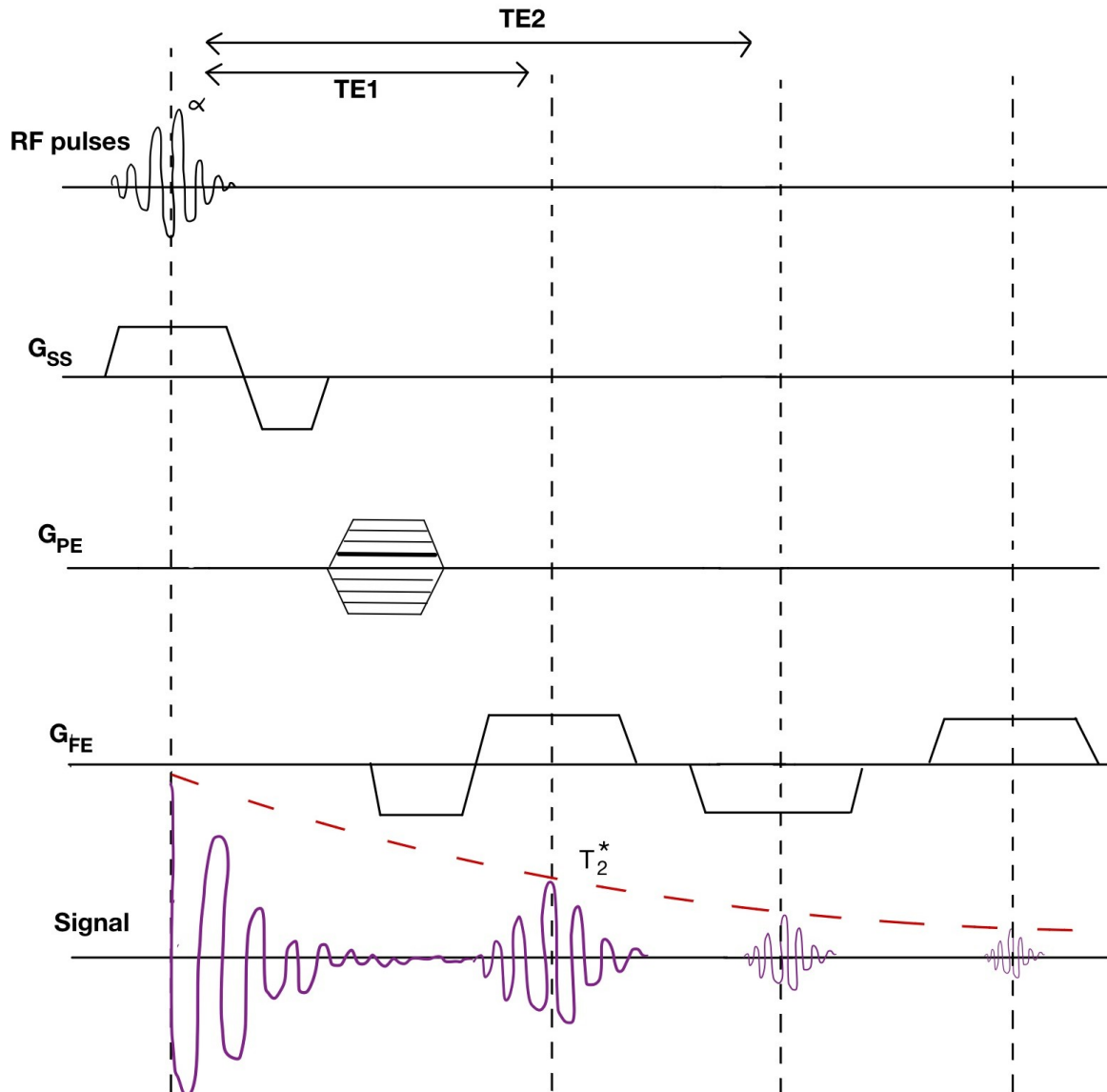


Figure 2.7: Illustration of a multi-echo GRE sequence. Multiple echoes can be acquired with only one excitation pulse. Each frequency readout is used as a prephase gradient for the next echo.

2.3.3 Spin-Echo (SE)

Although gradient echo is quite fast and commonly used, this sequence is very sensitive to static field inhomogeneity (T_2^*). In spin echo sequences (SE), described in **Fig. 2.8**, a refocusing 180° pulse (**Fig. 2.9**) is applied at $TE/2$, after the first 90° excitation pulse. This pulse reverses the spins, so the faster spins are behind the slower ones. As they still keep the same precessing frequency, the dephasing decreases until TE , where the echo signal is acquired. The 180° RF pulse corrects for the T_2^* inhomogeneities, but not for the dynamic inhomogeneities. Thus, the magnetization vector still decreases according to the T_2 exponential.

Trajectory in k-space is illustrated in **Fig. 2.10** (Dance, 2014; Weishaupt et al., 2006; Markl and Leupold, 2012). Unlike in the GRE sequences, no polarity-inverted gradient needs to be applied, due to the inversion of the spins by the refocusing pulse.

Spin-echo sequences are in general used to obtain good quality anatomical T_2 -weighted images.

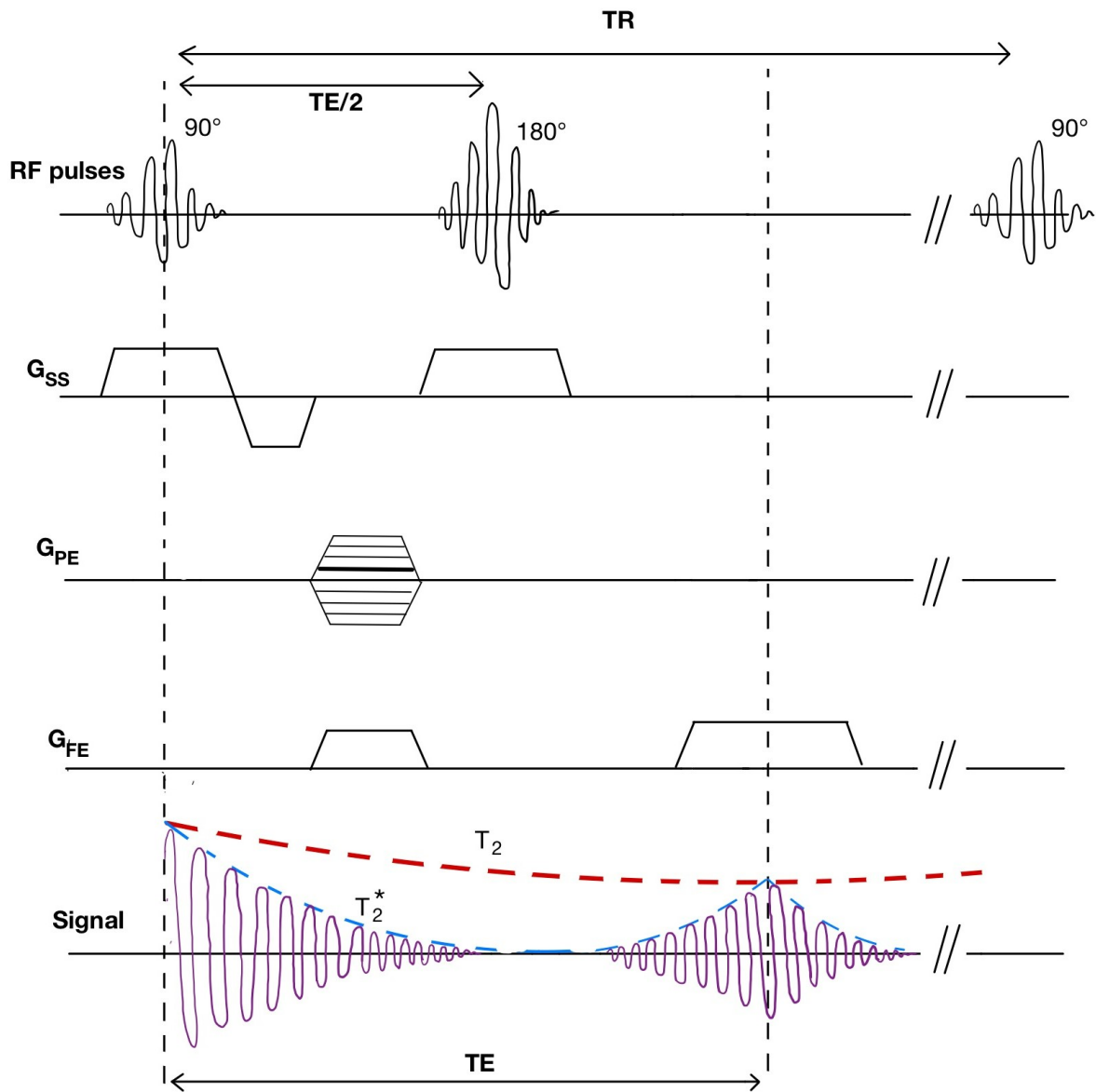


Figure 2.8: Illustration of a basic SE sequence.

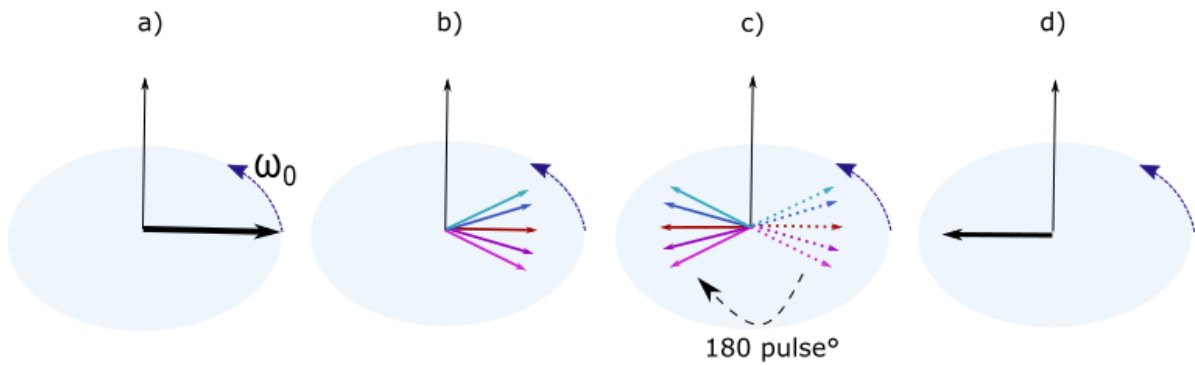


Figure 2.9: Rephasing of the spins in SE. a) The first 90° RF-pulse flips the magnetization vector to the transverse plane. Right after the excitation, all the spins are synchronized. b) The spins then start to dephase due to both static and dynamic inhomogeneities. c) At $TE/2$, the 180° pulse inverts the order of the spins, decreasing the phase shift. d) The echo is finally acquired at TE , when all the spins are back together, and M_{xy} maximum.

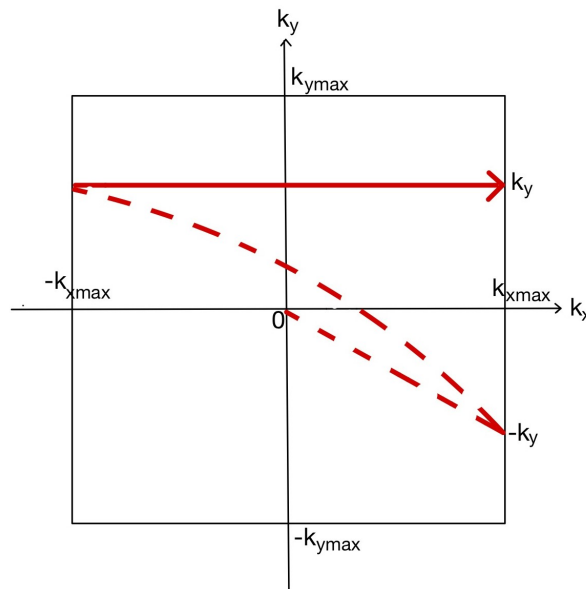


Figure 2.10: The SE sequence is similar to the GRE sequence, except that a refocusing pulse is used instead of a refocusing gradient, resulting in a movement in k-space to the conjugate position.

2.4 Magnetic Susceptibility

2.4.1 Definition

A magnetic moment produces a magnetic field, and a magnetic field can induce a magnetic moment (Le Bihan, 1985). Magnetic susceptibility χ is an intrinsic property of each material, characterizing its ability to interact with, and distort an external magnetic field. Depending on the context, the concept of permeability μ_r can equivalently be used, with $\chi = \mu_r - 1$. However, in MRI, the magnetic susceptibility is often preferred for reasons of scale (Schenck, 1996). χ is defined as:

$$\chi = \frac{\vec{M}}{\vec{H}} \quad (2.17)$$

with \vec{M} the local magnetization of the material, and \vec{H} the applied magnetic field in $A\,m^{-1}$. The total local magnetic field \vec{B} is a sum of the contributions of the applied field and of the material susceptibility:

$$\vec{B} = \mu_0(\chi + 1)\vec{H} \quad (2.18)$$

with μ_0 the magnetic permeability of the vacuum. Depending on the susceptibility value, three types of material can be distinguished: the *diamagnetic*, *paramagnetic*, and *ferromagnetic* materials. In the diamagnetic materials, the induced magnetic moment \vec{M} is opposed to the applied field \vec{H} , resulting in a negative susceptibility value. This effect is quite weak ($\chi \simeq 10^{-6}$). On the opposite, the paramagnetic materials possess a positive susceptibility value, meaning that \vec{M} and \vec{H} are in the same direction. However, without any applied field, these materials don't have any magnetic moment. χ is quite low ($\chi \simeq +[10^{-5}, 10^{-3}]$) and decreases with the temperature. Finally, with a susceptibility between 1 and one million, the ferromagnetic materials have a permanent magnetization and are contraindicated for MRI (Le Bihan, 1985).

2.4.2 Magnetic Susceptibility Artifacts

The spatial variations in susceptibility in between tissues, air and water in the body cause local magnetic field gradients, in particular at the interfaces, contradicting the fundamental MRI assumption that a perfectly homogeneous B_0 field is applied. This results in the emergence of artifacts, especially pronounced with GRE sequences and long TEs, which may appear as signal losses or geometric distortions. The amplitude of these field perturbations is proportional to the applied field strength, which makes these artifacts particularly visible and detrimental in ultra-high field MRI (Saritas et al., 2014; Czervionke et al., 1988).

2.4.2.1 Signal Losses

Inhomogeneities in the local magnetic field create dispersion in the spins Larmor frequencies, as seen in **Section 2.1.3.2**, inducing a dephasing of the spins. These phase shifts originate in mutual cancellations of the magnetization vector, leading to an increased signal loss. This effect is seen within one voxel, as multiple field variations can occur in a small local area, but is enhanced by the presence of tissues or material boundaries. Indeed, due to the susceptibility differences, these interfaces separate areas of different magnetic fields, but must also ensure the continuity of the field. They therefore present very strong magnetic gradients. Signal drop-outs are therefore very common around these interfaces (Czervionke et al., 1988; Port and Pomper, 2000).

2.4.2.2 Geometric Distortions

As **Section 2.2.2** describes, the spins are spatially encoded in k-space using their frequency and phase. Even a slight variation in their Larmor frequency can distort the gradients linearity, and lead to a misplacement of the spins position, thus creating geometrical artifacts. The direction of the induced distortions depends on the chosen k-space trajectory (line-by-line, zig-zag...).

The frequency-encoding process results from the readout acquisition of the frequencies spectrum, and is therefore not an instant process. The accumulation of phase shift is then variable along the frequency-encoding direction, following the equation:

$$\Delta\phi(t) = \gamma\Delta B_0 t \quad (2.19)$$

where t is the time elapsed between excitation and acquisition. However, in a line-by-line acquisition, the time between the excitation and the phase encoding is similar for each line, dephasing the spins in the same amount, and thus not affecting the phase encoding if the inhomogeneities are static in time. In a line-by-line k-space filling, the geometric distortions due to static inhomogeneities can therefore be mostly observed along the frequency-encoding direction.

2.4.3 Field-Mapping

As explained in **Section 2.3.1**, GRE acquisitions are sensitive to any inhomogeneity, and in particular to the differences in susceptibility between the components of the body, creating local field variations. If the field were completely homogeneous, two echoes acquired at different echo times should have the same phase. However, the B_0 inhomogeneities induce a phase accumulation term, proportional to the echo time TE (Finsterbusch, 2014):

$$\phi_i(\vec{r}, t) = \phi_0 + \gamma\Delta B_0(r)TE_i + r_0\gamma \int_0^\infty G_{\vec{r}}(\tau)d\tau \quad (2.20)$$

A map of these field inhomogeneities can be obtained by acquiring two T_2^* -weighted images with two different echo times and subtracting them. This field map is summed up by the following equation and is traditionally expressed as the difference in frequency between the Larmor frequencies $\Delta\omega$:

$$\Delta\omega = \gamma\Delta B_0 = \frac{\Delta\phi_i(\vec{r}, t)}{\Delta TE} \quad (2.21)$$

where $\Delta\phi_i(\vec{r}, t)$ and ΔTE are respectively the phases and echo-time differences.

The two echo times should be chosen with care, as increasing their difference increases the sensitivity, but also enhances the ambiguity of the phase. Phase wrapping problems can be limited by so-called phase unwrapping techniques. If several echo times can be used, in practice, only two are usually employed, as they need to be long.

2.4.4 Simulation of the Field Inhomogeneities

When a strong external magnetic field $\vec{B}_0 = B_0 \cdot \vec{z}$ (with \vec{z} a unit vector along the z-axis) is applied on a sample described by a magnetic susceptibility distribution $\chi(\vec{r})$, the generated magnetic field can be expressed by solving the Maxwell's equations and using a dipolar approximation. Each element of the magnetization distribution $\vec{M}(\vec{r})$ is seen as an independent dipole, whose sum gives the resulting field expressed in (2.22) (Marques and Bowtell, 2005).

$$\vec{B}_d(\vec{r}) = \frac{\mu_0}{4\pi} \int_V \frac{1}{|\vec{r} - \vec{r}'|^3} \cdot \left(3 \frac{\vec{M}(\vec{r}') \cdot (\vec{r} - \vec{r}')}{|\vec{r} - \vec{r}'|^2} (\vec{r} - \vec{r}') - \vec{M}(\vec{r}') \right) d^3\vec{r}' \quad (2.22)$$

This approximation is valid for $|\chi| \ll 1$, which is in general the case within the human body, composed of tissues with a susceptibility $\chi \sim 10^{-5}$ (Schäfer et al., 2009). The use of the Cauchy limit, and therefore of the sphere of Lorentz, described in Durrant et al. (2003) solves the divergence of the integral evaluation for $\vec{r} = \vec{r}'$ (Dogger Schmidt, 2022).

As the main B_0 field is in general applied along the z-direction, the z-component of the induced magnetization vector of the material dominates the transverse components by being the only one that significantly deviates from zero. Thus, using (2.17) for $|\chi| \ll 1$, the magnetization distribution can be written as:

$$M(r) \approx M_z(r) = \chi(\vec{r}) \frac{B_0}{\mu_0 \mu_r(\vec{r})} = \chi(\vec{r}) \frac{B_0}{\mu_0(1 + \chi(\vec{r}))} \approx \chi(\vec{r}) \frac{B_0}{\mu_0} \quad (2.23)$$

By inserting (2.23) into (2.22), the normalized z-component of the susceptibility-induced magnetic field perturbation becomes (Dogger Schmidt, 2022):

$$\frac{B_{z,d}(\vec{r})}{B_0} = \frac{1}{4\pi} \int_V \left(3 \frac{\chi(\vec{r}') \cdot (z - z')^2}{|\vec{r} - \vec{r}'|^5} - \frac{\chi(\vec{r}')}{|\vec{r} - \vec{r}'|^3} \right) d^3 r' = \int_V \chi(\vec{r}') D_z(\vec{r} - \vec{r}') d^3 r' \quad (2.24)$$

with $D_z(\vec{r})$ the dipole field, expressed as follows (Schäfer et al., 2009):

$$D_z(\vec{r}) = \frac{1}{4\pi} \cdot \frac{3z^2 - |\vec{r}|^2}{|\vec{r}|^5} = \frac{1}{4\pi} \cdot \frac{3\cos^2(\theta) - 1}{|\vec{r}|^3} \quad (2.25)$$

θ is the angle between B_0 and \vec{r} , such as $\cos(\theta) = \frac{z}{|\vec{r}|}$.

(2.24) can be recognized as the convolution between a dipole response ($D_z(\vec{r})$) and the susceptibility distribution $\chi(\vec{r})$. The normalized z-component of the induced field can therefore easily be calculated by multiplication in the Fourier space. A rapid calculation of the susceptibility-induced field inhomogeneities can thus be achieved, by simply multiplying the Fourier transforms of the susceptibility map ($\chi(\vec{k})$) and of the dipole field ($D_z(\vec{k})$) defined (2.25):

$$\frac{B_z(\vec{k})}{B_0} = \chi(\vec{k}) \cdot D_z(\vec{k}) \quad (2.26)$$

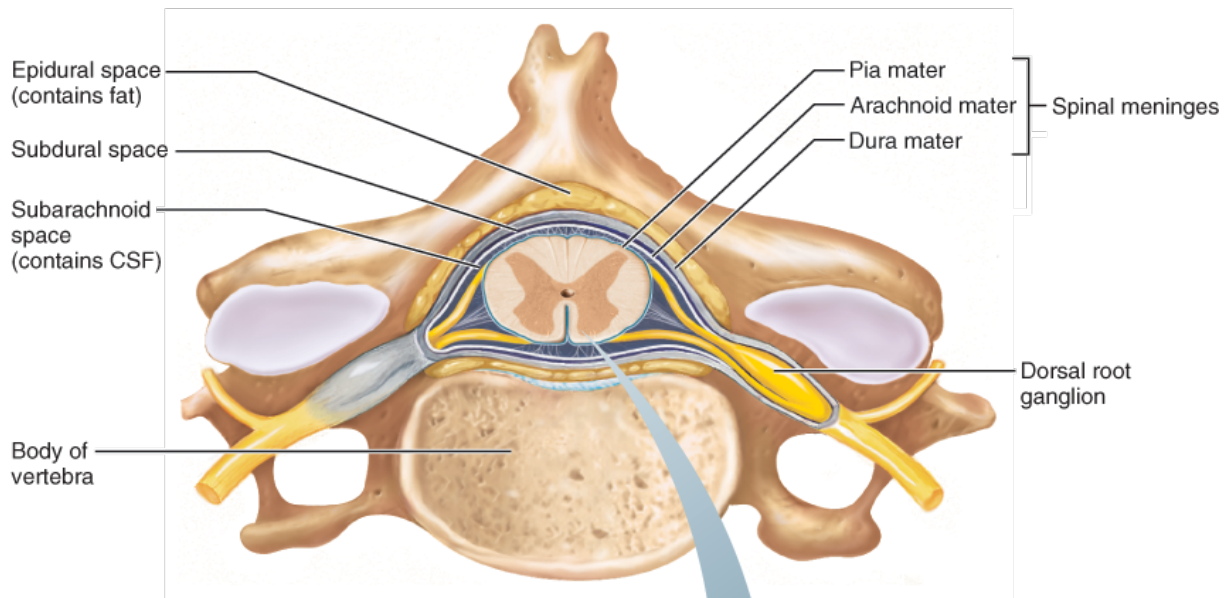
with \vec{k} the position in k-space.

2.5 Spinal Cord Imaging

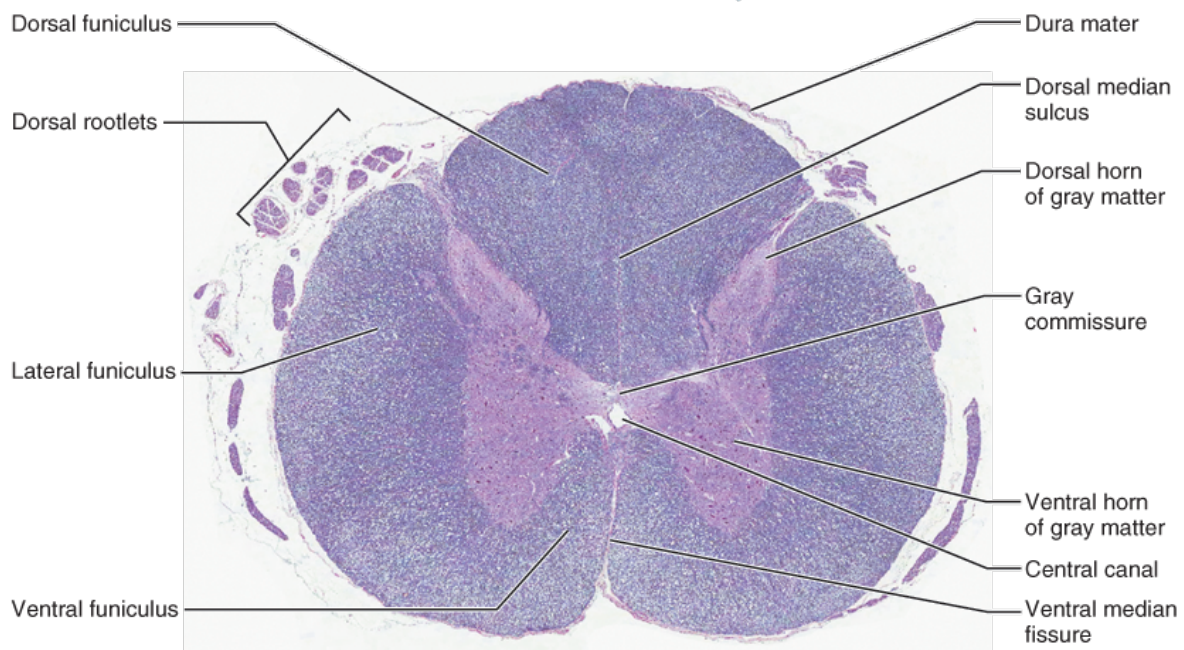
2.5.1 Anatomy and Function

2.5.1.1 Spinal Cord Function

The spinal cord is a central part of the nervous system, and ensures the conduction of signals between the brain and the different parts of the body. It both carries information from to brain, ordering for example the muscles to move, and transmits sensory signals to the brain, while partially processing them. The spinal cord is also responsible for some of our reflexes (Queensland Brain Institute, 2017).



(a) Cross section of spinal cord and vertebra, cervical region



(b) Light micrograph of cross section through spinal cord, cervical region (8x)

Figure 2.11: Cross-section of the spine, in the cervical region (KindPNG.com, 2022). (a) Cross-section of the spinal cord and vertebra. (b) Light micrograph of cross-section through spinal cord (x8). The Grey Matter in the center, in light purple, is surrounded by the White Matter, in dark purple.

2.5.1.2 Structure of the Spinal Cord

The spinal cord is a 1 cm diameter, 45 cm long tubular structure composed of White Matter (WM) and Gray Matter (GM) as shown in **Fig. 2.11 (b)**, similarly to the other parts of the nervous system. In the center, the GM takes the shape of a butterfly, having four wings called "horns". The frontal, or "ventral"

horns are dedicated to the transmission of information from the brain to the muscles, through the motor neurons, while the dorsal ones bring sensory information from different parts of the body to the brain. Gray matter is surrounded by white matter, which contains axons that connect nerve cells (Queensland Brain Institute, 2017).

The spinal cord is protected by three layers of tissues called *meninges* (Nall, 2019). **Fig. 2.11 (a)** illustrates them. The *Pia mater* is the first layer, directly covering the spinal cord, the *Arachnoid mater* is the second, and the *Dura mater*, as the external layer, is tough and protective. The space between the Dura and Arachnoid mater is called the *Epidural space*. Finally, the space between the Arachnoid and Pia mater, the *Subarachnoid space*, is filled by Cerebrospinal fluid (CSF), often considered as the zero-susceptibility reference in the body.

2.5.1.3 Structure of the Vertebral Column

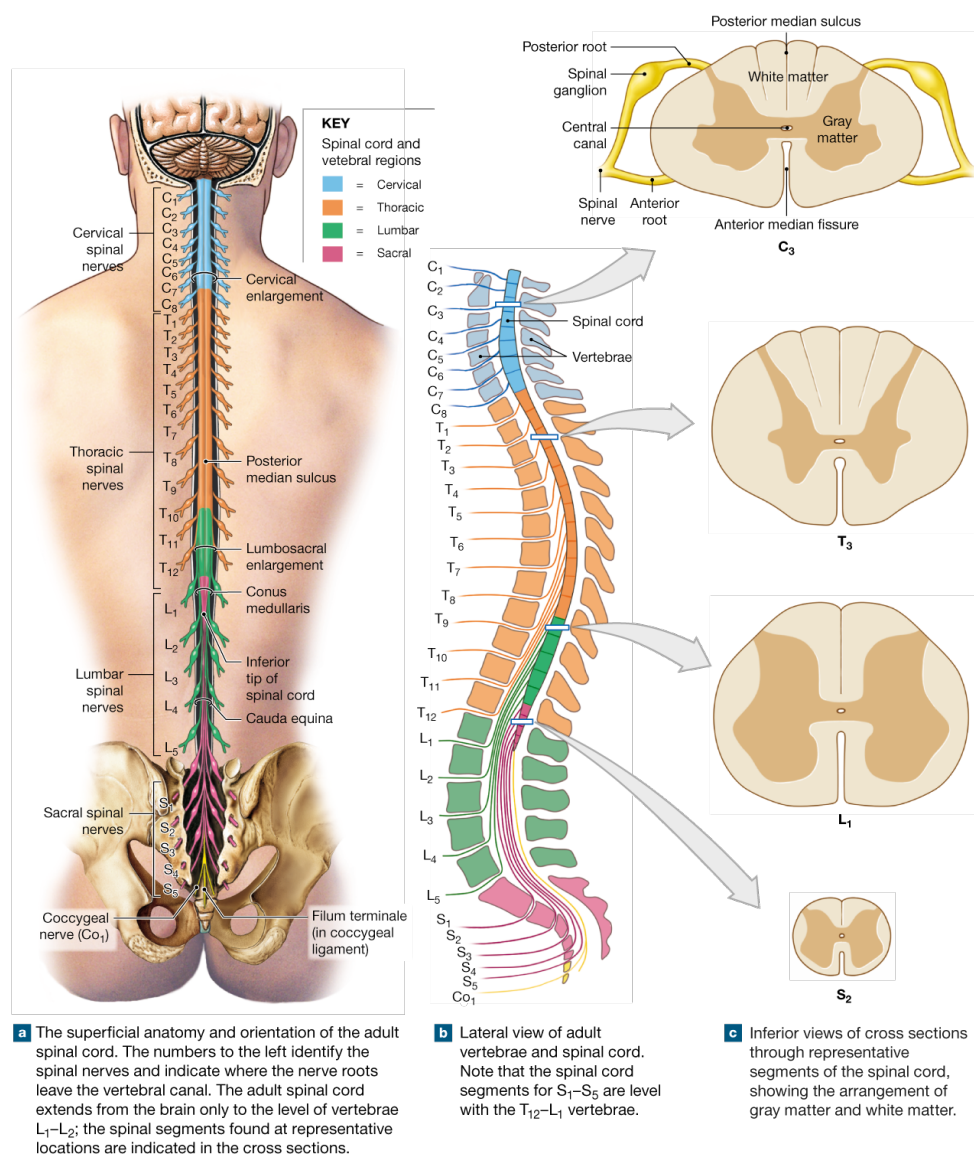


Figure 2.12: Regions of the spine (KindPNG.com).

The spinal cord and the meninges are surrounded by a protective bony structure, composed of 33 vertebrae interposed by cartilaginous intervertebral discs (Kenhub., 2023). The vertebral column extends from the skull to the coccyx and can be divided into five regions described in **Fig. 2.12**: cervical,

thoracic, lumbar, sacral and coccygeal. The spinal cord is shorter than the spine, and usually stops in the top lumbar region (Nall, 2019). Each vertebra has different size, shape and characteristics, especially between different regions.

The cervical area, on which this master's thesis focuses, is composed of seven vertebrae located in the neck. Even though their intervertebral discs are the smallest and thinnest, they are also the most mobile of the spine. Three out of seven of its vertebrae are considered to be atypical and differ in shape from the other vertebrae: C1 and C2, respectively named the Atlas and the Axis, and C7, known as *Vertebra prominens* (Kenhub., 2023).

2.5.2 High-Field MRI of the Spinal Cord

Due to the small diameter of the spinal cord and its extreme complexity, an increased resolution and better contrast and signal-to-noise ratio through Ultra-High Field (UHF) imaging could greatly benefit to spinal cord magnetic imaging. However, these past decades, if many 7T technologies have been developed for the study of the brain, development and interest have been quite slow regarding the spinal cord UHF imaging (Barry et al., 2018).

Magnetic imaging of the spinal cord is made very challenging by the extreme variability of the materials and tissues composing the spine, as seen in **Section 2.5.1.2**. Indeed, in vivo data are heavily affected by B_0 static field inhomogeneities, due to differences in susceptibility between tissues. Specifically, the field inhomogeneities cause a periodic pattern of signal drop-outs and geometric distortions around each intervertebral junction, which severely compromises anatomical, as well as functional, imaging (Saritas et al., 2014; Finsterbusch et al., 2012; Islam et al., 2019).

Dynamic B_0 inhomogeneities are also a huge issue in spinal cord imaging (Tillieux et al., 2018). Patient respiration induces air-volume variations in the lungs, creating a periodic evolution of the susceptibility inhomogeneities.

2.6 Correction of the Artifacts

The generation of a perfectly homogeneous field is therefore complicated by the differences in susceptibility between air, bones and tissues, especially for high-field spinal cord imaging. Advanced correction techniques and optimization of the acquisition parameters must therefore be achieved to improve the image quality, limit signal losses and distortions, and thus provide better clinical diagnoses (Finsterbusch, 2014). Although SE sequences are generally less prone to signal drop-outs compared to GRE sequences, GRE sequences are still necessary for some applications. In particular, field mapping, flow imaging, fMRI, and rapid imaging often require the use of GRE sequences.

2.6.1 Sequence and Parameters Optimization

The choice of the sequence and its parameters is fundamental to minimize the susceptibility artifacts. The shape and intensity of the susceptibility artifacts have been shown to be dependent on local anatomic susceptibility variations ($\Delta\chi$), field strength B_0 , echo time (TE), and receiver bandwidth per pixel $BW_p = \Delta f/pixel$, as described in the following expression (Elster, 2021):

$$\text{Size of the susceptibility artifact} \propto \frac{\Delta\chi \cdot B_0 \cdot TE}{BW_p} \quad (2.27)$$

TE is one of the most important parameters. A short TE reduces the impact of the spin dephasing within one voxel, as the echo is generated more quickly. However, a long enough TE is needed to ensure a sufficient image contrast, so the choice of TE must be done carefully (Port and Pomper, 2000). Increasing the receiver bandwidth, so the strength of the gradient, reduces the impact of the phase shift relatively

to the total signal, thus also minimizing the geometrical distortion. Susceptibility artifacts can also be reduced by decreasing the voxel volume in the frequency direction, thus decreasing the intravoxel phase shift. Finally, a diminution of the field of view (FOV) is beneficial for reducing the artifacts (Saritas et al., 2014; Barry et al., 2018).

In parallel imaging, the position of each coil and the signal intensity they each receive is taken into account as a new information, which allows a reduced number of phase-encoding steps during the acquisition, and thus a reduced acquisition time (Elster, 2021). Parallel imaging techniques have been shown to reduce the geometric distortions in some multi-echo imaging sequences by shortening the length of the total echo train, thus decreasing the spins dephasing. Shortening the acquisition times also decreases the motion artifacts (Deshmane et al., 2012).

2.6.2 B_0 Shimming

Directly increasing the field homogeneity is also a way to minimize the artifacts. *Shimming* describes the techniques used to correct for the magnetic field inhomogeneities and improve the homogeneity of the magnetic flux density (Finsterbusch, 2014). It can be active or passive.

Standard active B_0 shimming is achieved by decomposing the apparent magnetic field into spherical harmonic basis functions, and correcting the first harmonics using a corresponding current, up to the second or third order. Each spherical harmonic is generated by a dedicated coil and is subject specific (Juchem et al., 2011; Barry et al., 2018). B_0 field maps can be used as a basis for the shimming calibration (Finsterbusch, 2014). However, given the complexity of the spine, the low harmonics are not sufficient enough to perfectly correct the field, especially for large volumes.

Multi-Coil shimming is a recent technique, where multiple individual constant current coils are arranged closely around the patient. The multiplicity of the coils allowing a larger amount of magnetic field shapes, more complex field inhomogeneities of the body can be corrected. Multi-Coil techniques are promising, and have been shown to significantly reduce the susceptibility artifacts in the brain at 7T (Juchem et al., 2011).

Passive shimming, obtained by positioning chosen materials with specific susceptibility values close to the patient, has recently been shown to be a promising field homogeneity improvement technique. However, it is for now more difficult to adjust it to each specific patient (Barry et al., 2018).

2.6.3 Slice-Wise Shimming

In case of local inhomogeneities due to a complex periodic shape, such as in the spinal cord, where the alternation of bones and intervertebral discs creates periodic drop-outs and distortion of the signal, slice-wise shimming techniques can also be used (Islam et al., 2019; Finsterbusch et al., 2012). These techniques try to minimize the through-slice dephasing in T_2^* -weighted acquisitions, by shimming each slice separately.

2.6.4 Post-Processing

In this thesis, we mainly focused on the pre-acquisition and intra-acquisition corrections of the artifacts. However, post-processing methods also exist and can be equally clinically relevant. Some of these techniques are described in Martin and Bender (2015) or Wang and Alexopoulos (2016).

2.7 Phantom Building (3D Printing)

Shimming and correction techniques are in constant improvement, and techniques such as multi-coil shimming, slice-wise shimming, or parallel imaging have been shown to significantly limit the B_0 field variations and thus decrease their artifacts (Deshmane et al., 2012; Barry et al., 2018; Port and Pomper,

2000). However, some field inhomogeneities still remain, especially in 7T spinal cord imaging. Imaging phantoms are therefore very useful to help optimize advanced shimming and acquisition techniques. Phantoms are objects of varying complexity or realism, used to test the performance of imaging machines, or to evaluate and experiment with new techniques. 3D printing is an emerging technology that can be particularly useful in the construction of medical phantoms (Filippou and Tsoumpas, 2018).

2.7.1 General Principles and Benefits of 3D Printing

3D printers, already used in many technological fields, are today enjoying a growing popularity in medical sciences. Although quite expensive, their cost is compensated by their large number of applications and advantages. 3D printed models can be obtained from any sufficient 3D image dataset. CT images are more commonly used, and gives the possibility to print physical volumetric models of patients, which tends to drive towards a more individualized and patient-specific medicine and a decrease in mortality, mistakes and operating room time. Implants and new materials can now also be used, with reduced time of production, and increased anthropomorphic shapes. Finally, research and studies will also benefit from this 3D printing revolution, with for example the possibility to design more anthropomorphic phantoms and test new MRI methods (Mitsouras et al., 2015)

Different technologies of 3D printers are on the market: vat photopolymerization (also called stereolithography, or simply resin printing), material jetting, binder jetting, material extrusion, powder bed fusion, sheet lamination, and directed energy deposition (Mitsouras et al., 2015). Each of them is based on different printing methods and materials and offers variable costs and biophysical properties. The standard format of 3D printing files is the *STL* format. Multiple softwares, such as for example *3D Slicer* (Kikinis et al., 2012; Fedorov et al., 2012; Clifton et al., 2019) offer conversion tools from DICOM (the standard format for medical images) to STL.

2.7.2 Advantages and Disadvantages of a 3D Printed Phantom Compared to a Cadaveric One

One could think that the simplest and best way to create phantoms with similar properties to human tissues and bones would be to use tissues and bones from animals or humans. Indeed, animal extracted materials have biophysical properties, magnetization and structure similar to those of humans (Keereman et al., 2011). However, some unknowns and technical issues occur from the use of cadavers. If animal and human body properties are quite similar when they live, a phantom developed from animal cadavers may suffer from the embalming process, as it may be impaired by time and temperature (Baba et al., 1994; Lennie et al., 2021). The use of ex-vivo samples also raises reproducibility and preservation issues, as well as clean-up concerns before, during and after the experiments (Lennie et al., 2021; Keereman et al., 2011). Animal and human ethics must also be taken into consideration. All these reasons, added to the fact that animal materials can't be arranged into completely anthropomorphic shapes, leads to a quite low interest in cadaveric MRI phantoms in the literature. Only phantoms extracted from some specific organs or simple parts of the body have been evaluated (Keereman et al., 2011).

As explained in **Section 2.7.1**, 3D printing technologies can produce very complicated anthropomorphic shapes. A phantom based on CT images can provide patient-based volumes with a very high accuracy (Clifton et al., 2019; Mitsouras et al., 2015). Of course, no single material can exactly replicate all the properties of tissue and bone, and compromises must be made in the choice of materials (Filippou and Tsoumpas, 2018), but the research interest for 3D printing materials and 3D printed phantoms is constantly growing (Filippou and Tsoumpas, 2018; Mitsouras et al., 2015; Rai et al., 2019). In magnetic phantoms imaging, constraints linked to MRI compatibility and visibility must be added, complicating the problem. Finally, a 3D printed phantom provides reproducibility, as its numerical model can be used several times, and flexibility to change. Indeed, each material can be changed or modified separately from the others, which can simplify the research process and reduce costs (Kobe et al., 2019). **Table. 2.1** summarizes the pros and cons of 3D printed phantoms when compared to ex-vivo phantoms.

	3D printing	Cadavers
Shape	High accuracy in producing complicated anthropomorphic shapes by using CT images (Clifton et al., 2019; Mitsouras et al., 2015)	Lack of anthropomorphism of the animal cadavers (Lennie et al., 2021)
Physical properties	No perfect material to simulate tissues (Filippou and Tsoumpas, 2018). Difficulty of finding an MRI compatible and visible material that fits the susceptibility (Mitsouras et al., 2015)	Tissues and bones extracted from cadavers have a structure and magnetic properties (susceptibility) similar to those of living humans. However, the embalming process may impair these properties (Lennie et al., 2021; Keere-man et al., 2011)
Literature	Growing interest in 3D printed phantoms (Filippou and Tsoumpas, 2018; Mitsouras et al., 2015; Rai et al., 2019)	Low interest in cadaveric anthropomorphic phantoms (Lennie et al., 2021).
Conservation	No specific issue	Cleaning before, during and after the experiments, and frequent tissue replacement needed (Lennie et al., 2021)
Reproducibility	Yes	No (Keere-man et al., 2011)
Flexibility to changes	High flexibility: each material can be changed separately (Kobe et al., 2019)	Low flexibility
Ethics	The images used for the design of the phantom must be free of access	Animal and human ethics

Table 2.1: Comparison of the advantages and drawbacks of using a 3D printed phantom or a cadaveric phantom

2.7.3 Existing 3D Printed MRI Phantoms of the Cervical Spine

Research regarding the 3D printing of phantoms is in full expansion. The paper from Filippou and Tsoumpas (2018), with a review of the 3D printed imaging phantoms, shows the potential of such phantoms in clinical applications. It nevertheless emphasizes the difficulty of finding materials fitting the properties of interest. Rai et al. (2019) demonstrates the feasibility of the use of 3D printable materials for MRI phantoms. A cervical spine phantom has been printed in Clifton et al. (2019) and was able to fit some of the mechanical properties of the human spine. Another was also generated by Mitsouras et al. (2017) and demonstrated that current 3D printing technologies are ready for being used to print anatomically accurate MRI/CT phantoms. However, to our knowledge, no available realistic 3D printed cervical spine phantom is yet able to reproduce the susceptibility inhomogeneities observed in vivo in the magnetic imaging of the spine.

2.7.4 Doping Agents to Match Tissues Properties

In order to approximate tissue properties, it is common practice to construct phantoms using different components that allow for the modification of relaxation times, electrical properties, and magnetic properties. These contrast agents can lead to the creation of liquid phantoms, or, more commonly, gel phantoms to reduce diffusivity (Duan et al., 2014).

NaCl is commonly used as a conductivity controller (Bennett, 2011; Ikemoto et al., 2013).

Manganese (Pan et al., 2011; Douglas et al., 2013) and gadolinium (Kato et al., 2005; Ikemoto et al., 2013) are the most commonly used contrast agents. They are often used in gel phantoms based on agar or PVP (Ianniello et al., 2018). Furthermore, Duan et al. (2014) built a sucrose–NaCl-based gel phantom that demonstrated the strong relationship between the concentration of sugar and the decrease of both T_1 and T_2^* .

Methods

In this section, the methods used to build the phantom are presented divided into four experiments. The first one was the comparison of five printing materials, to decide which one to use for the vertebrae. The second section concerns the evaluation of the magnetic properties of different solution ingredients, which were then chosen or not to be incorporated in the phantoms. Based on these results, two successive phantoms of the C3 to C5 vertebrae were built, trying to match the properties of the in vivo tissues. Finally, this work was extended to the creation of a human-shaped phantom, from the head to the thorax, comprising all the cervical vertebrae and the first thoracic vertebra.

Data was acquired on a 7T Siemens Terra system at St. Olav's hospital in Trondheim, Norway. All the acquisitions were done using the head coil, except for the final phantom, which was imaged with a cervical coil. The DICOM data were converted into NIfTI files using MRICroGL (NITRO, 2014). All the simulations were run on Matlab 2022a (The MathWorks Inc., 2022), while all the other data analyses were coded on Jupyter notebooks (Kluyver et al., 2016) in Python 3.9.13.

3.1 Choice of the printing material

In this section, the field effects of five printing materials from various printing processes, in a salty water solution, were compared in order to choose which material to use to build the phantom. The field distortion due to each sample was linearly compared to the theoretical one generated by a Fourier-based simulation of a sphere, to determine the susceptibility difference between the material and the external solution.

Five printing materials were tested, in the form of spherical samples of 1.5 cm in diameter. Their characteristics are summed up in **Table. 3.1**.

3.1.1 Experimental Set-up

The materials were individually placed in the center of a distilled water solution, with 7.9 g of salt (4.94 g/L) to assure a conductivity similar to human tissues (Bennett, 2011). "Antibac skincare" soap from "Kiilto" was also added to the solution to prevent the formation of air bubbles at the surface of the 3D printed materials. A 150 mm diameter plastic lamp cover from Clas Ohlson (Clas Ohlson) was used as an external shell, with an almost spherical capacity of 1.6 L. Each 3D printed sphere was attached via a sewing thread, the ends of which were taped to the outside of the plastic sphere as shown in **Fig. 3.1**. To ensure watertightness, the opening of the lamp cover was covered with a reusable IKEA silicone food lid (IKEA) and sealed with a rubber band.

The same set-up without any material to be tested was also acquired to get a reference image of the background field.

	PLA	Standard White Resin (v4)	M3 Crystal	Flexible 80A Resin	Nylon
Brand	Prima Value	Formlabs	3D-Systems	Formlabs	FormLabs
Printer	Prusa i3MK2	Form3B	3600 MJP	Form3B	Fuse 1+ 30W
Printing method	FDM	SLA	Material Jet	SLA	SLS
Cost	-	+	+++	+	+
Flexibility	no	no	no	yes	no
Resolution	-	++	++	-	++
Availability	All phantoms	All phantoms	All phantoms	All phantoms.	Final phantom

Table 3.1: Main characteristics of the tested 3D printing materials.



Figure 3.1: Set up of the first experiment: choice of the printing material. The sphere of the material to be tested is hung by two threads in the center of a plastic sphere filled with water, salt and soap. The assembly is closed by a reusable IKEA silicon lid and a rubber band to ensure water-tightness.

3.1.2 Field Map Acquisitions and Analysis

3.1.2.1 Field map Acquisition Sequences and Parameters

A B_0 field map (FM) of the assembly was acquired in the sagittal direction with a 1 mm^3 isotropic resolution, echo times of $TE_1 = 3.06 \text{ ms}$ and $TE_2 = 4.08 \text{ ms}$, and a repetition time $TR = 1050.0 \text{ ms}$. A flip angle $\alpha = 53$ degrees was chosen, and the head coil was used.

3.1.2.2 Comparison of the Materials

The center of each material was manually determined by plotting the field maps in the three planes such as illustrated in **Fig. 3.2**. The phase inhomogeneity along the three axes passing through this center was then plotted for each of the materials, to better visualize the impact of each material on the field in every direction. Each line-plot was centered on the sphere using the coordinates that were previously determined.

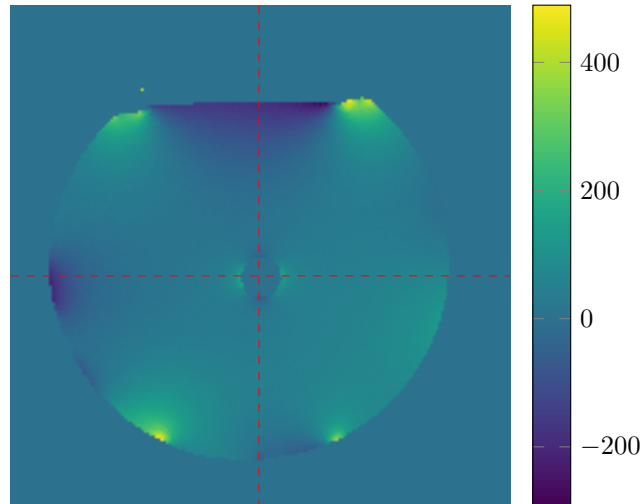


Figure 3.2: Field map in hertz of PLA. The intersection of the red lines determines the center of the sphere. A line plot of the inhomogeneities in the three directions was then plotted, centered on this sphere. The line plots then describe the inhomogeneities along the red lines.

The materials were then compared on their ability to affect the surrounding field, while also considering their printing accuracy and cost.

3.1.2.3 Simulation of a Sphere

A Fourier-based method simulation was then run on Matlab to model the expected susceptibility artifacts generated by a perfect sphere. This sphere was chosen to be of higher resolution (radius $r = 100$ voxels) than in the measured image, to limit the errors due to discretization in the borders of the simulation. The Matlab code we used was written by a former student of the Prof. Vannesjo research group, Annelen Dogger Schmidt (2022), based on the equations and methods described in **Section 2.4.4**. The sphere was assigned a uniform susceptibility value and was multiplied with a dipole function in k-space, before being inverse transformed back to image space.

3.1.2.4 Determination of the Material Susceptibilities

To rescale the measured data by considering the water background as the zero reference, the mean value of the inhomogeneities generated by water in the middle of this reference scan was computed, and subtracted to the final FMs.

The susceptibility of the materials were finally computed by comparing the acquired and simulated field maps. For each material, the simulated FM was reshaped to the same number of pixels as the acquired data. An identical region of interest (ROI) was defined for both the simulated and measured data, to focus on the artifacts directly created by the sphere. A linear regression was then performed on all voxels within the ROI (except those parts of the sphere itself) to analyze the relationship between the simulated and acquired phase inhomogeneity values fm_{simu} and fm_{exp} , such that $fm_{exp} = a \cdot fm_{simu} + b$. This regression model aimed to determine whether the simulated artifacts were comparable to those

observed experimentally, as well as to estimate the slope coefficient a . The magnetic susceptibility value χ_{mat} of the material compared to water was then calculated by:

$$\chi_{mat} = \frac{a}{f} \quad (3.1)$$

with $f \approx 300$ MHz the frequency of the 7T MRI. χ_{mat} is generally expressed in ppm.

3.2 Testing additives to the solution

Various substances were then tested to dope the water solution, in order to better match to human relaxation times and magnetic susceptibilities, inspired by the recipes given in Lopez-Rioz and Cohen-Adad (2023) and Duan et al. (2014) (AMRI, 2016). Two types of mouthwashes, one with alcohol and one without, were analyzed as potential preservatives, along with different concentrations of sugar, to investigate their impact on the susceptibility difference and relaxation time of the solution. During the phantom acquisitions, soap was added to prevent the formation of air bubbles around the vertebrae. Therefore, in this section, we studied the impact of this addition on susceptibility.

3.2.1 Solution Ingredients and Experimental Set-ups

This experiment was divided in two parts. First, to evaluate the susceptibility impact of small amounts of soap in the external solution, a protocol similar to that described in **Section 3.1** was followed. The susceptibility difference between the spherical sample under study and the external solution was computed in the same conditions, except that various amounts of soap, close to the one needed to remove the bubbles, were added to the external solution. Four solutions were tested, with soap concentrations evenly dispersed between 0 and 15 mL in 1.6 L solution, to ascertain the impact of adding small amounts of soap. We chose to study the susceptibility difference with the sample of Standard White Resin, as this material was then used to print the first spherical phantoms, as described in **Section 3.3.1**.

In a second time, eight solutions of various amounts of soap, salt, mouthwash or sugar were tested, divided into two sets of acquisitions. The set-up, inspired from the previous one, is illustrated in **Fig. 3.3**. The four solutions to be analyzed were placed in small watertight tubes, which were positioned in a square in the middle of a two-layer plastic film. This plastic film was then inserted in the center of the previously used plastic sphere, bonding the film to the walls, to prevent the device from floating. Finally, the sphere was filled with a solution composed of 7.9 g salt, 10 mL soap and distilled water, and sealed by an IKEA silicone food lid. The following solutions were first evaluated:

- a solution of $\approx 6\%$ of Listerine Total Care mouthwash;
- a solution of $\approx 6\%$ of COOP alcohol-free mouthwash;
- a solution of $\approx 50\%$ of Anglamark liquid hand soap;
- a blank solution identical to the external solution.

Several sugar concentrations were then investigated:

- $C_1 = 350$ g/L sugar;
- $C_2 = 550$ g/L sugar;
- $C_3 = 750$ g/L sugar;
- a solution of $C_3 = 750$ g/L sugar, 1 g of salt, and 6% of alcohol-free mouthwash.

All the solutions were prepared with distilled water.



Figure 3.3: Set-up of the second experiment. The four tubes to be tested were inserted in a two-layer plastic film in the center of the plastic sphere, which was filled by a solution of salt, soap and distilled water.

3.2.2 Field Maps Acquisitions and Analysis

This section follows the same steps that were described in **Section 3.1.2**, with some slight modifications, explained in detail in the following paragraphs.

3.2.2.1 Acquisition Sequence and Parameters

Similarly to the procedure described in Section 3.1.2.1, B_0 field maps (FMs) of the assemblies were acquired with the head coil at a 1 mm^3 isotropic resolution using echo times of $TE_1 = 3.06 \text{ ms}$ and $TE_2 = 4.08 \text{ ms}$, a repetition time of $TR = 1050.0 \text{ ms}$, and a flip angle of $\alpha = 53$ degrees. The FM of the sphere inside a soap solution was acquired in the transverse plane, while the FMs of the solutions with various concentrations of sugar, mouthwashes, and soap were acquired in the coronal direction.

3.2.2.2 Simulation of the Susceptibility Effects

A simulation was performed to predict the susceptibility artifacts generated by the sphere using a Fourier-based approach in Matlab, similar to the one described in **Section 3.1.2.3**. However, this time, the simulation was run on a mask of the sphere, which was obtained by thresholding the magnitude values of the acquired data. Specifically, all magnitude values above a threshold of $s = 400$ were set to 1, while the rest were set to zero, as illustrated in **Fig. 3.4**. The mask was then assigned a uniform susceptibility value, and the Fourier-based simulation was performed to obtain the expected and theoretical field variations corresponding to the chosen susceptibility difference between the sphere and the solution.

To compare the performance obtained with a simulation run on a perfect sphere of higher resolution as done in **Section 3.1.2.3**, we also ran a simulation on a perfect sphere of radius $r = 100$ voxels.

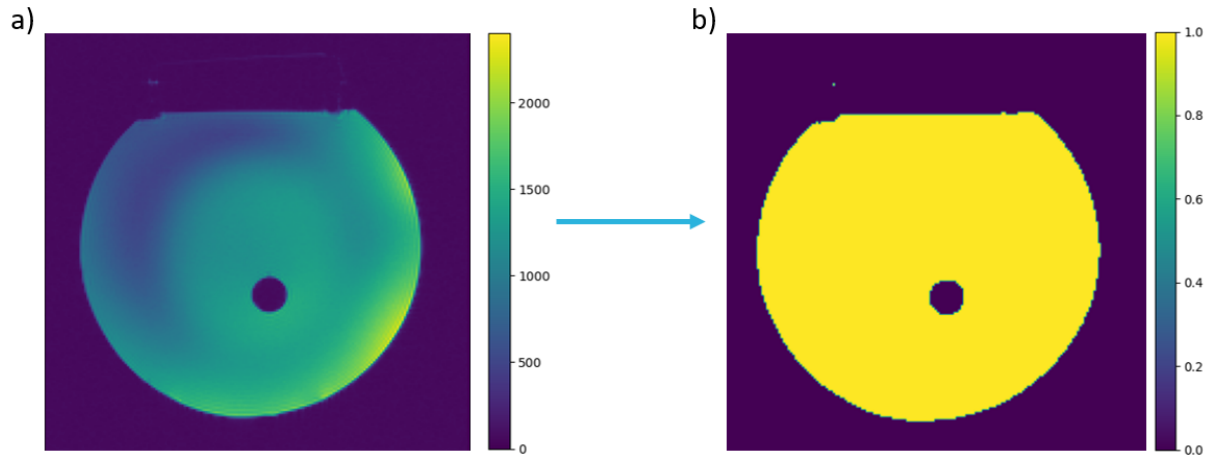


Figure 3.4: Illustration of the determination of a mask. a) A threshold $s = 400$ was defined on the acquired magnitude image to extract b) a mask of the studied component.

Finally, a binary mask of a cylinder of radius 5 pixels, length 20 pixels, oriented along the y-axis, was created on Matlab. The Fourier-based simulation was similarly run on it to simulate the field inhomogeneity generated by the vertical tubes in the MRI.

3.2.2.3 Determination of the Susceptibility of the Components

The FMs were corrected using the background removal method that was also used to correct the spherical phantom acquisitions in **Section 3.3.2.2**. To perform this correction, a reference background FM was subtracted from the studied field map to minimize the container's artifacts. Then, the data was recentered around zero by subtracting the average value of the field map from the final FM.

Finally, the field variations created by each solution or by the sphere were linearly compared to the expected inhomogeneities generated in the respective simulations, as described in **Section 3.1.2.4**. A histogram of the error $f(x_i) - y$ was also plotted, with y the acquired value on each voxel, and $f(x_i)$ the predicted linear value using the regression coefficients. In the assessment of the susceptibility of the solutions inside the tubes, a ROI containing the cylinder of interest was defined on a single slide of the acquired and simulated FMs.

3.2.3 Multi-Echo GRE Acquisitions and Analysis

Once the susceptibility effects were determined, we focused on acquiring and analyzing data from Multi-echo 2D GRE acquisitions of the eight studied solutions, to determine if some of the tested components had T_2^* modifying properties. Indeed, the transversal relaxation time of water being much higher than the one of tissues, considered to be between 20 and 50 ms (Peters et al., 2007), the external solution of the final phantom needed to be tuned to decrease its relaxation time.

3.2.3.1 Acquisition sequence and parameters

A coronal multi-echo 2D GRE sequence with a resolution of $0.3 \times 0.3 \times 3.0$ mm was utilized to quantify the signal decay of the eight solutions. The sequence involved acquiring 12 equally spaced echoes with a range of TE values from $TE_1 = 7.40$ ms to $TE_{12} = 80$ ms.

3.2.3.2 T_2^* values

The T_2^* values of the external solution, and of the eight tested solutions, were determined by fitting an exponential function $f(TE) = A \cdot e^{-TE/T_2^*} + b$ between the 12 echoes for each specific voxel. Each

relaxation time was also associated with its corresponding coefficient of determination R^2 .

As the variability between each voxel was very high, even within the same tube, a circle of radius $r = 10$ voxels was defined around the center of each tube. Then, the T_2^* -value of each sample was assigned to be the mean value of the T_2^* of the voxels inside the defined circle, and having a coefficient of determination $R^2 > R_{\min}^2$. R_{\min}^2 was defined to be as high as possible while keeping at least 5% of voxels to get a mean value. As the variability was different for each tube, as well as their T_2^* value, the threshold was chosen differently for each sample. The standard deviation between the kept voxels of each tube was also computed.

3.3 Spherical phantoms

Two spherical phantoms were constructed to analyze the effect of 3D printed C3 to C5 vertebrae on the field. Both phantoms were imaged using a field map and a multi-echo 2D gradient echo sequence.

The first phantom consisted of the C3-to-C5 vertebrae placed within a spherical plastic cover lamp filled with a solution of water, soap, and salt.

In the second phantom, sugar was added to decrease both the T_2^* and the susceptibility of water, and alcohol-free mouthwash was included as a preservative. The spherical container of the second phantom was reinforced with epoxy and fiberglass to test the resulting artifacts.

3.3.1 Building the Phantoms

An STL template of the vertebrae C3 to C5 was extracted from the subject *sub-gl017* in the public CT dataset *VerSe 2020 validation* (Liebl et al., 2021; Löffler et al., 2020; Sekuboyina et al., 2021). The DICOM data were uploaded to the software 3D Slicer (Kikinis et al., 2012; Fedorov et al., 2012), where the region of interest was first selected using the ‘Crop Volumes’ module. The segmentation of the vertebrae was then defined with the ‘Segment Editor’ module, first by applying a threshold, allowing to automatically preselect the vertebrae, then by manually correcting the segmentation with the eraser, painting and smoothing tools. To allow more precision, each vertebra was segmented separately from the others, before grouping them in the final segmentation containing C3 to C5. Finally, the STL template of the segmented vertebrae was exported from 3D Slicer.

The vertebrae were 3D printed at 1:1 scale, with a layer thickness of 0.1 mm, in standard White Resin (v4) by the Stereolithography (SLA) Form3B printer from Formlabs.

The phantoms were then built using the C3 to C5 vertebrae and a set-up inspired from the one previously used for the testing of printing materials in **Section 3.1.1**. The vertebrae were suspended in the center of the 15 cm diameter plastic sphere with two threads passed through the transverse foramina (holes at the extremities of the vertebrae). In the first phantom, the 1.6 L container was filled with a solution of deionized water and 7.9 g salt. Approximately 12 mL of Anglamark liquid hand soap was also added to avoid air bubbles formation at the surface of the vertebrae. In the second phantom, an external solution of 2 L of water for 700 g of sugar, 80 mL of alcohol-free mouthwash, 15 mL soap and 9.9 g of salt was prepared 24 hours before the acquisition, to ensure a good dissolution of sugar.

The phantoms were closed with the previously used IKEA silicon lid and the rubber band. A schematic workflow of the proposed approach is presented in **Fig. 3.5**.

Before the second phantom’s acquisition, multiple pieces of glass fiber fabric (roving) from Biltema (a) were used to completely cover the spherical container. The fabric was glued onto the container using laminating epoxy also from Biltema (b), and allowed to dry for 74 hours. The inside of the sphere was also painted with epoxy.

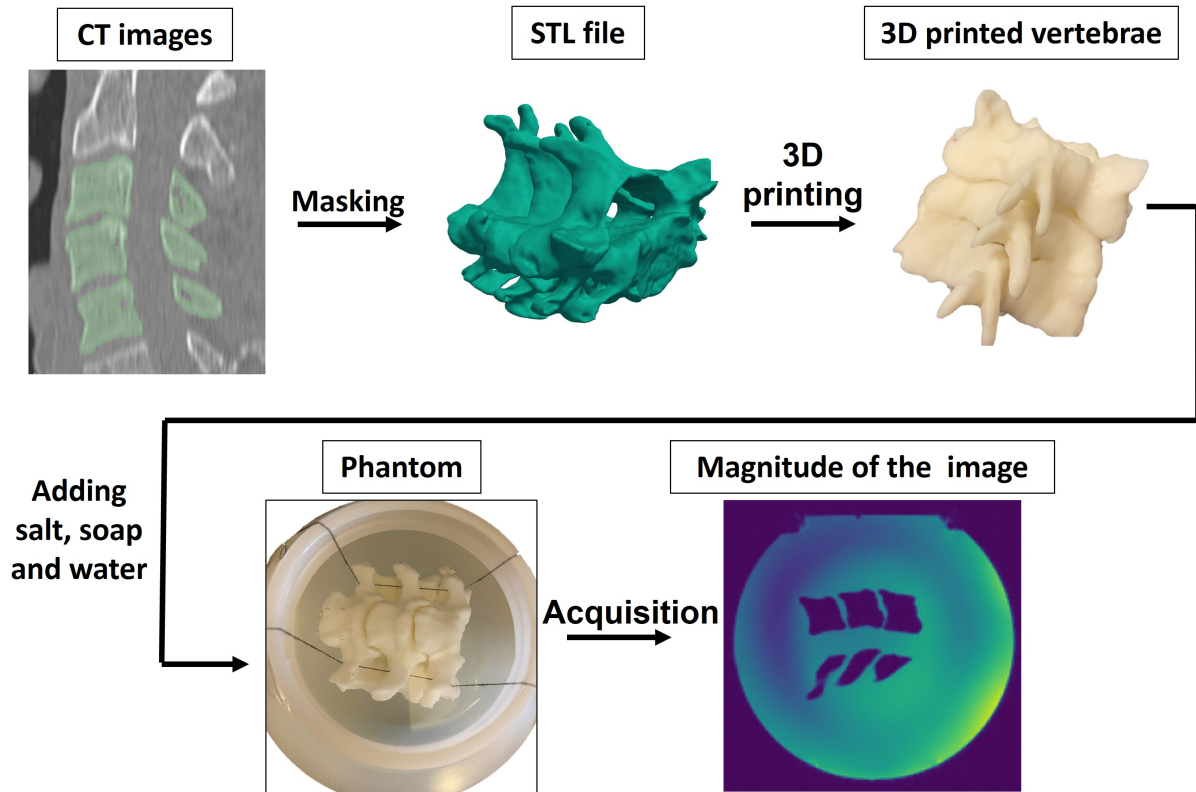


Figure 3.5: Workflow of the first C3 to C5 phantom building from CT images to acquired data. In the second phantom, sugar and mouthwash were also added to the solution, and the lamp cover was covered with epoxy and fiberglass.

3.3.2 Field Maps

3.3.2.1 Field Map Acquisition Sequences and Parameters

B_0 field maps (TR= 1050.0 ms, $TE_1 = 3.06$ ms, $TE_2 = 4.08$ ms, flip angle $\alpha = 53$ degrees) of the phantoms were acquired in the sagittal direction, with the head coil. A 1 mm^3 isotropic resolution was chosen. Reference B_0 field maps of the external solutions inside the spherical shell with no vertebra were also acquired to correct for the background inhomogeneities, as explained in the next section. In the first phantom only, the slices were angulated to be chosen perpendicular to the spinal canal, as it is generally done in vivo to avoid partial volume effect.

3.3.2.2 Background Correction Techniques

Several background correction methods were implemented on the first C3 to C5 phantom to try to reduce the artifacts created by the background solution and the external container: 3D linear gradient corrections, shape functions, Gaussian filters, subtraction of the mean and background subtraction. Some combinations of these methods were also tested.

A linear gradient correction was first proposed. For each direction $i \in \{x, y, z\}$, the mean value of each slice along i was computed, excluding the values inside the mask of the vertebrae, to get an array of the field variation along i . A linear function was then fitted on this array to get an approximate linear gradient of the field. Finally, the FM values were corrected by subtracting for each voxel the values of the three linear gradients.

A second method using shape functions, inspired from finite element analysis, was also tested. This method calculated the 3D field variations using a linear combination of the non-homogeneity values at

specific ‘nodes’ in the sample. It first defined a set of eight ‘nodes’ by taking the average value of the input array over small cubic regions of the array. Shape functions were then defined for each node. Each of them was the linear combination of cubic functions along the x, y and z directions, and varied cubically between 0 and 1 depending on the relative position of the voxel of interest with respect to the node. These eight shape functions were finally combined linearly to compute the expected value of the field non-homogeneity in each voxel. Similarly as in the previous linear gradient correction method, the FM values were then corrected by subtracting for each voxel the value of the computed correction matrix. This shape function correction method was tested in two different configurations. It was first evaluated by taking node values at the eight corners of the 3D data array, and was then tested in 2D, by fitting one gradient per slice.

Smoothing the FM to reduce the artifacts using multidimensional Gaussian filters with different standard deviations was also tested.

The mean value of the data, excluding voxels inside the vertebrae, was computed in addition to every other correction technique, to recenter the data around zero.

A last method was finally tested, consisting in acquiring a background reference of the set-up without the vertebrae, and subtracting it to the acquired vertebral data. Before being subtracted from the data, this reference FM was first smoothed using a 3D Gaussian filter with a standard deviation of $\sigma_{water} = 2$.

In the following parts of this thesis, we chose to correct the background artifacts by subtracting the smoothed reference background. Using the mask, the voxels inside the vertebrae were set to zero and ignored, as there was no signal here, and therefore no valid FM. Each final field map was computed by subtracting the averaged value of the corrected field map (excluding the interior of the vertebrae), and smoothing with a Gaussian filter of standard deviation $\sigma = 0.5$.

3.3.2.3 Simulations, Susceptibility and Local Field Gradients

For each phantom, a Fourier-based simulation of the susceptibility artifacts generated by the vertebrae in solution was run on a magnitude-extracted mask of the vertebrae, similarly as what was done in **Section 3.2.2.2**.

The susceptibility difference between the vertebrae and the external solution was determined by linear regression between the acquired data and the simulation on a mask of the vertebrae, as described in **Section 3.1.2.4** with equation (3.1). A histogram of the error distribution has also been associated with the regression.

For the two spherical phantoms, local field gradients along the z-direction of the FMs were calculated by taking the difference between neighboring voxels in the z-direction, after that the final FMs (already corrected with the manipulations explained in the previous sections) were first smoothed again with a Gaussian filter of standard deviation $\sigma = 0.75$.

3.3.3 Multiecho GRE acquisition

3.3.3.1 Acquisition Sequence and Parameters

A transversal multi-echo 2D GRE sequence of 0.3x0.3x3.0 mm resolution was acquired to measure signal loss between 12 evenly spaced echoes between $TE_1 = 7.40$ ms and $TE_{12} = 80$ ms.

3.3.3.2 T_2^* Values

Fitting an exponential function $f(TE) = A \cdot e^{-TE/T_2^*} + b$ between the 12 echoes for each unique voxel yielded the T_2^* value of the external solution, and its coefficient of determination R^2 .

Due to the predominance of water in the solution of the first phantom, its T_2^* value was difficult to compute as it exceeded the chosen echo times, resulting in significant variability between the computed values. To obtain a better estimation of the overall relaxation time of the external solution, the mean value and standard deviation of the computed T_2^* values were calculated between voxels with $R^2 > 0.9$, inside a circular ROI of radius 40 voxels, in a portion of the image not including the vertebrae or their artifacts.

3.3.4 Signal loss comparison

To verify that the data obtained during the FM acquisition was consistent with the one obtained during the GRE multi-echo acquisition, the signal difference between the first and last echo of the ME-GRE acquisition of the first phantom was visually compared to the local field gradient. To compute the local field gradient, each voxel v of the field map was compared to its 2 closest neighbors in the z -direction (the one before and the one after). A linear regression between these three voxels was run, and the obtained slope was stored in the signal loss matrix, voxel v . The process was repeated on all voxels of the FM to obtain a matrix representing the local gradient obtained by FM acquisition.

3.4 Final C1 to T1 phantom

Finally, in this section, the study was extended to the full cervical spine, and an anthropomorphic external shell was produced to simulate the artifacts generated both by the vertebrae C1 to T1 and by the external human shape.

3.4.1 Building the Phantom

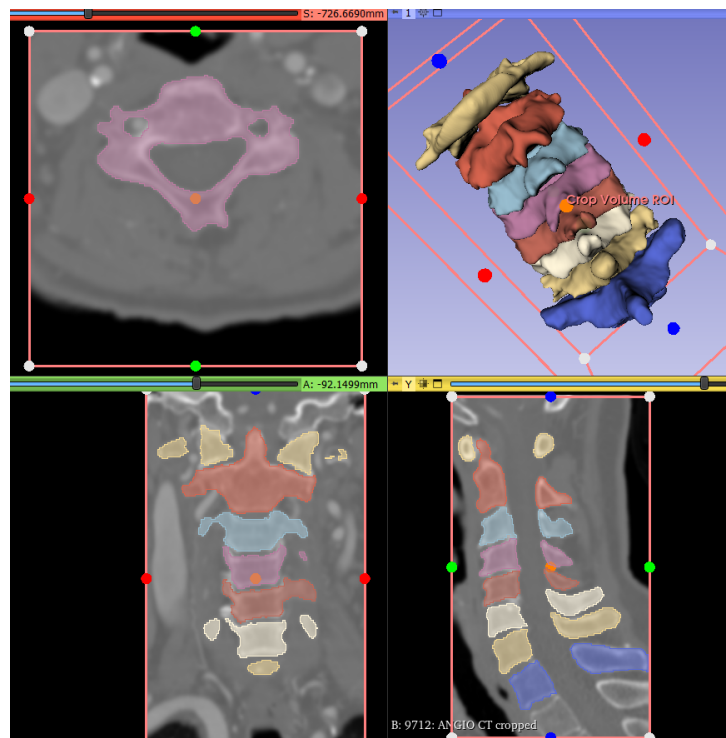


Figure 3.6: 3D Slicer visualization of the segmented C1 to T1 vertebrae. The transversal (top left), coronal (bottom left) and sagittal (bottom right) are shown in addition to the resulting 3D model (top right).

Vertebrae from C1 to T1 were segmented using the same protocol as for the C3 to C5 phantoms that was explained in **Section 3.3.1**. Data was taken from the free online head and neck CT dataset (Dr. Mike, 2016) and extracted using 3D Slicer. Each vertebra was exported in a separated STL file, which were then merged into one final combined file with the online STL file merger Aspose (Aspose). The final vertebral template obtained with this segmentation is shown in **Fig. 3.6**.

The vertebrae were 3D printed at 1:1 scale, with a layer thickness of 0.1 mm, in nylon, by the Selective Laser Sintering (SLS) printer FormLabs Fuse 1+ 30W.

An anthropomorphic shell was designed and 3D printed to fit the 3D printed vertebrae into a volume that closely resembled a real neck.

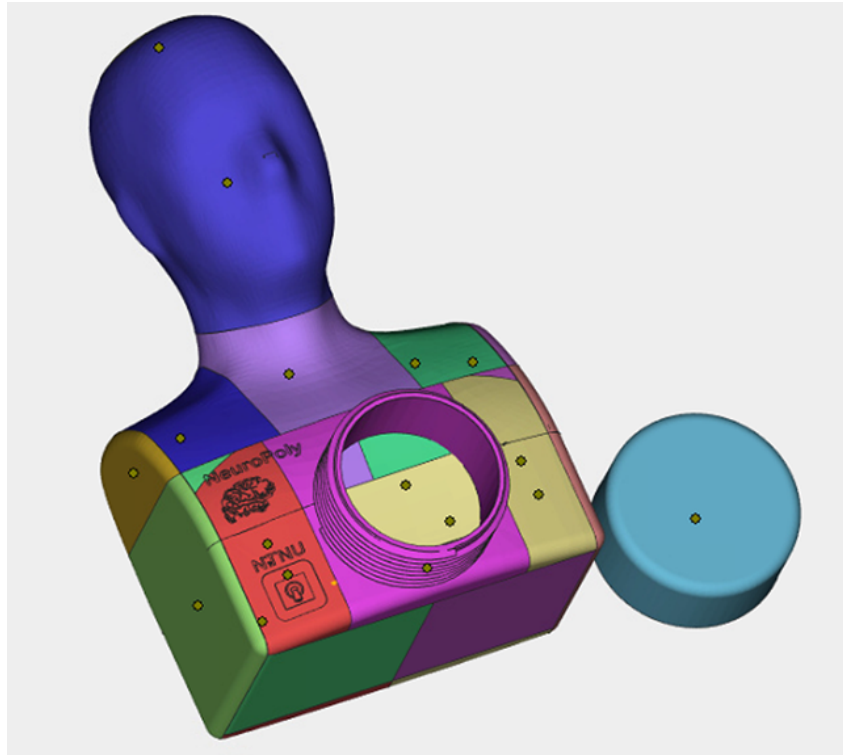


Figure 3.7: The designed shell was divided into several parts as in a jigsaw puzzle. These parts were printed separately and then assembled and glued together by the online printing company.

The head, neck, shoulders and thorax shell was inspired from the Spinoza phantom developed by Lopez-Rioz and Cohen-Adad (2023). Their computer-aided design (CAD), composed of a phantom body and of a cap, was opened in Solidworks 2022 (Dassault Systèmes Solidworks Corporation, 2022) to be modified and adapted to the needs of our project. Their model, which stopped fairly below the shoulder level, has been lengthened to the chest level. The opening on the side was plugged, and the thorax was provided with a large opening that could be closed by a screw cap system. Attention has been paid to make this opening higher than the nose, in order to be able to fill the phantom in its entirety. Finally, a bar at the level of the nose was added in the phantom to define a positioning point for the beginning of the vertebrae.

This shell was then printed in nylon (SLS material, EOS PA2200) at a reduced size by ordering it to the Norwegian online company Protototal AS (PROTOTAL AS). Each dimension has been resized to 80% of its initial length, allowing the reduction of the volume to be printed, while keeping humanly acceptable dimensions. Nylon was chosen as the printing material because the SLS process does not need support structure, as the build chamber is filled with material and only the areas that are to become actual parts are sintered by the laser. This property allowed us to print the shell as a jigsaw puzzle, as illustrated in

Fig. 3.7, to utilize the area inside the body and nest the pieces as tight as possible, and therefore reduce the printing time and costs. Another advantage of nylon compared to PLA, which is the cheapest printing material, was the fact that it could be printed with 100% infill, whereas PLA could not.

To ensure the waterproofness and the solidity of the structure, the shell was covered with roving fiberglass (Biltema, a), the whole glued by laminating epoxy (Biltema, b). A layer of epoxy was also applied on the inside. The recovery process was performed in two stages. Firstly, the anterior section of the phantom and the upper sides were covered with fiberglass, while the inside and the screw cap were coated with epoxy. After 48 hours, once the epoxy had hardened, the phantom was turned over to cover the backside with fiberglass. Finally, the phantom was left in a dry area for several days, before being polished with sandpaper. Four plastic hooks were glued in the posterior part of the phantom, and one next to the opening, to help hanging the vertebrae.

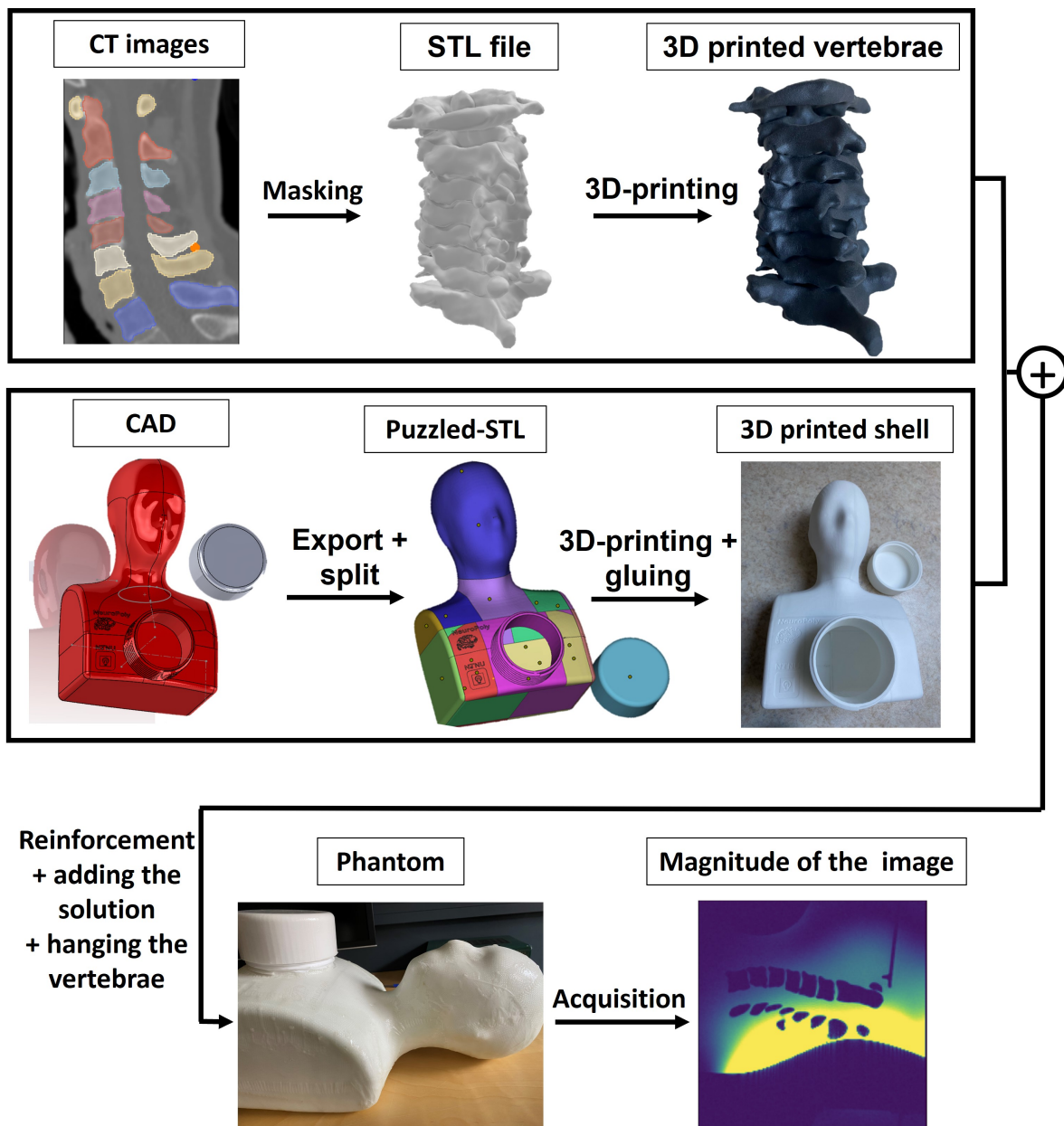


Figure 3.8: Workflow of the final anthropomorphic phantom building from CT images and CAD to acquired data.

The final phantom consists of the C1 to T1 vertebrae in a solution of water, 5 g/L of salt, 75 g/L of sugar and 15 mL of soap per liter, within the 3D printed head-to-thorax shell. Two threads were

passed through the transverse holes of the vertebrae, then knotted to allow the structure to be positioned within the shell using the five hooks. As the nylon vertebrae were floating in the solution, this step was performed while the phantom was 3/4 full.

The workflow of the building process, from the CT images and the CAD to the acquisition of images, is illustrated in **Fig. 3.8**.

3.4.2 Field Map Acquisition and Analysis

3.4.2.1 Acquisitions Sequences and Parameters

A B_0 field map of the final phantom, with 1 mm^3 isotropic resolution ($TR = 1050.0 \text{ ms}$, $TE_1 = 3.06 \text{ ms}$, $TE_2 = 4.08 \text{ ms}$) was acquired on the 7T Siemens Terra system. Contrary to the previous acquisitions, the cervical coil was used, with a flip angle $\alpha = 40$ degrees. A reference B_0 field map of the solution inside the shell with no vertebra was also acquired to correct for the shell inhomogeneities.

3.4.2.2 Simulations, Susceptibility Difference and Local Field Gradients

Similarly than in **Section 3.2.2.2**, a Fourier-based simulation of the susceptibility artifacts generated by the vertebrae was run in Matlab, on a magnitude-extracted mask of the vertebrae. This mask was framed to shape the vertebrae closely, neglecting in a first time the shell. The simulation was finally run on the mask, assigning the value 1 to the voxels representing the vertebrae and zero to the voxels of the solution, as done for the previous phantoms.

To visualize approximately the impact of the shell and of air on the structure, a second mask separating in three the voxels belonging to the vertebrae, to the solution and to the exterior or to the shell, has been designed. The susceptibility of the external air was chosen to be zero, while the one of the vertebrae was $-\text{coeff}_{\text{air}}$ and the one of the solution was $-\text{coeff}_{\text{air}} - 1$. The simulation of the susceptibility artifacts was then run on this approximate mask for different choices of $\text{coeff}_{\text{air}}$.

Due to the significant background effects of the shell, the acquired FM of the vertebrae was once again corrected by subtraction of the reference FM previously smoothed by a Gaussian filter of standard deviation $\sigma = 2$ voxels. Since the vertebral sector of interest was longer than in the previous phantoms, multiple reduced regions of interest (ROI) were separately studied, such as the restrictions of the FM to the vertebrae C3 to C6, or to C1 to C3, for example. However, strong field variations still remained in the background even after the reference background removal, so each selected ROI was further corrected by removing the 3D linear gradients and recentered on zero by removing their mean values. These correction methods are explained in detail in **Section 3.3.2.2**.

As before in **Section 3.1.2.4**, the susceptibility difference between the vertebrae and the external solution, and its associated error distribution were determined by linear regression between the acquired data and the simulation of a mask of the vertebrae.

To get rid of the background gradients and have a better look on the artifacts generated by the vertebrae themselves, the corrected final FM was smoothed again with a Gaussian filter of standard deviation $\sigma = 0.75$, before that the local field gradient along the z-direction of this FM was computed by taking the difference between neighboring voxels in the z-direction.

3.4.3 Multi-Echo 2D GRE Acquisition and Analysis

A transversal multi-echo 2D GRE acquisition was run on the final phantom with a resolution of $0.3 \times 0.3 \times 3.0 \text{ mm}^3$ for six echo times evenly spaced between $TE_1 = 4.75 \text{ ms}$ and $TE_6 = 48.68 \text{ ms}$. A T_2^* -map reporting the evolution of the T_2^* values within one slice was then computed by exponential fit between the echoes, similarly as in **Section 3.3.3**.

Results

4.1 Choice of the printing material

4.1.1 Material and 3D printers

The PLA sphere had a small printing resolution. The different layers of the printing process could be seen, leading to a non-perfectly spherical ball. Both the Standard White Resin, the M3 Crystal, and the nylon spheres were of good quality. Finally, the printing process of the flexible material experienced some failures, resulting in a temporary machine breakdown and an incomplete sample of the material. The nylon sample was obtained later in the thesis than the other materials, due to the unavailability of the dedicated printer before the building of the last phantom.

4.1.2 Field Map Analysis

4.1.2.1 Line Plots of the Materials

The evolution of the field inhomogeneity generated by each sphere along the three axes x , y , z is given in **Fig. 4.1**. The predicted field variations generated by an ideal sphere with a susceptibility difference with water of $\Delta\chi = 0.22$ ppm are also given as a comparison. The presence of a strong and noisy background field makes the interpretation of the line plots complicated, especially for certain materials. In particular, the field around the Flexible 80A Resin is highly affected by background variations, making it difficult to draw clear conclusions about its effect. Similarly, the effect of the nylon sample on the field is challenging to quantify. It appears to have similar effects in the B_0 direction and along the Left-Right axis as the simulated sphere, but does not create significant field variations along the vertical axis. On the other hand, the Standard White Resin and the M3 Crystal have very similar effects, generating inhomogeneities of the same magnitude and direction, both on the B_0 axis and the x - and y -axis. These two materials always produce field variations that oppose the theoretical field from the simulation. Finally, PLA generates strong field variations in the same direction as the simulated sphere.

Despite the poor quality of the flexible and PLA samples, the analysis of these line plots provided valuable insights into the effects of the different materials. The similarity between the effects of the Standard White Resin and 3M Crystal indicated that the former could be a suitable material for the subsequent experiments.

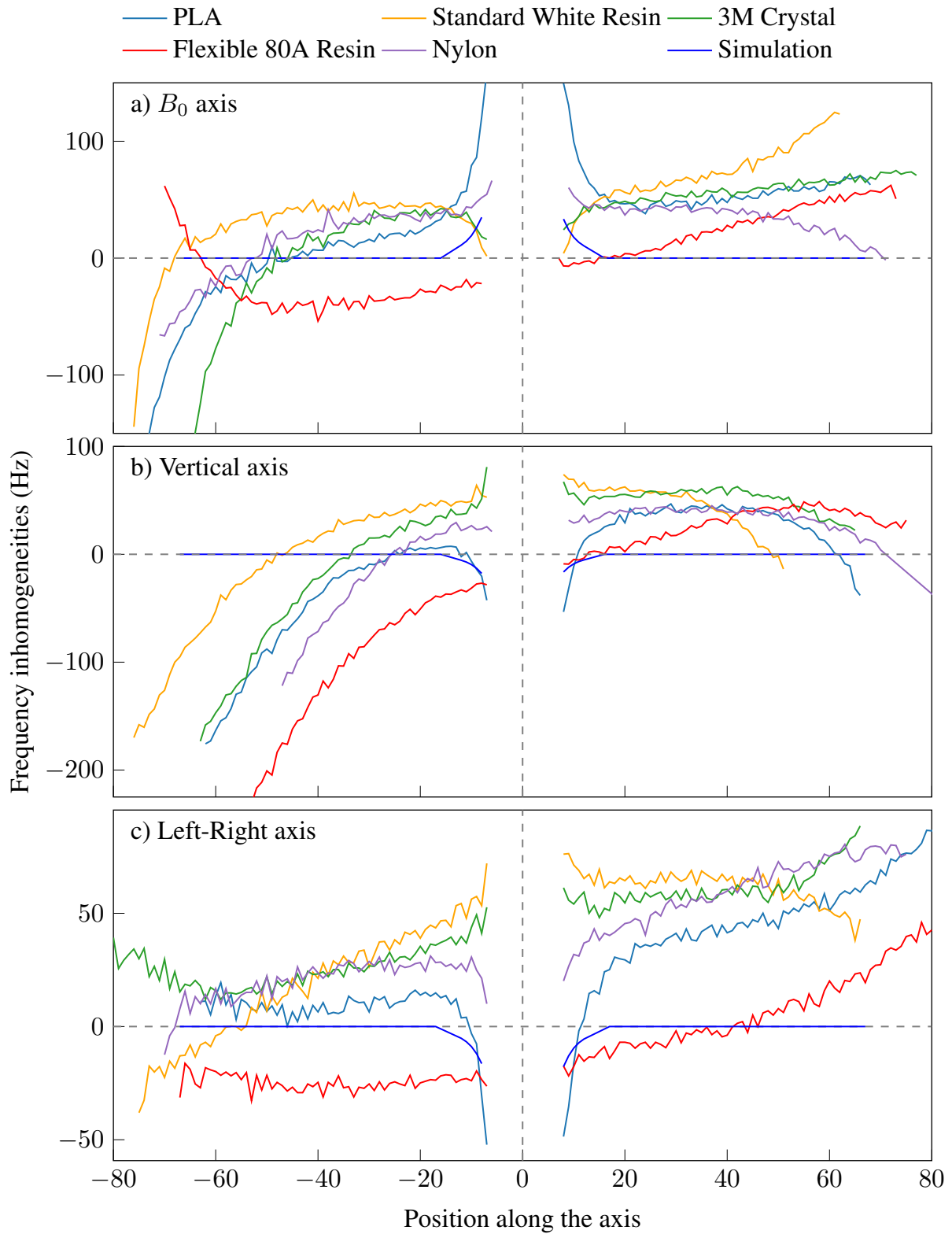


Figure 4.1: Comparison of the inhomogeneities of frequencies generated by the tested material samples along (a) horizontal axis, (b) vertical axis and (c) slice axis.

4.1.2.2 Susceptibility of the Materials

To complete the previous study of the line plots generated by each material along each direction, the estimated susceptibilities of the materials compared to the external solution of salted water are given in **Table 4.1**, based on a fit between the acquired FMs and a simulation of a perfect sphere.

Material	Slope a	Susceptibility (ppm)	R^2
PLA	227,9	0,76	0,7
Standard White Resin	- 80	- 0,27	0,6
M3 Crystal	- 42	- 0,14	0,3
Flexible 80A Resin	9,2	0,03	0.01
Nylon	49.7	0,17	0.44

Table 4.1: Susceptibility of the tested materials compared to water, found by linear regression with a Fourier-based simulation. The simulation was run on a perfect sphere with a higher resolution than what was acquired, and was then reshaped to obtain an array of similar dimensions. The slope a is used to calculate the susceptibility according to equation (3.1). R^2 is the correlation coefficient.

These susceptibility results confirmed the previous observations in **Section 4.1.2.1**, such as the similarities between M3 Crystal and Standard White Resin. With a susceptibility difference with the solution of -0.27, Standard White Resin presents an absolute susceptibility difference similar to the one between bones and tissues, close to +0.25 ppm, but with opposite signs. Nylon is the material with the closest results to the in vivo ones.

Due to cost, availability, and printing resolution considerations, described in **Section 5.3**, Standard White Resin was finally chosen as the material to print in the C3-to-C5 vertebrae, while the last final cervical phantom was printed in nylon.

4.2 Testing different additives to the solution

4.2.1 Field Map Acquisitions

4.2.1.1 Susceptibility Impact of Small Amounts of Soap

The susceptibility differences between Standard White Resin and the external solutions containing various concentrations of soap are given in **Table 4.2** and in **Table 4.3**. In **Table 4.2**, the simulation was run on a perfect sphere that was then rescaled to the dimension of the acquired image, while **Table 4.3** refers to the susceptibility values obtained by comparison with a simulation based on a magnitude mask of each material sample. In both cases, one can see that adding small amounts of soap doesn't seem to influence the susceptibility. Indeed, values of the susceptibility differences stay between -0.30 ppm and -0.27 ppm for all the studied cases. It is nevertheless interesting to note that there is considerably less error variability when the simulation is performed on a perfect sphere.

	Slope a	Susceptibility (ppm)	R^2
No soap	-85,6	-0,29	0,7
5mL soap	-84,6	-0,28	0,7
10mL soap	-83,1	-0,28	0,8
15mL soap	-84,3	-0,28	0,8

Table 4.2: Susceptibility of Standard White Resin compared to the external solutions containing various amounts of soap, found by linear regression with a Fourier-based simulation. The simulation was run on a perfect sphere with a higher resolution than what was acquired, and was then reshaped to obtain an array of similar dimensions. The slope a is used to calculate the susceptibility according to equation (3.1). R^2 is the correlation coefficient.

	Slope a	Susceptibility (ppm)	R^2
No soap	-80	-0,27	0,7
5mL soap	-92	-0,31	0,7
10mL soap	-89	-0,30	0,8
15mL soap	-91	-0,30	0,8

Table 4.3: Susceptibility of Standard White Resin compared to the external solutions containing various amounts of soap, found by linear regression with Fourier-based simulations. The simulations were run on a mask based on the magnitude of the images acquired in each case, defining each sphere using a threshold $s = 200$. The slope a is used to calculate the susceptibility according to equation (3.1). R^2 is the correlation coefficient.

4.2.1.2 Visual Inspection of the Eight Acquired Field Maps

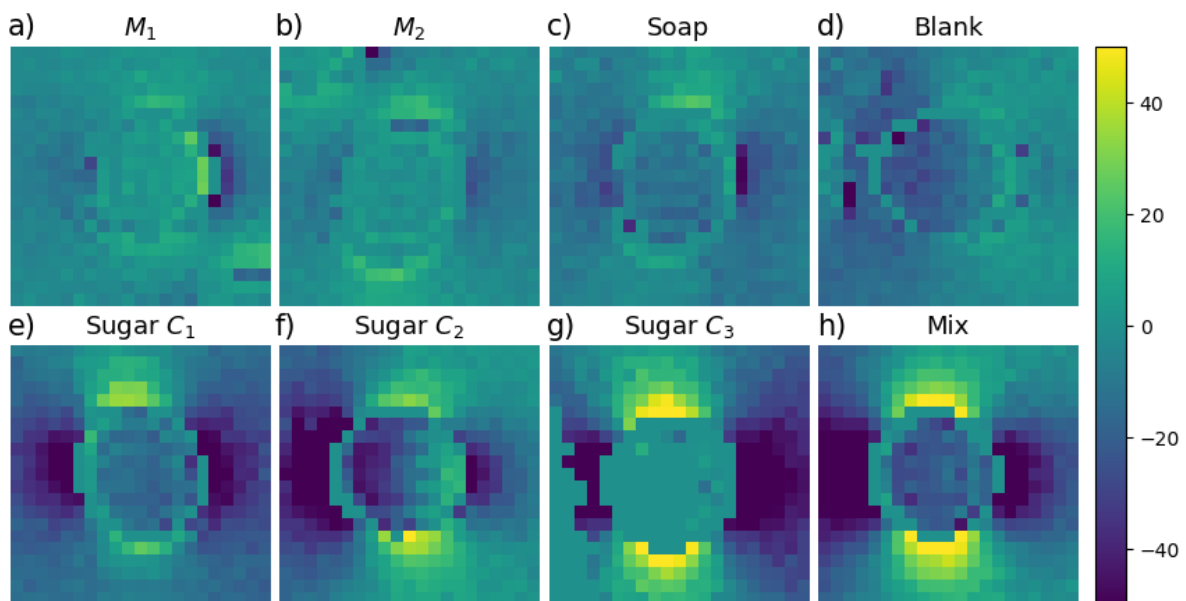


Figure 4.2: Field maps (Hz) of the eight tested solutions of mouthwash without (M_2) and with (M_1) alcohol, soap, various concentration of sugar, and the combined solution (Mix) of sugar, M_1 , and salt. The blank solution shows the effect of the plastic tube on the field.

The field maps acquired for the eight various solutions to be tested are given in **Fig. 4.2** after correction of the background. Visually, both mouthwashes and soap seem to have a negligible impact on the susceptibility effect. Indeed, their field maps are very similar to the reference one of the "blank" tube, only containing the external solution (d). The effect of this blank tube is quite small (< 20 Hz), which

allows us to consider the susceptibility impact of the solution by neglecting the impact of the tube. On the other hand, sugar seems to strongly modify the susceptibility of water. The higher the concentration of sugar, the stronger the artifacts appear. The sample containing the solution with a concentration C_3 of sugar (g) suffered from artifacts generated by the plastic layer. Therefore, the masking part of this sample covered a larger part of the generated image.

4.2.1.3 Susceptibility Effects of the Eight Solutions

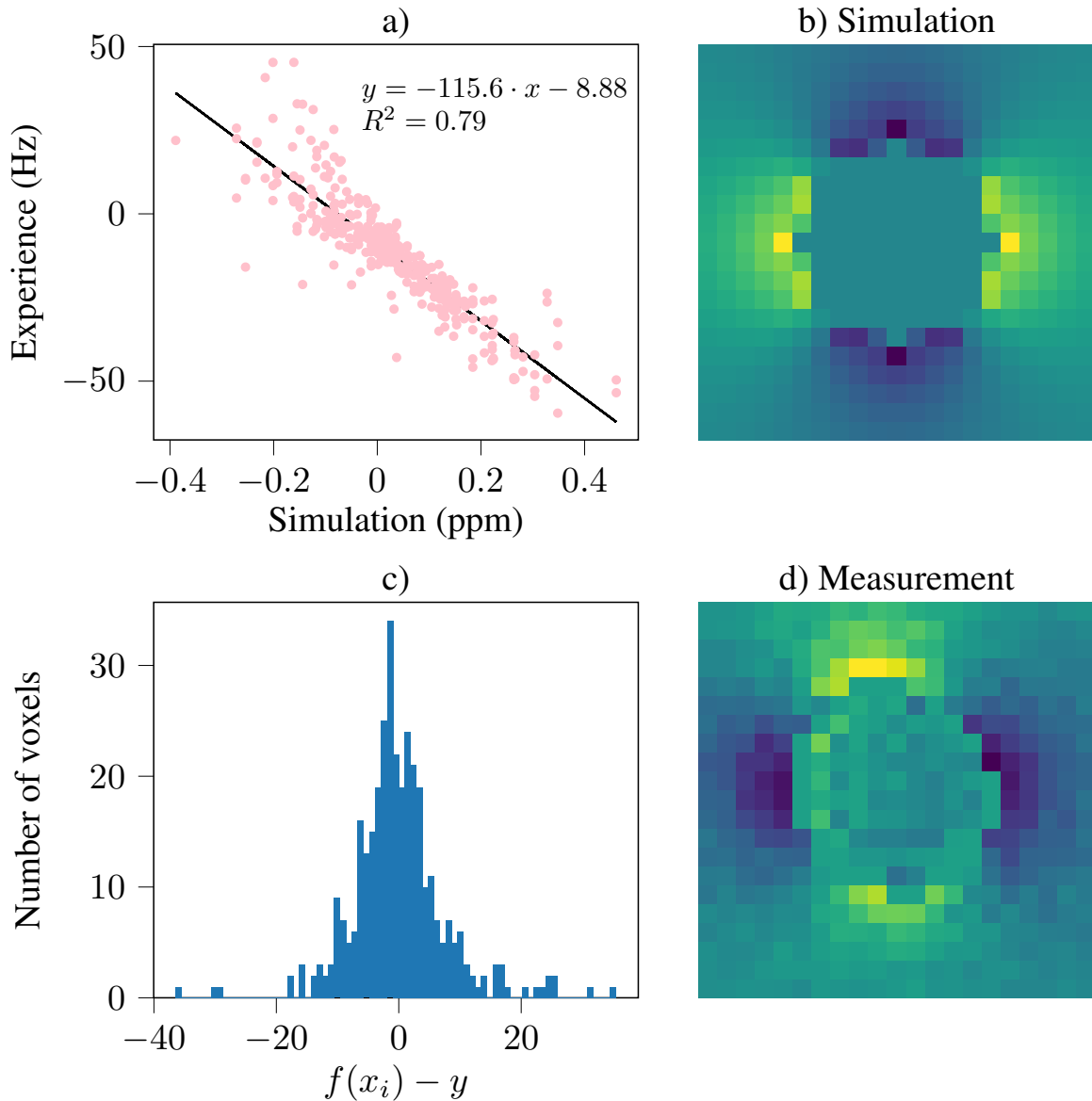


Figure 4.3: Comparison of the field inhomogeneities generated in one slice of the tested solution of concentration C_1 of sugar and a simulated cylinder. The linear regression between those two slices is presented in a). c) represents the histogram of the error $f(x_i) - y$, with y the acquired value, and $f(x_i)$ the approximate linear value obtained from the simulation using the coefficients of the linear regression. The right part of the figure represents the slice of the field map in which the linear regression was run, for both the simulation (b) and the acquired field map (d).

Fig. 4.3 illustrates the determination of the susceptibility difference between the solution containing a concentration C_1 of sugar, and the external salted water solution. The linear regression in a) between measured data fm_{exp} in Hz and simulated data fm_{simu} in ppm shows that $fm_{\text{exp}} = -115.6 \cdot fm_{\text{simu}} - 8.9$,

with a correlation coefficient $R^2 = 0.79$. The histogram of the error of this regression is given in c) and shows a Gaussian distribution, suggesting that our variance is mostly caused by Gaussian noise. This could come, as previously seen, from the external solution's background, which is not perfectly homogeneous, and from artifacts created by the plastic tube used as a container. Illustrated in b) and d) are the simulated and acquired field maps, respectively, of the chosen slice for which the regression was run.

Similar analyses were run for all the eight solutions and are summed up in **Table 4.4**. As planned, the susceptibility difference between the external solution and the blank one is very low (-0.06 ppm) with an extremely bad R^2 . That confirms the previous conclusion of **Section 4.2.1.2** that the tube has a negligible effect on the field. Both mouthwashes, especially the first one also got low susceptibility effects, comparable to the one of the tube. The soap solution had a small impact on the susceptibility difference, bringing it to -0.18 ppm. However, the amount of soap was very high ($\approx 50\%$) and is very far from the quantity we need to use in the phantoms to remove the bubbles, so we can also consider the impact of soap as negligible.

	Slope	$\Delta\chi$ (ppm)	R^2
$\approx 6\%$ of alcohol-free mouthwash M_1	-27	-0,09	0,37
$\approx 6\%$ of mouthwash with alcohol M_2	-45,6	-0,15	0,54
$\approx 50\%$ of soap	-54,9	-0,18	0,69
Blank	-18	-0,06	0,083
$C_1 = 350g/L$ sugar	-115,6	-0,39	0,79
$C_2 = 550g/L$ sugar	-143	-0,48	0,69
$C_3 = 750g/L$ sugar	-198	-0,66	0,8
Mix C_3 of sugar, 1g salt and $\approx 6\%$ of M_1	-200	-0,67	0,83

Table 4.4: Susceptibility difference $\Delta\chi$ of the eight tested solution compared to the external one, with their corresponding correlation coefficient.

The impact of the concentration C in sugar on the susceptibility difference $\Delta\chi$ between the tested and the external solutions follows a linear evolution $\Delta\chi = -0.0008 \cdot C - 0.0736$, with a correlation coefficient $R^2 = 0.9875$, which means we can linearly tune the susceptibility of water in the final external solution with sugar.

The susceptibility difference between water with and without sugar is negative, meaning, according to our convention in the choice of the simulation, that a solution with sugar and water has a lower susceptibility value than a solution of pure water. To match reality, we want the external solution to have a lower susceptibility than the vertebrae, so adding sugar will help lower the water susceptibility value.

4.2.2 Multi-Echo GRE Analysis and T_2^* Values

In this section, we analyzed the ME-GRE acquisitions of the eight studied solutions to determine if one or several of the studied substances could help decrease the T_2^* of the final phantom.

Fig. 4.4 gives an example of one of the exponential fits (a) of signal decay with TE. This fit was computed on the values of the voxel designed in b) by the intersection of the two blue lines, giving an exponential decay $y(t) = 2105 \cdot e^{-t/20.5} + 41.9$ for a correlation coefficient $R^2 = 0.990$. The slice of the voxel was selected to avoid as much as possible the artifacts generated by the plastic film used to hold the tubes. Even if the coefficient of determination is high, one can see that the fitted function does not perfectly match the measured data. It seems that some echoes have larger signal than the previous ones, as for example the magnitude of the 11th echo which is larger than the one of the 10th.

The resulting mean T_2^* value of each solution was then calculated. These values and their associated standard deviations and selecting parameters are summed up in **Table 4.5**.

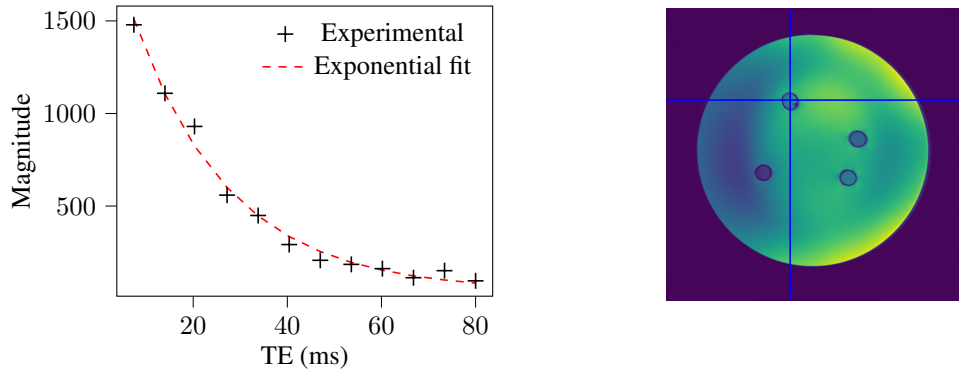


Figure 4.4: (left) Exponential fit of the T_2^* -value in one voxel of the solution with a concentration C_1 of sugar. The voxel is given by the intersection of the blue lines in the representation of the first echo ($TE = 7.40$ ms) in the right.

	T_2^*	Std	$\frac{Std}{Mean}$	N_{R^2}	$N\%$	R_{min}^2
$\approx 6\%$ of alcohol-free mouthwash M_1	563,3	332,9	59%	46	15%	0,93
$\approx 6\%$ of mouthwash with alcohol M_2	890,70	174	20%	20	7%	0,93
$\approx 50\%$ soap	236,30	16,1	7%	197	65%	0,97
Blank	747,00	172	23%	17	6%	0,9
$C_1 = 350g/L$ sugar	20,95	0,89	4%	140	46%	0,99
$C_2 = 550g/L$ sugar	9,33	0,53	6%	176	58%	0,98
$C_3 = 750g/L$ sugar	7,97	0,55	7%	168	55%	0,98
Mix C_3 of sugar, 1g salt, $\approx 6\%$ of M_1	26,24	1,07	4%	279	91%	0,98
External solution acquisition 1 (soap)	976,2	210	22%	194	2%	0,96
External solution acquisition 2 (sugar)	784	203	26%	396	5%	0,96

Table 4.5: Computed mean T_2^* values of the eight tested solutions and of the external solution. Each T_2^* value was calculated between voxels of one selected slice inside a circular ROI of radius $r = 10$ voxels centered in the middle of the examined tube, excluding all values with a coefficient of determination inferior to the chosen R_{min}^2 . The standard deviation, and the number and percentage of selected voxels inside the studied ROI are respectively given by Std, N_{R^2} and $N\%$.

4.3 Spherical Phantoms

4.3.1 Building the Phantoms

Two different printing orientations of the C3-to-C5 vertebrae were tested, as illustrated in **Fig. 4.5**. Printing the vertebrae horizontally resulted in small irregularities (circled in red) inside the spinal canal and in between the vertebrae, leading to artifacts in the acquired FMs. By reorienting the vertebrae to a vertical position during the printing process, those artifacts were greatly reduced.

For the second phantom, the entire outer surface of the spherical plastic container was successfully coated with fiberglass and epoxy, solidifying the structure. However, the coated sphere suffered from protrusions on the intersection between the different pieces of fiberglass. The epoxy that was applied to the inside surface of the container did not present any major trouble, spreading correctly and evenly over the entire surface. Nevertheless, as the epoxy solution used was rather liquid, some of the epoxy from the upper part flowed by gravity to the lower part of the sphere during the drying phase. Based on this consideration, a slightly less liquid solution was therefore preferred when applying the epoxy to the final phantom.

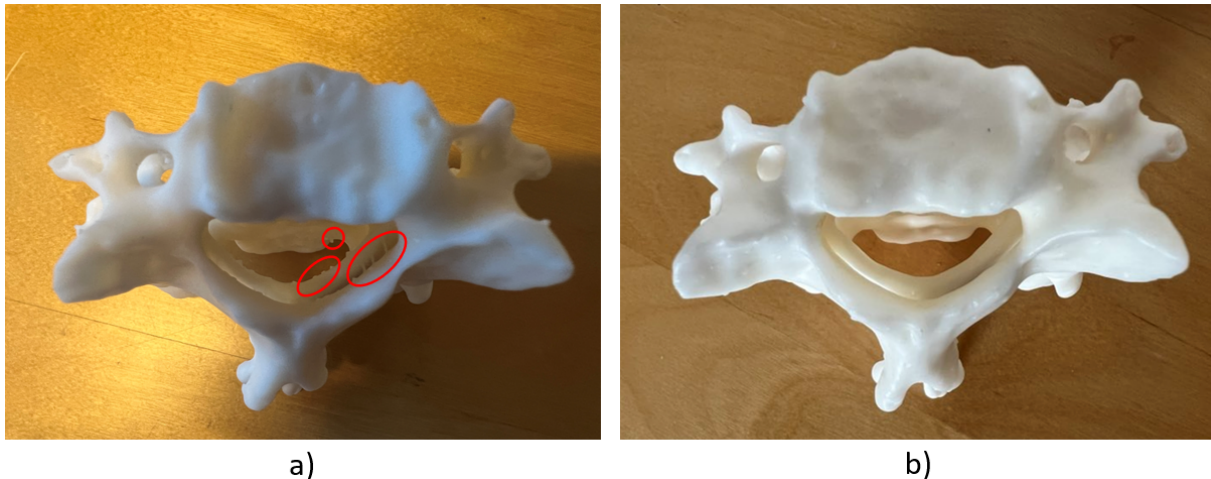


Figure 4.5: Comparison of the quality of the spinal cord canal between two different printing orientation choices. In a), the C3 to C5 vertebrae were printed horizontally, to minimize the printing time, whereas in b), they were printed upright making it easier to access the support and remove it.

4.3.2 Analysis of the Field Maps

4.3.2.1 Background Correction Techniques

Fig. 4.6 illustrates the different correction methods that have been tried on the first phantom to correct for the background inhomogeneities, mainly due to the external shell. The color scales of all the field maps were adjusted to the same range for easier comparison. **Fig. 4.6 a)** shows the uncorrected FM. Nothing can be seen on the image, whose scaling is not centered on zero because of the non-zero background. On **Fig. 4.6 b)**, one can see that removing the mean background value allowed the FM to become readable, and the susceptibility artifacts inside the vertebral canal start to appear. Unfortunately, the figure is degraded by a strong gradient between the different corners of the image. The lower left corner, and more generally the lower part of the image, suffers from high values, while the upper part is characterized by very negative values of field inhomogeneities. In all the following correcting methods, the mean value of the studied corrected FM was computed and subtracted to the corrected FM to recenter them, in order to be able to compare them more easily.

Shape functions inspired from the finite elements were then tested in **Fig. 4.6 c)** and **d)**, respectively in 3D by choosing nodes in the eight corners of the 3D matrix, and by computing it in 2D for each sagittal slice. These two methods were unable to help correct the image, probably because of too much field variability in the background and of the choice of an insufficient number of nodes. However, the choice of nodes was limited, because they could not be taken too close to the vertebrae, for fear of correcting inhomogeneities created by the vertebrae and that we wanted to observe. Moreover, increasing the number of nodes greatly increased the computation time.

In **Fig. 4.6 e)**, a linear gradient correction method was tested and shown to be slightly more effective than the previous methods. Indeed, the intervertebral artifacts can still be observed, while the background seems more homogeneous, even if the inferior left corner still suffers from high inhomogeneity values.

Subtracting the reference background to the uncorrected FM, as was done in **Fig. 4.6 f)** was shown to be the best method we tested. The background doesn't seem to be influenced by container gradients anymore. Some noise between the voxels still remains.

The FM corrected with the reference background was then soothed with different standard deviation values as **Fig. 4.6 g)** and **h)** illustrate, to try to remove the noise. In **Fig. 4.6 g)** the standard deviation was put to 0,5 voxels, and resulted in a smoothed FM, with reduced background noise. In **Fig. 4.6 h)**, finally, one can see that the chosen standard deviation of 1 voxel led to a strong blurring of the image, and is therefore too much.

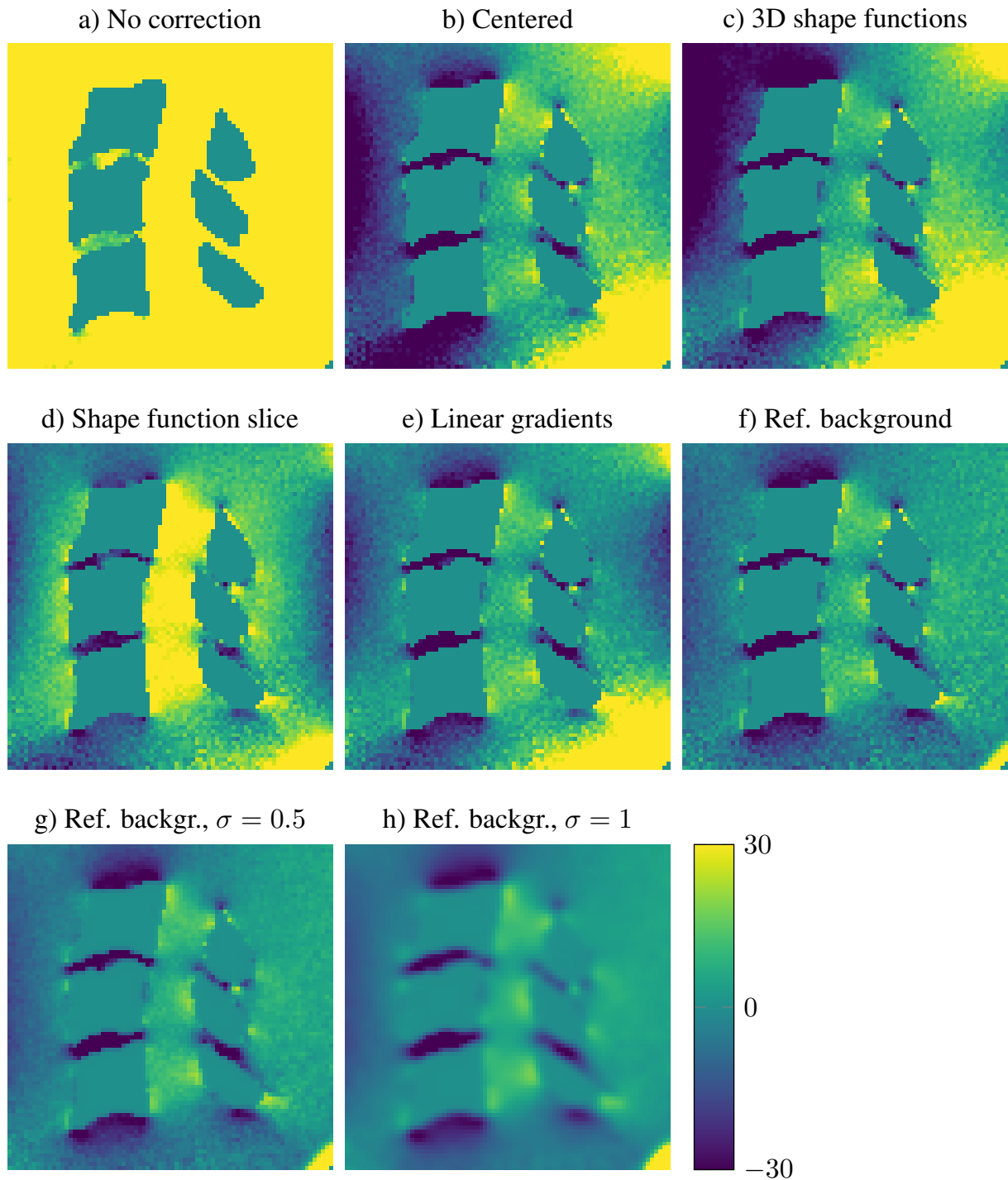


Figure 4.6: Original acquired FM of the first C3 to C5 phantom (a), and the various tested correction methods to remove the background inhomogeneities.

In the following sections, the reference background subtraction, followed by a recentering and a smoothing with a standard deviation $\sigma = 0.5$ voxels, was chosen to be the background correction method.

4.3.2.2 Susceptibility Difference

First spherical phantom: The linear regression between the simulated and the acquired field maps was first run by taking into account the artifacts created all around the vertebrae, on the entire reshaped matrix space as was shown in the previous section by **Fig. 4.6**. However, due to strong background field, probably due to the shape of the container, the result of the regression was very noisy, and the associate coefficient of determination was only $R^2 = 0.30$. To limit this effect, the area of interest of the regression was then limited to the intervertebral canal, as defined by the yellow frame in **Fig. 4.7 c)** and **d)** showing the selected region in the sagittal and transverse planes respectively. This technique was quite efficient and allowed the result shown in **Fig. 4.7 a)**. A slope $y = -73.2 \cdot x - 0.87$ was found for a coefficient of determination R^2 increased to 0.76. According to the histogram presented in **Fig. 4.7 a)**, the error is mainly due to Gaussian noise.

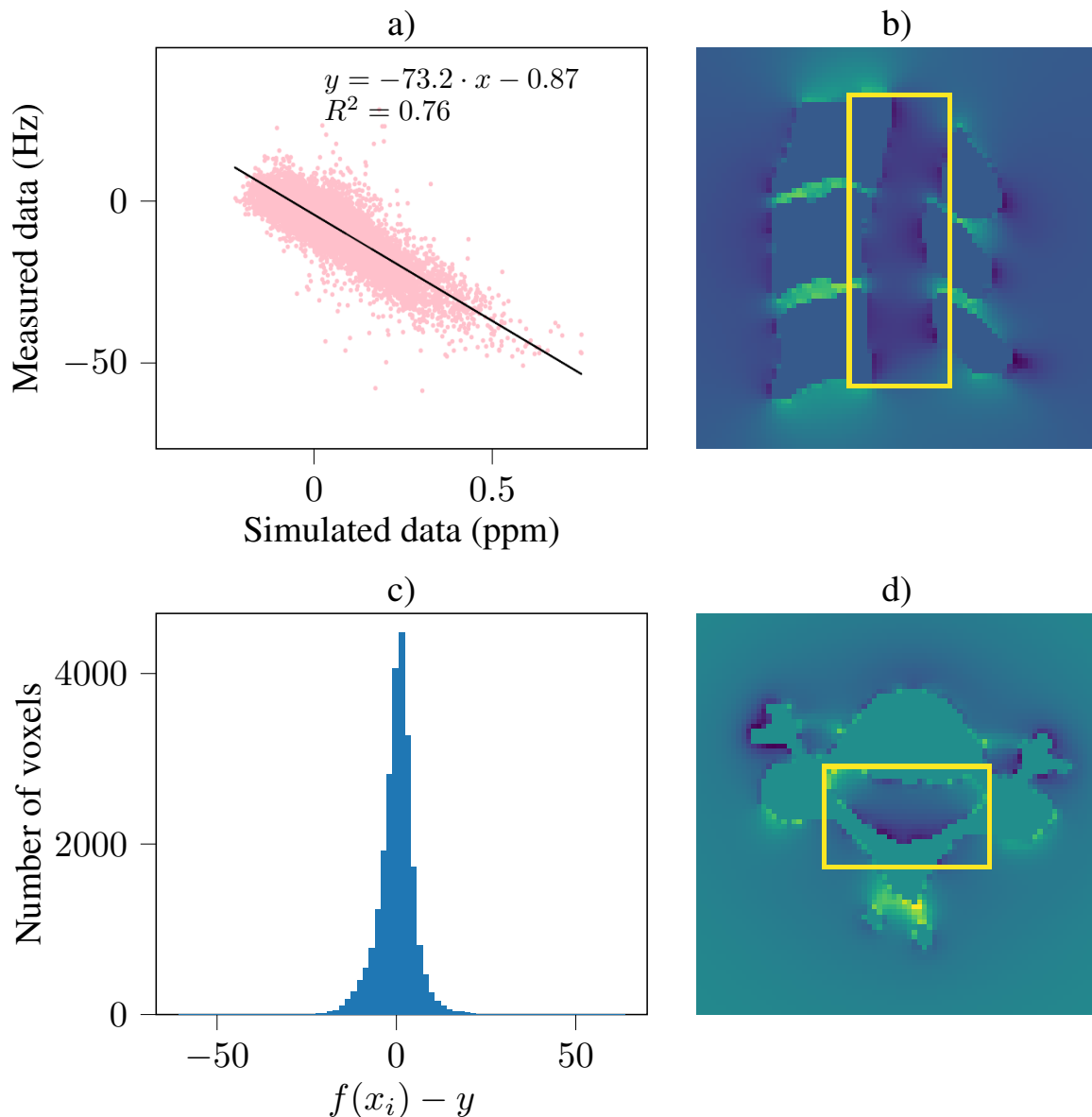


Figure 4.7: a) Linear regression between the simulated and measured data of the first phantom. The region of interest of the regression was chosen to be the voxels inside the volume defined by the yellow lines in both the sagittal (b) and transversal (d) planes, and which are not inside the vertebrae. c) gives the histogram of error between the linearly predicted $f(x_i)$ and measured data y .

The susceptibility difference between the vertebrae and the external solution is then -0.244 , according to equation (3.1). This value is close to the one given in **Table 4.1**, previously found when comparing a similar solution to a small spherical sample of Standard White Resin ($\Delta\chi = -0.27$). Indeed, the relative error between the two values is

$$\left| \frac{\Delta\chi_{\text{sample}} - \Delta\chi_{\text{vertebrae}}}{\Delta\chi_{\text{sample}}} \right| = 8.5\% \quad (4.1)$$

This confirms the consistency of the results between the two experiments. To match the susceptibility difference between bones and tissues, we ideally expect a experimental susceptibility difference $\Delta\chi$ between $+0.19$ and $+0.25$ (Schenck, 1996). Here, the absolute value of the experimental susceptibility difference matches the expectations, but not its relative value. Even if a sign can easily be inverted, we can't be totally satisfied with this result, as we would like, in a later stage of this project, to take into account the susceptibility impact of air.

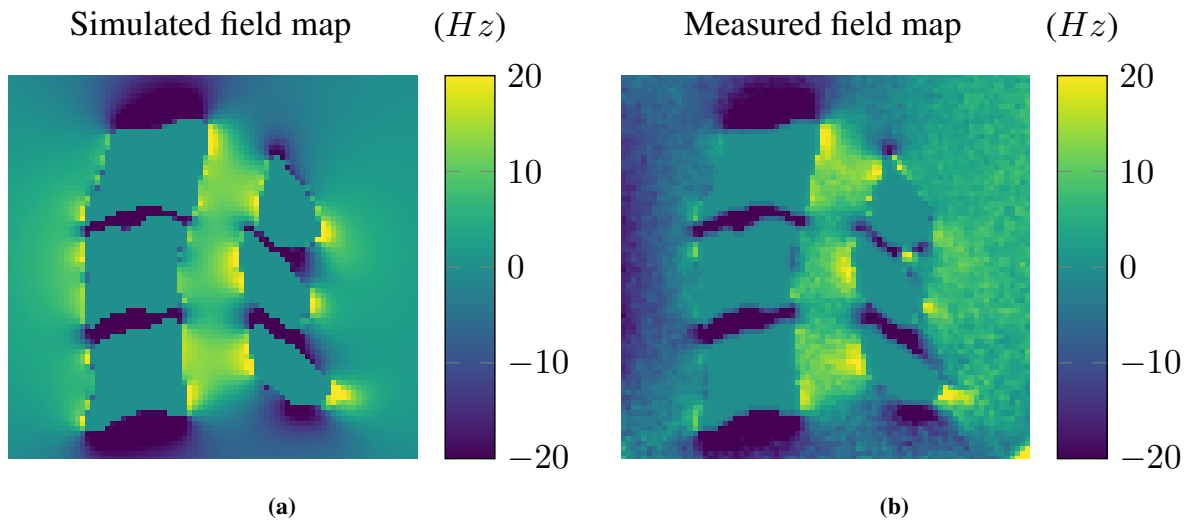


Figure 4.8: Comparison of the simulated and the measured field maps, in a sagittal slice. The simulated field map (a) was computed by assigning a susceptibility difference of 1 ppm between vertebrae and water. It was then rescaled to Hz using the susceptibility value difference between Standard White Resin and the external solution predicted with the analysis of the material in **Section 4.1.2.2**. The acquired field map (b) is shown in Hz after background field correction. The values inside the vertebrae are masked.

The susceptibility difference value between Standard White Resin and the external solution predicted with the analysis of the material in **Section 4.1.2.2** was chosen to scale the simulated FM to Hz . It was preferred to the value found with the vertebral linear regression, as it was computed on the full 3D array, whereas the region of interest had to be decreased for the vertebrae in order to limit the noise, and that the resulting value depended a lot from the chosen volume of interest. The rescaled simulated FM and the acquired one can be seen in **Fig. 4.8**.

One can visually assess the similarity between the two FMs. Qualitatively similar field patterns were observed in the simulated and acquired FMs, with low fields between the vertebrae, and high fields in front of each spinal process, creating alternating fields along the spinal canal.

Second spherical phantom: The results of the linear regression between the acquired and simulated FMs of the second phantom are shown in **Fig. 4.9** in a similar format than for the previous phantom. The linear correlation (a) was computed inside the vertebral canal as illustrated by the yellow frames in the sagittal (a) and transversal (b) views of the simulated FM. The computed relationship between simulation

and measurement was this time found to be $y = 68.5 \cdot x + 81.04$, for a coefficient of determination $R^2 = 0.40$.

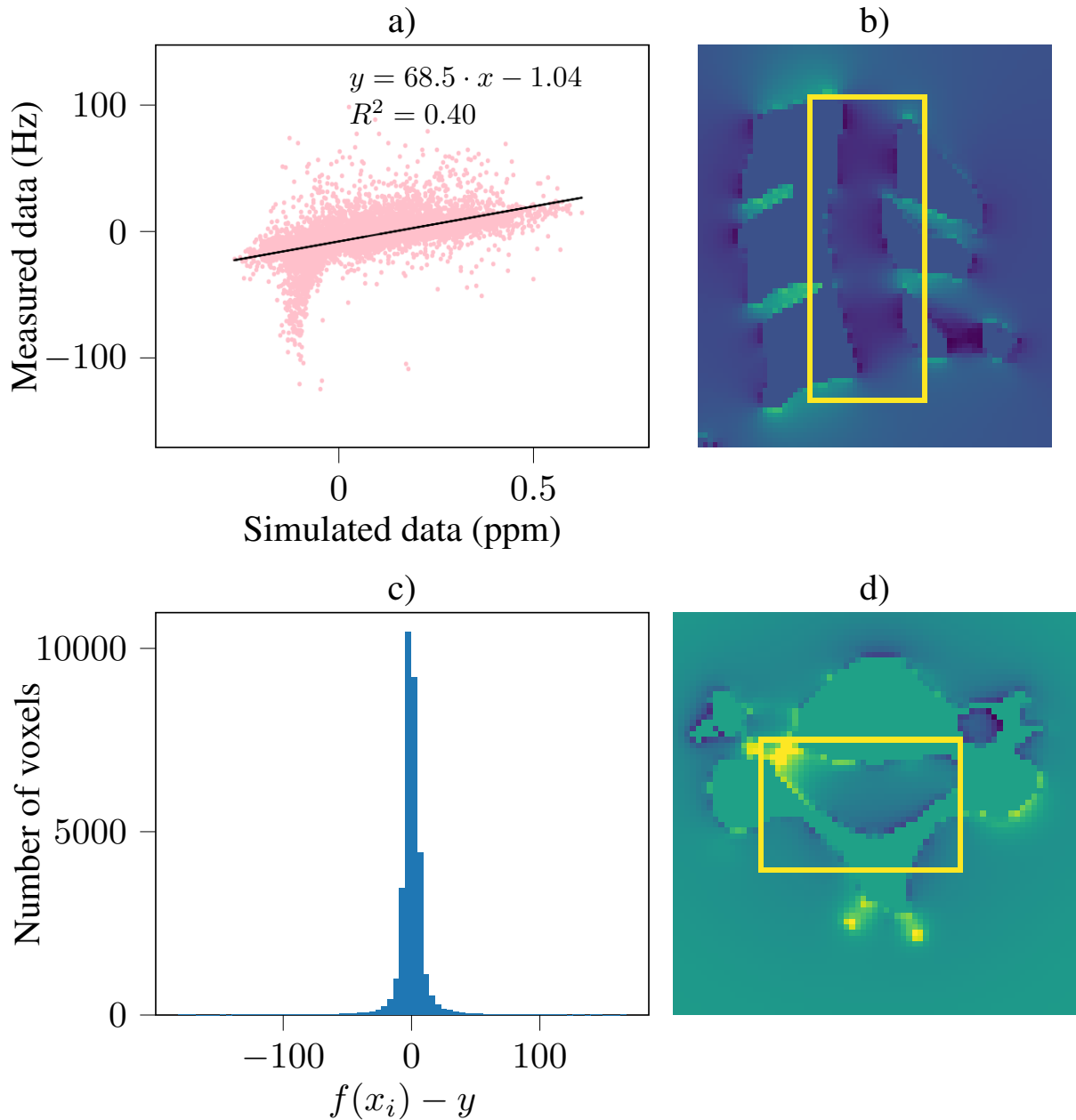


Figure 4.9: a) Linear regression between the simulated and measured data of the second C3 to C5 phantom. b) and d) show the sagittal and transversal views of the simulated vertebrae in ppm. The region of interest of the regression was chosen to be the voxels inside the volume defined by the yellow lines in both the sagittal (b) and transversal (d) planes, which are not inside the vertebrae. c) gives the histogram of error between the linearly predicted and measured data.

Given equation (3.1), the susceptibility difference between the printed vertebrae and the sugary external solution is $\Delta\chi = +0.23$ ppm, which corresponds to the value we are looking for to reproduce the in vivo vertebrae / tissues susceptibility difference.

For this phantom, the variability is much higher than for the phantom using an external solution without sugar, whose R^2 was 0.76 (**Fig. 4.7**). Nevertheless, the simulated and the measured fields showed a highly significant correlation with a p-value $p < 0.001$. When looking at the shape of the

correlation function, one can visually see a good correlation for the positive values of the simulated field, with a Gaussian dispersion similar to the one observed in the previous phantom. This is confirmed by the Gaussian distribution of the error in **Fig. 4.9 c**). Once again, this variability may be due to noise and residual background fields in the measured FM, as well as discretization errors close to bone/soft tissue interfaces in the simulated FM. An incomplete dissolution of the sugar in the solution could also partially explain some of the variability. A peak in the dispersion of the measured values can be seen at negative values of the simulated FM, as if an artifact with very negative field strength values disturbed the measured FM. This surprising artifact can be visually observed in the representation of measured FM in **Fig. 4.10b** on the posterior part of C3. A small imperfection in the posterior part of C3 can be observed by a careful inspection of the printed vertebrae, as illustrated in the appendix, in **Fig. 7.1**. This small hole, which felt slightly sticky to the touch, could explain the presence of this artifact due to an inhomogeneous accumulation of sugar in this position. Despite this, one can again observe similar patterns of periodic signal loss with higher fields between vertebrae and lower fields in front of each vertebral process, even if some of these are obscured by the inhomogeneity around C3.

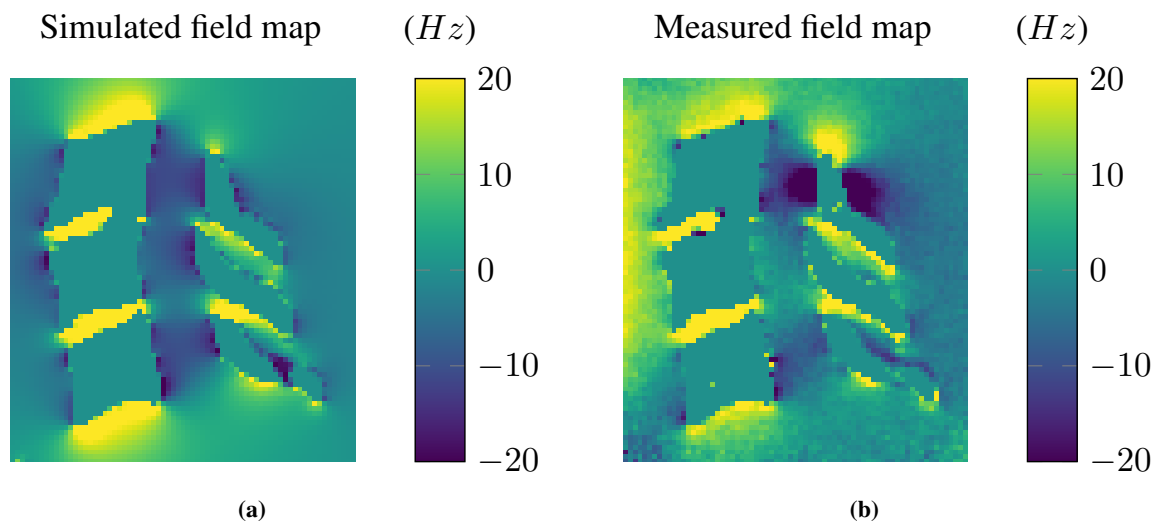


Figure 4.10: Comparison of the simulated and the measured field maps of the second C3 to C5 phantom, in a sagittal slice. The simulated field map (a) was computed by assigning a susceptibility difference of 1 ppm between vertebrae and water. It was then rescaled to Hz using the susceptibility value difference between the vertebrae and the external solution found by linear regression between the acquired and simulated FMs, restricted to the spinal cord canal. The acquired field map (b) is shown in Hz after background field correction. The values inside the vertebrae are masked.

4.3.2.3 Z-Gradients

First spherical phantom: **Fig. 4.11** shows the local field gradients in the z-direction, for both the rescaled simulated FM, and the measured data of the first phantom. Alternating positive and negative field gradients can be observed posteriorly in the spinal canal, around each intervertebral junction, in both measurement and simulation. The absolute values of the field gradients (**Fig. 4.11 c**) and d)) show zero points extending from the center of each intervertebral junction, with large local field gradients above and below.

Second spherical phantom: **Fig. 4.21** illustrates the local field gradients in the z-direction of the vertebrae in water and sugar. In the measured gradient (right), the anterior part of the canal shows the same alternating fields along the spinal canal as observed with the first phantom and in the simulation

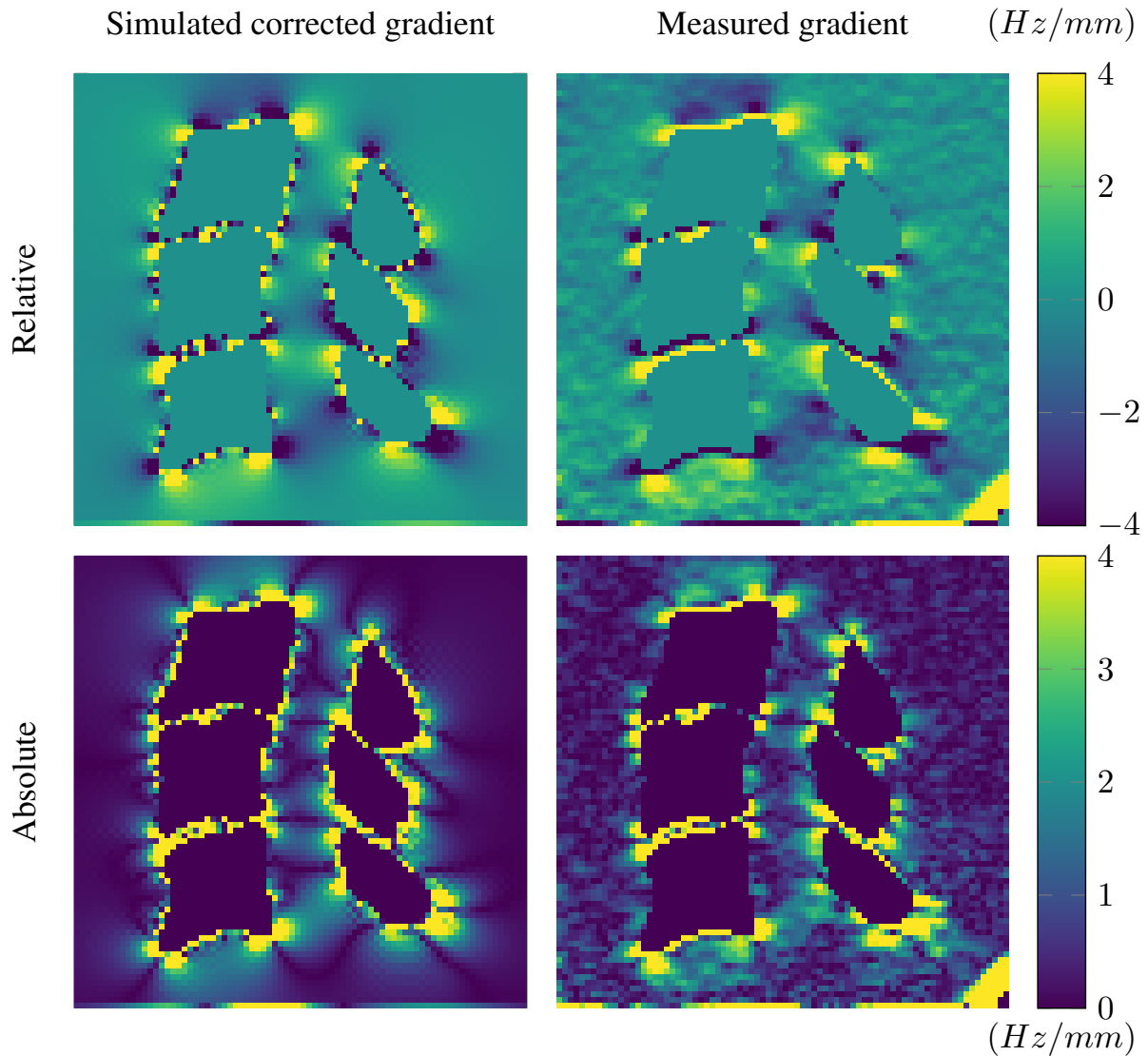


Figure 4.11: Comparison of local field gradients (upper part), and absolute values of the gradients (lower part) along the z-direction for both the simulated (left) and the measured (right) field maps. The simulated gradient has been rescaled to Hz/mm using the susceptibility value difference between Standard White Resin and the external solution predicted with the analysis of the material in **Section 4.1.2.2**.

(left), both in absolute and relative values. Posteriorly, the field gradient along C4 and C5 is also very similar in the simulated and acquired images. However, the artifact on the posterior part of C3 that we already observed in **Fig. 4.10** is again highly visible and greatly disturbs the local gradient around it.

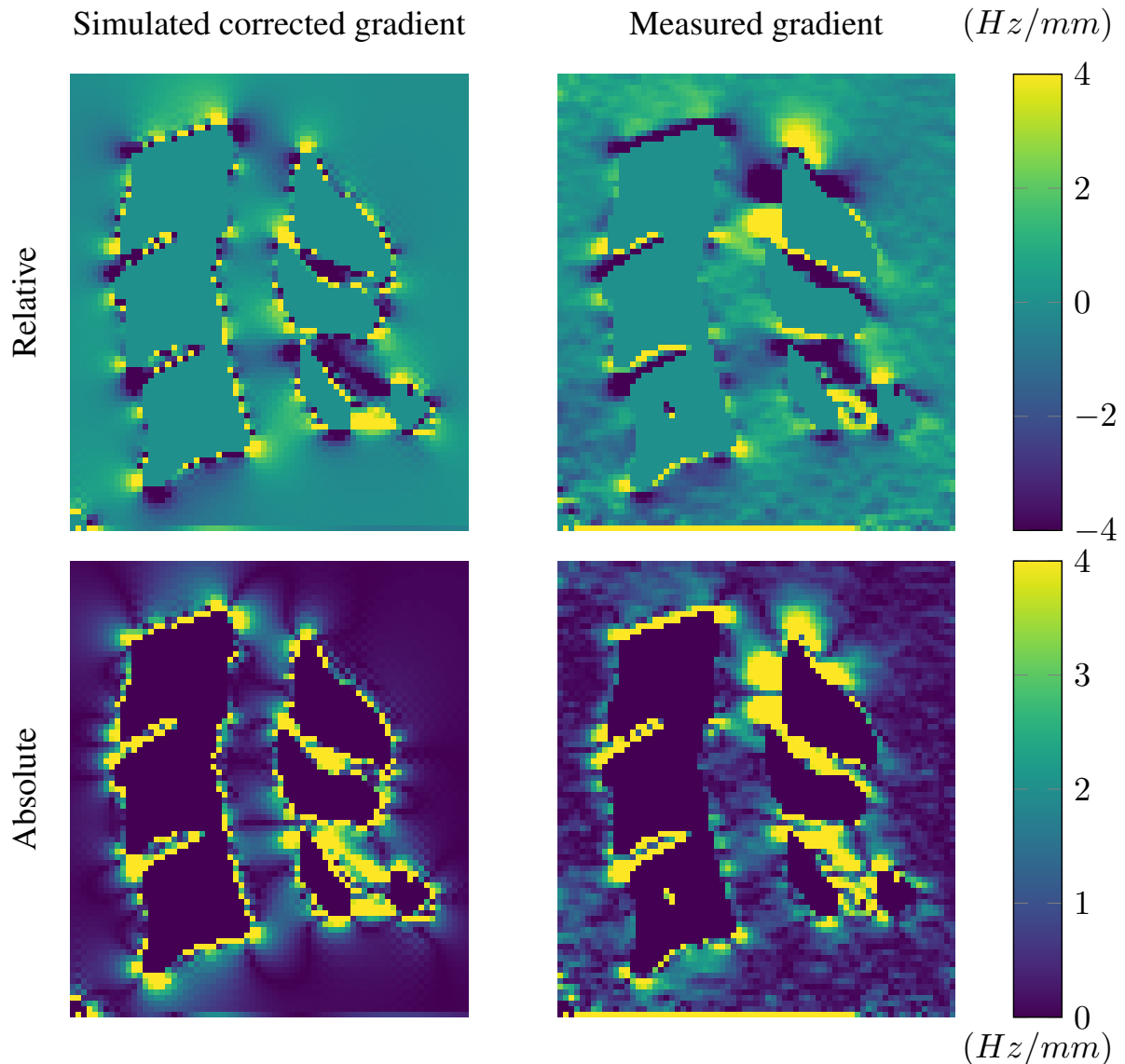


Figure 4.12: Comparison of local field gradients (upper part), and absolute values of the gradients (lower part) along the z-direction for both the simulated (left) and the measured (right) field maps of the second vertebral phantom.

4.3.3 Multi-Echo GRE Analysis

4.3.3.1 Visual Comparison With in vivo Data

First spherical phantom: Fig. 4.13 shows the first phantom multi-echo GRE images from two selected slices, in the C4/C5 intervertebral junction, and mid-C4. For comparison, two slices (mid-C3 and just above C3/C4) from an in vivo acquisition are shown in the left part of the figure. The slices near an intervertebral junction show drop-out along the rim of the spinal canal, particularly towards the posterior edge. However, the acquired data shows more loss along the anterior side than can be seen in the in vivo data. Differently to the slices around a vertebral junction, the ones centered on a vertebra instead suffer from drop-out coming in from the sides anteriorly. The sagittal view (Fig. 4.13 e) shows the periodicity of the signal drop-out related to the vertebrae.

A notable difference between phantom and in vivo data was that the signal loss appeared at earlier echo times in the in vivo data.

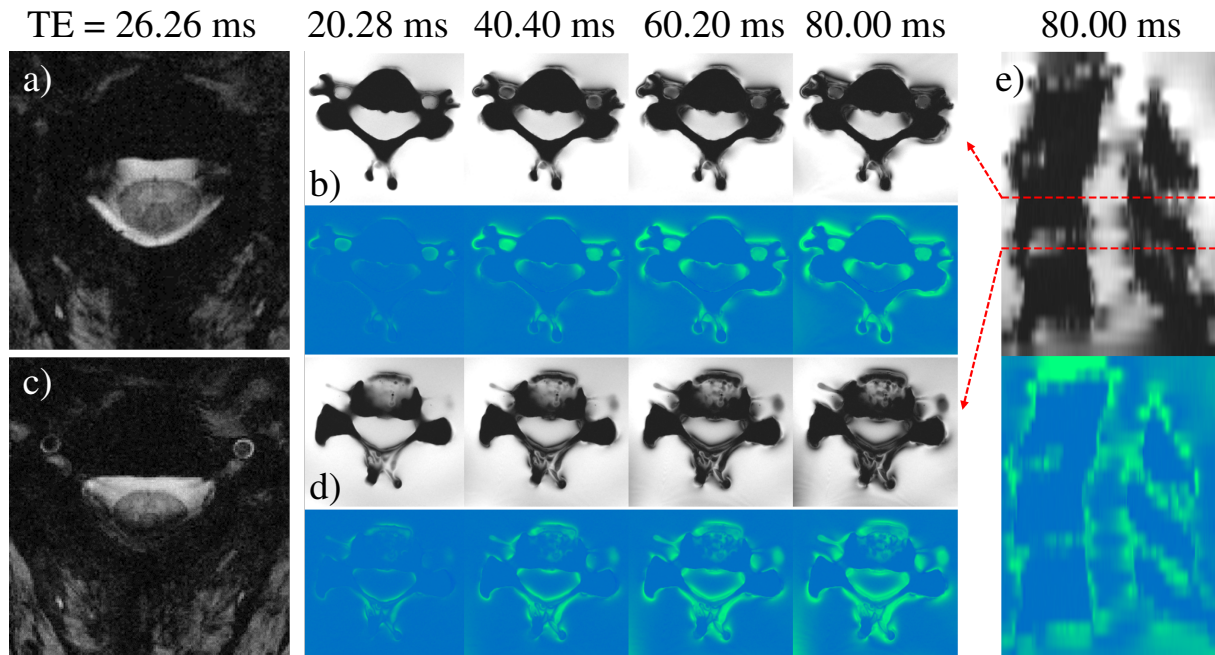


Figure 4.13: Representative slices from an in vivo GRE acquisition (a,c), located mid-vertebra (a) and above an intervertebral junction (c) showing different patterns of signal drop-outs. Corresponding slice locations in the C3 to C5 first phantom (b,d) show increasing signal drop-out with increasing TE, resembling the in vivo pattern. For the phantom data, the difference to the first echo, acquired at $TE_1 = 7.40$ ms, is shown below the magnitude image for each echo. The last echo of the phantom data is shown in a sagittal view (e) demonstrating the periodicity of the signal drop-out.

Second spherical phantom: The evolution of the signal of the second spherical phantom between the different echo times from $TE_1 = 20.28$ ms to $TE_{12} = 80.00$ ms was computed for some selected slices. The top C5 slice, that we already looked at in the first C3 to C5 phantom in **Fig. 4.13 d**), is represented for the second phantom in **Fig. 4.14**. The echoes are arranged in ascending order from left to right, row by row. The first one is in the top left corner, and subsequent images follow this order: top row second column, top row third column, top row fourth column, second row first column, and so on. All the echoes are scaled to the same colorbar presented on the right. Similarly that in the previous phantom, this slice shows a drop-out along the rim of the spinal canal, which is especially visible along the posterior edge. In the first phantom, a large drop out along the anterior edge was also present, but is less visible here, where the images are closer to the in vivo slices around intervertebral junctions. The decline of the signal appears much earlier than previously, suggesting that the sugar greatly reduced the relaxation time T_2^* , as expected.

Contrary to what was expected, the signal's decrease does not seem to follow perfectly an exponential decrease. It can be noticed that echo 9 (3rd line on the left) is much darker than its successor, suggesting that some signal has returned, and spins have been rephased partially, which is somewhat counterintuitive. This non-exponential signal decay effect had already been noticed in the study of the different solutions, and especially of the solution of water and sugar in **Fig. 4.4**, although to a lesser extent.

4.3.3.2 T_2^* -Values

First spherical phantom: The calculation of the relaxation time of the voxels with $R^2 > 0.9$, inside a circle of radius $r = 40$ voxels in the external solution of salt, water, and soap showed that the mean T_2^* -value of the solution seems to be around **630 ms \pm 300 ms** (587 voxels were defined as satisfying all the inclusion criteria). This value confirmed the observation of the previous **Section 4.3.3.1** that the

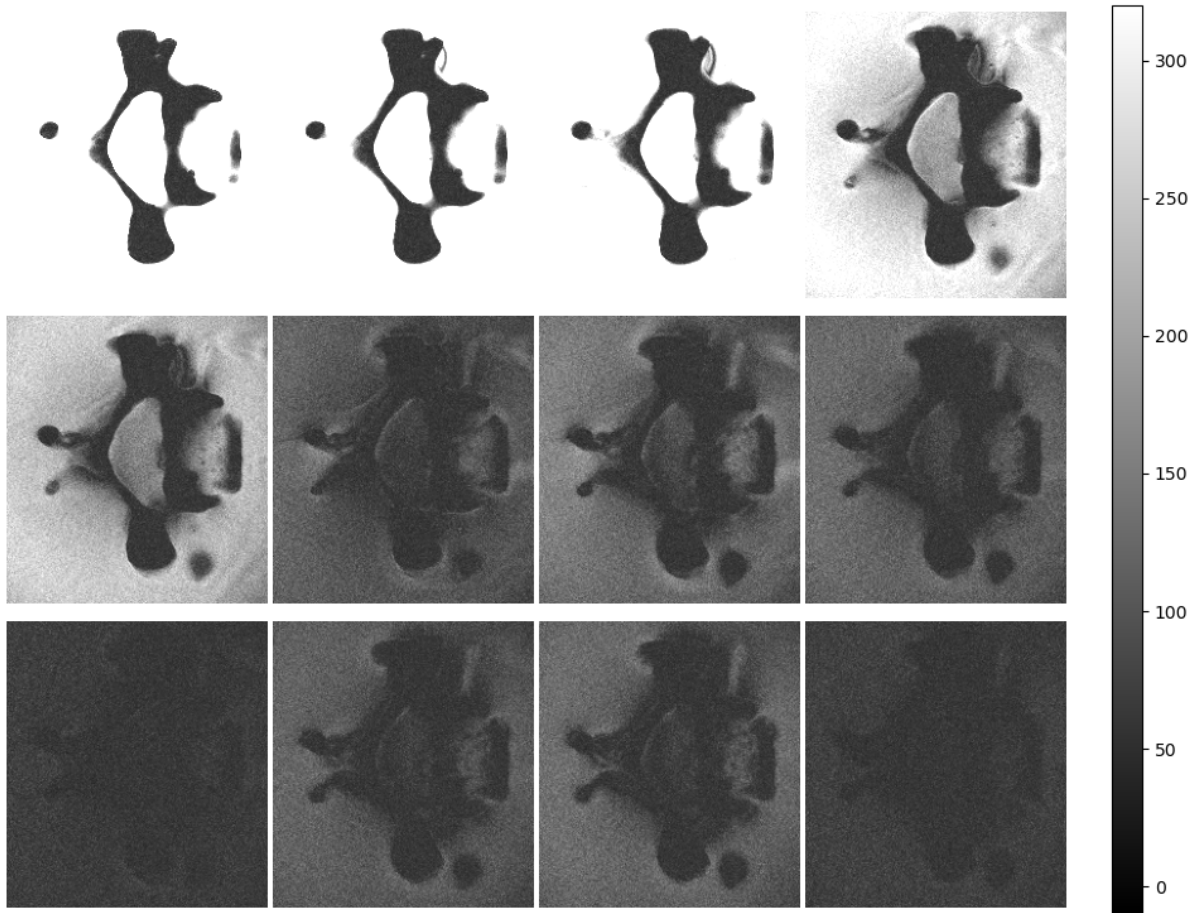


Figure 4.14: Illustration of the evolution of the signal of the second phantom, on a transversal slice along the 12 evenly spaced echoes, from $TE_1 = 20.28$ ms to $TE_{12} = 80.00$ ms. The echoes are arranged in ascending order from left to right, row by row. The first one is in the top left corner, and subsequent images follow this order: top row second column, top row third column, top row fourth column, second row first column, and so on. All the echoes are scaled to the same colorbar presented on the right. The represented slice is situated in the top C5, similarly as the one presented in **Fig. 4.13 d**).

transversal relaxation time is much bigger than in vivo (± 20 to 50 ms (Peters et al., 2007)), leading to earlier signal loss in vivo. The uncertainty of the computed T_2^* is very high, and most of the voxels could not satisfy the minimal determination coefficient condition. That can probably be explained by the very long relaxation time compared to the chosen TE of the 12 acquired echoes. Reducing the solution's relaxation time should reduce this issue.

Second spherical phantom: In this second C3 to C5 phantom with a sugary external solution, the mean transversal relaxation time was found to be $T_2^* = 12.1$ ms. As expected from the study of the different solutions in **Section 4.2.2**, adding sugar did greatly reduce the relaxation time of the solution. However, for such a concentration of about 350 g of sugar for 1L of water, we expected from **Table 4.5** a slightly higher T_2^* , between 20 ms (case water + sugar) and 27 ms (case water + sugar + mouthwash). In the final phantom, to perfectly match the expected in vivo relaxation time $T_2^* \approx 40$ ms (Peters et al., 2007), it would be needed to use less sugar. The upper part of the T_2^* map suffers from the appearance of inhomogeneities resembling a liquid flow, suggesting a possible mis-mixing between the components of the solution.

As the T_2^* was greatly reduced, and is now lower than the TEs used in the ME-GRE acquisition, the variability between the computed T_2^* of the voxels was drastically reduced, with a standard deviation

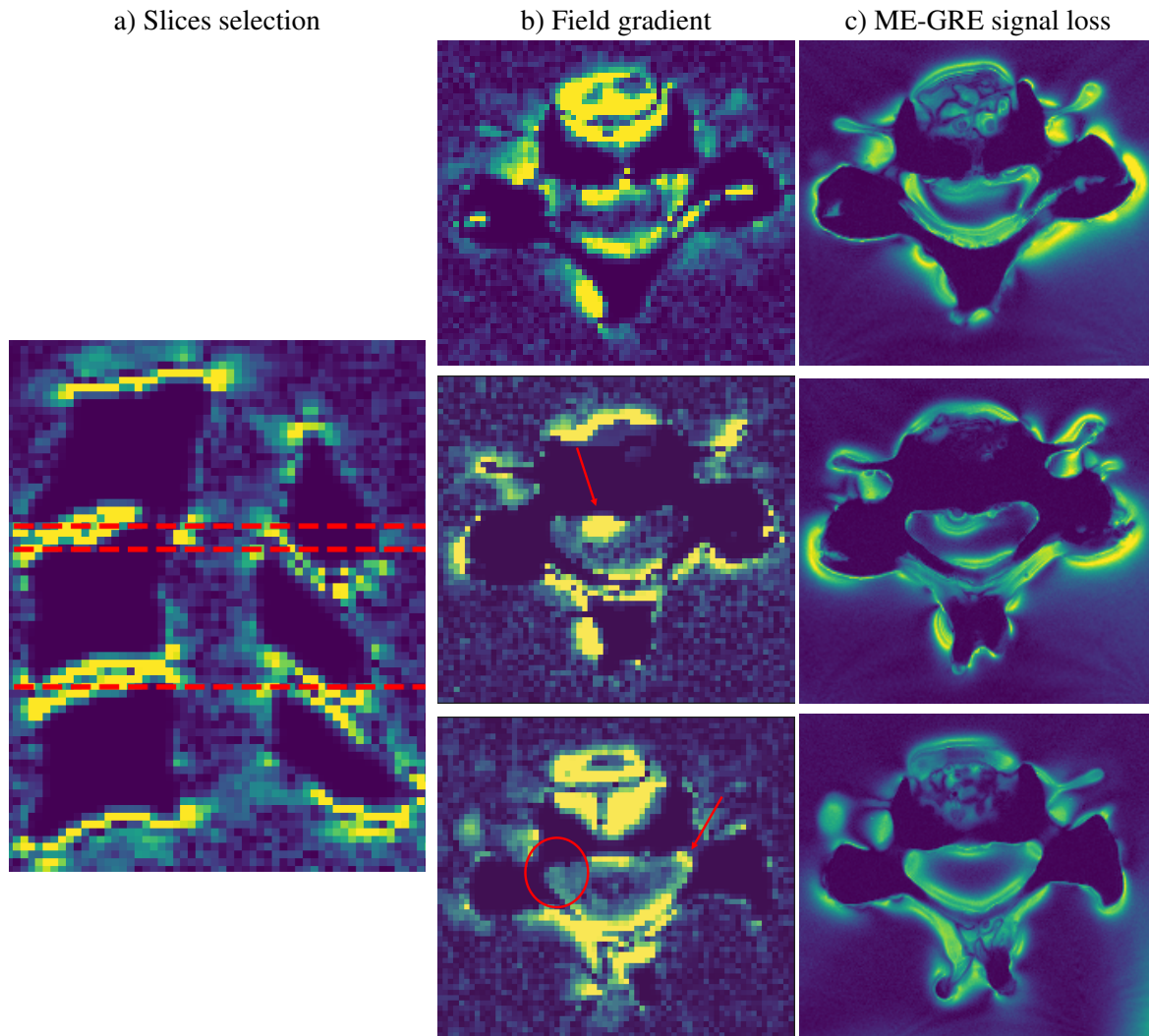


Figure 4.16: Comparison of the field gradient (a,b) with the ME-GRE loss (c). Three different transversal slices are shown: from top to bottom of the image, one can see a mid-C3/C4 slice, an upper C4 slice and a mid-C4/C5 slice. Their localization is shown in the sagittal view in a) by the three dotted red lines.

4.4 Final C1 to T1 Phantom

4.4.1 Building the Phantom

The printing of the cervical vertebrae in nylon resulted in a very high quality structure, as illustrated in **Fig. 4.17 a)**. Contrary to in the previous vertebrae in Standard White Resin, the nylon intervertebral space is clear of any irregularity due to the SLS printing process, as shown in **Fig. 4.17 b)**. However, as discussed in **Section 5.2.1**, the printing software still includes some unwanted connection points between the vertebrae to ensure the structural integrity and interconnection between different parts, as shown in **Fig. 4.17 c)**.

Pictures of the shell's building process can be found in **Fig. 4.18**. The shell was successfully covered with fiberglass and epoxy, so that it became watertight. The coating is nevertheless imperfect. Epoxy streaks have run down the sides of the phantom, creating bumps, while air bubbles remain in some areas under the fiberglass. The plastic bag on which was put the shell to dry has also partially stuck to the phantom.

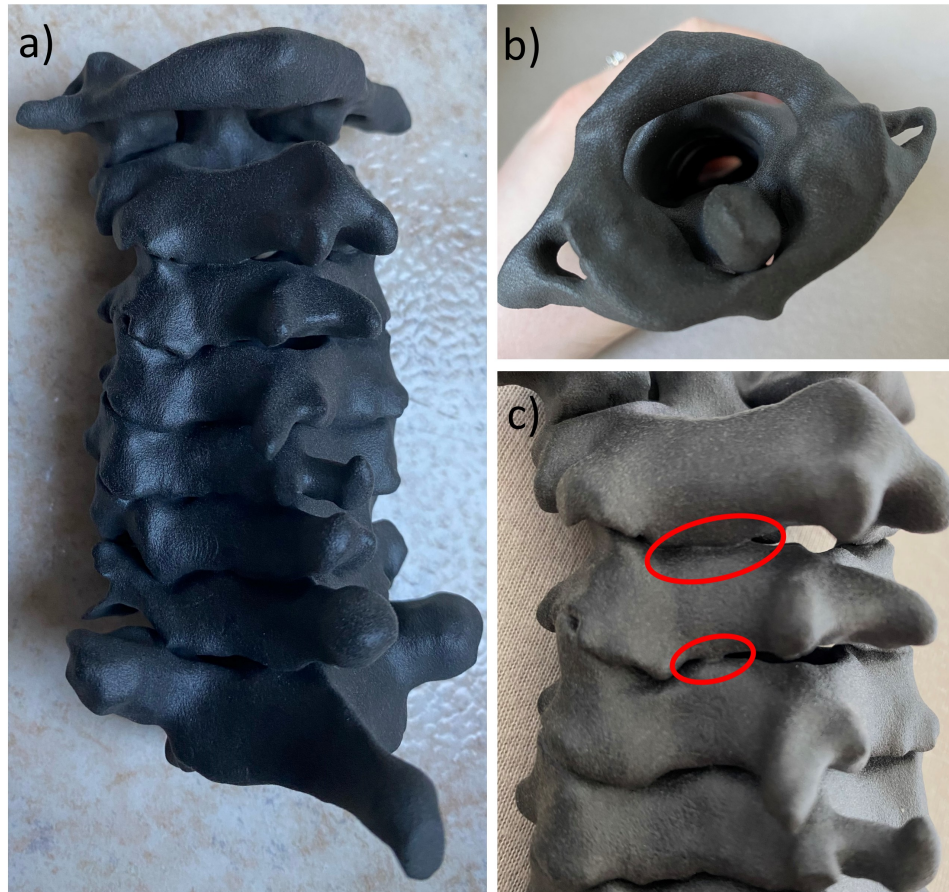


Figure 4.17: a) Final nylon printed vertebrae. In b), one can see the good quality of the printing. Contrary to the previous resin vertebrae, SLS printing allows having no support to remove, and thus no additional artifacts as observed in **Fig. 4.5**. However, to guarantee the solidity of the structure and that the vertebrae were well attached to each other, some intervertebral attachment points were added by the printer (c). Two of them are shown in red.

4.4.2 Field Map Analysis

4.4.2.1 Susceptibility Difference

A high correlation between the simulated and acquired data restricted to the spinal canal between C3 and C5/6 was shown by the linear regression illustrated in **Fig. 4.19**, with a p-value $p < 0.001$. The linear relationship between the two FMs is $y = 25.0 \cdot x + 3.0$, and has a high variability with $R^2 = 0.21$. By restricting the area of interest of the regression to other parts of the vertebral structure, the slope was found to have values between 20 and 40 Hz/ppm, meaning a susceptibility difference of $\Delta\chi \in [0.07, 0.13]$ ppm between the vertebrae and the solution. The large error dispersion is confirmed by the histogram in **Fig. 4.19 c**).

The simulated field map rescaled from ppm to Hz using the slope of the linear regression, restricted to the C1 to C3 vertebrae and to the C3 to C5 vertebrae, is presented next to the acquired field map after background correction in **Fig. 4.20**. Qualitatively similar patterns can be observed between the simulation and the measurement for both the selected regions of interest. The field in front of each spinal process is lower, while it increases between the vertebrae, similarly as what was already observed in the study of the C3 to C5 phantoms in **Fig. 4.8** and **4.10**. These intense periodic drop-outs are observed on both the anterior and posterior sides of the canal, although they are more pronounced on the posterior side.

To observe the same intensity of artifacts in the simulated FM and in the acquired one, the color scale



Figure 4.18: Pictures of the final shell of the phantom. It is presented before (a) and after (b,c,d,e,f) the epoxy and fiberglass application.

of the simulation had to be restricted to extreme values about 2 times smaller than the acquired FM scale, suggesting that the value of susceptibility difference obtained by simulation is underestimated.

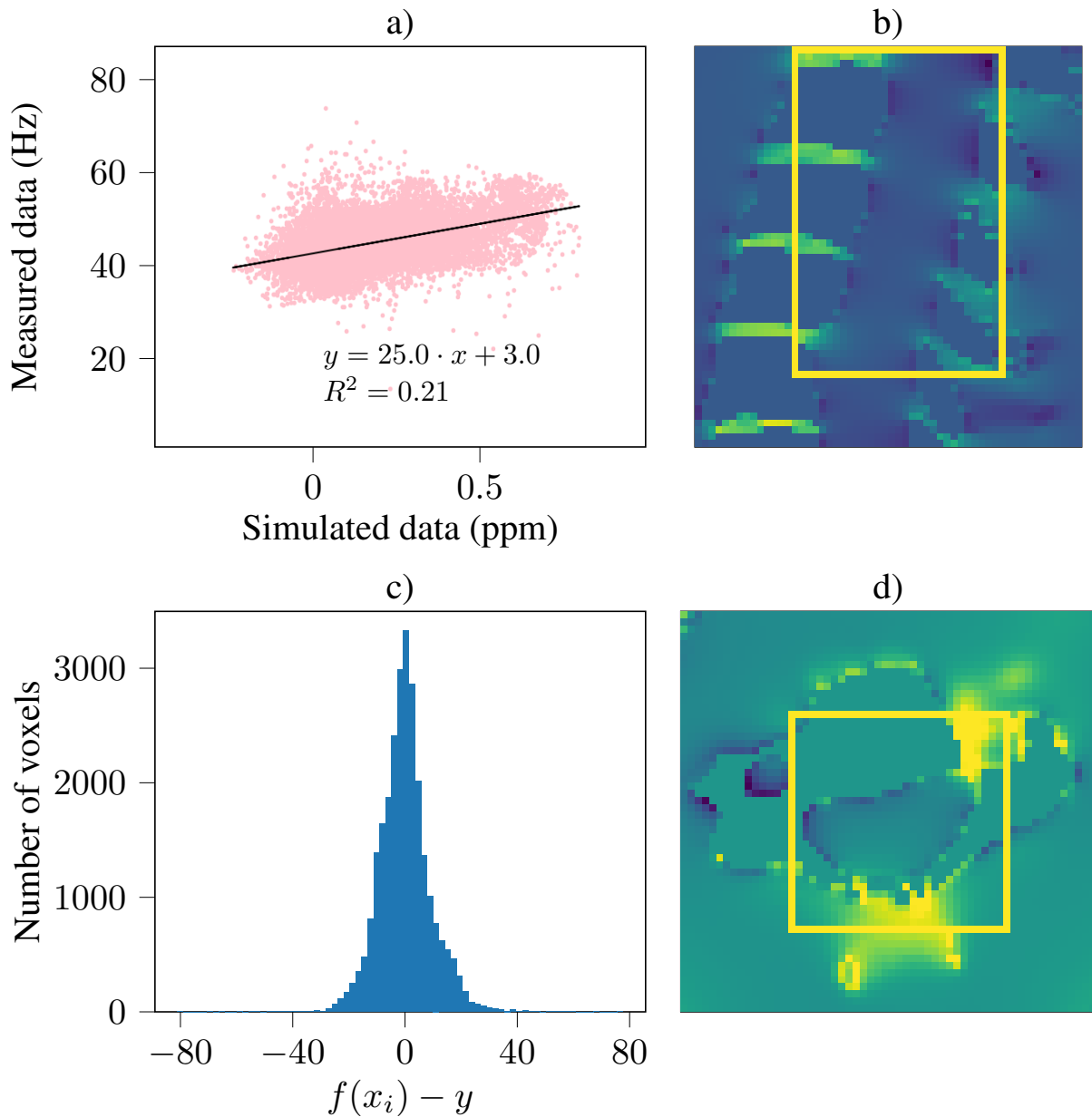


Figure 4.19: Linear regression between the experimental and simulated field maps (a). The regression was run on the voxels inside the 3D area illustrated by the yellow frame in the sagittal and transversal slices b) and d). c) is the histogram of the error $f(x_i) - y$, with y the acquired value, and $f(x_i)$ the approximate linear value obtained from the simulation using the coefficients of the linear regression.

Even after background removal and correction by linear gradients, the measured data still exhibits strong background inhomogeneities, making it difficult to observe the periodic alternations of signal drop-outs within the canal. However, restricting the correction to these smaller regions of interest has yet allowed for an improvement in the visual quality of the images.

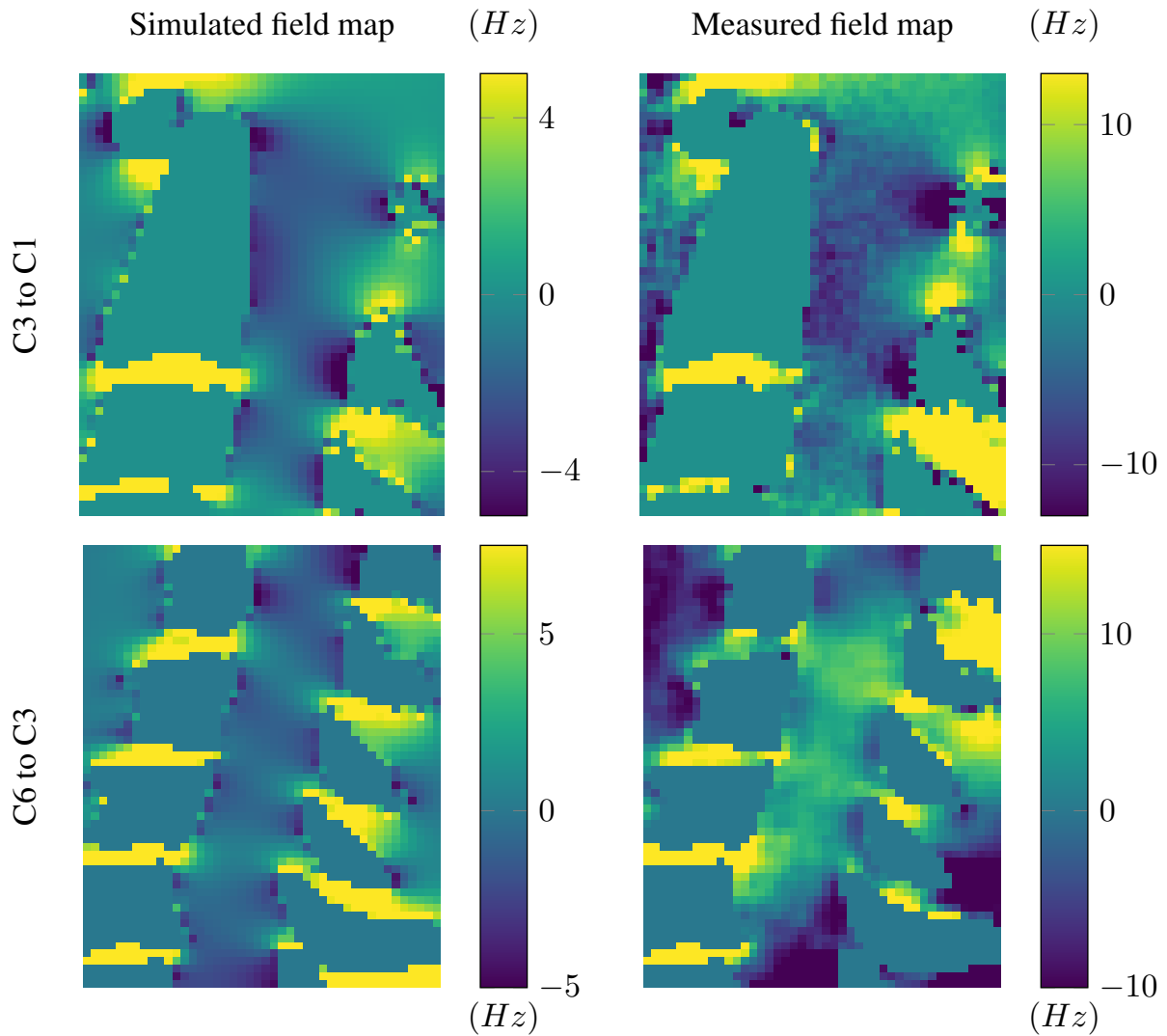


Figure 4.20: Simulated (left) and measured field maps, restricted to C3 to C1, and to C6 to C3. The simulated FM was computed in ppm by allowing a susceptibility value of 1 for the voxels inside the vertebrae, and 0 outside, and then rescaled to Hz using the slope of the linear regression. The values inside the vertebrae are masked.

4.4.2.2 Z-Gradients

To reduce the impact of the inhomogeneities in the background, the gradient of the field variations along the z-direction was computed and is shown in **Fig. 4.21**. If this method is inefficient to remove the systematic effects from the background field, it was nevertheless successful in removing the larger gradients of inhomogeneities in the background which were probably generated by the shell and the external air. Positive and negative alternations of the field gradient can indeed be observed in the spinal canal, with a huge variation around the intervertebral junctions, for both the simulated and measured data. These quick field variations are especially visible along the posterior side of the spinal canal, confirming the previous observation that the posterior side of the vertebrae generates stronger field variations than the anterior one.

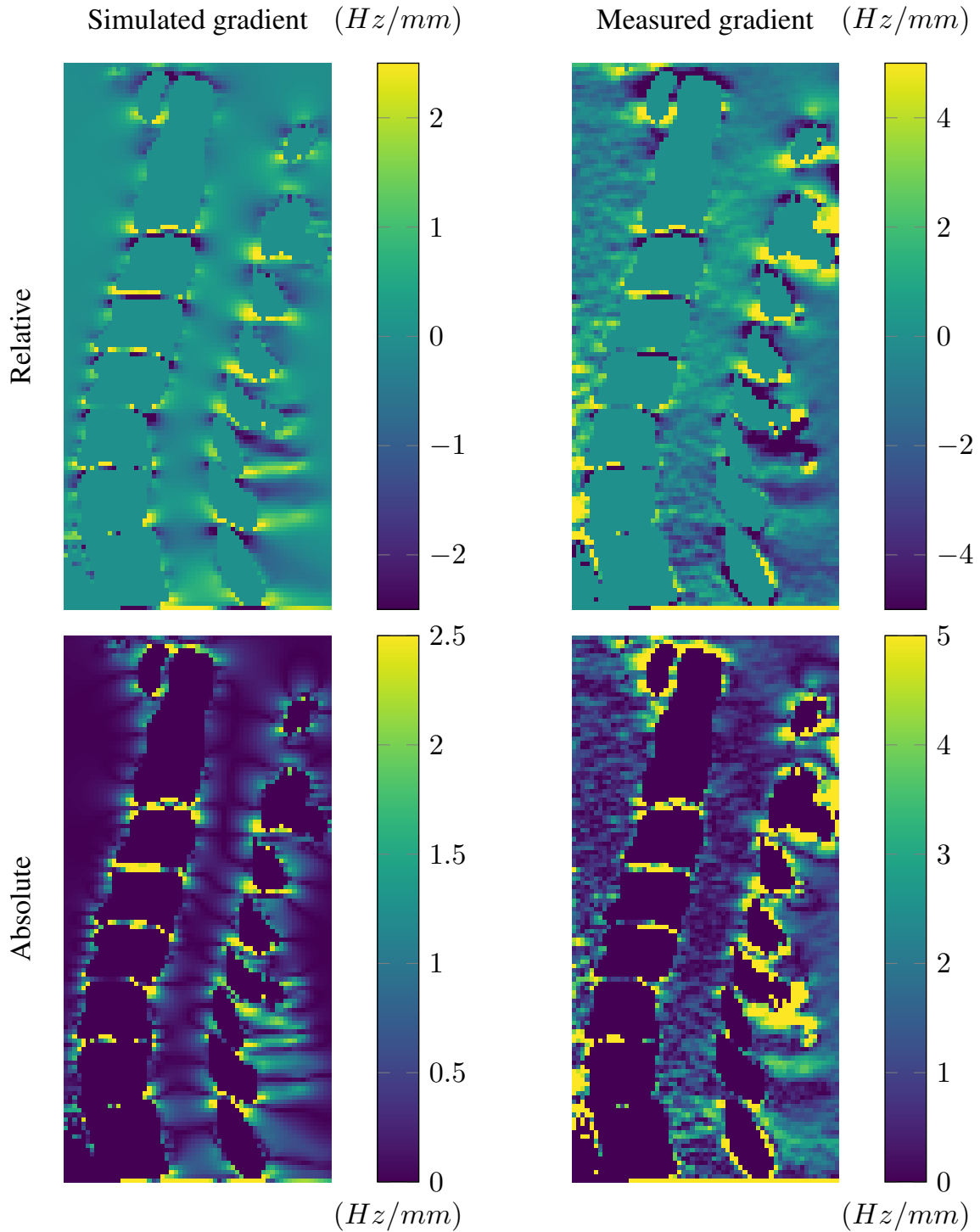


Figure 4.21: Comparison of local field gradients (upper part), and absolute values of the gradients (lower part) along the z-direction for both the simulated (left) and the measured (right) field maps of the final cervical phantom, from C1 to T1. The simulated gradient was previously rescaled from ppm to Hz using the slope of the linear regression.

4.4.2.3 Simulation of the Artifacts Generated by the Shell and the Air

In the two previous paragraphs, only the susceptibility difference between the vertebrae and the external solution was considered. However, it was a strong assumption, and rather inaccurate in this case where

the vertebrae are very close to the shell, which itself has a complex shape, and is surrounded by air. In this section, a three-color mask was therefore considered, where different values were assigned to the voxels inside the vertebrae, inside the solution, and outside the shell. Due to the huge background inhomogeneities, this mask, shown in **Fig 4.22 a)** could not be perfectly defined as properly as the two-color mask, parts of the solution, especially in the upper part, having a magnitude value lower than the external air. The complete shell could also not be simulated, as it was restricted by the acquisition's FOV.

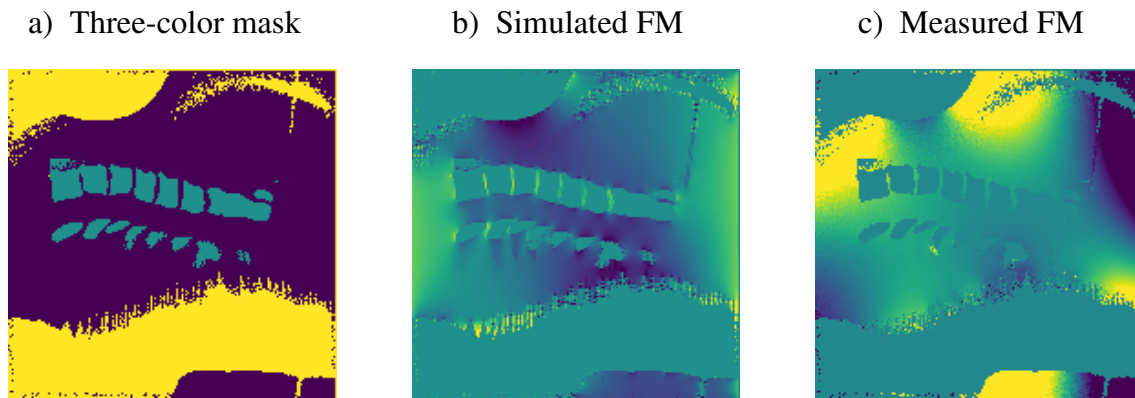


Figure 4.22: Three-color mask (a) of the magnitude of the acquired FM. Outside voxels have been assigned a value of zero, while $-\text{coeff}_{\text{air}} = -1$ was attributed to the voxels inside the vertebrae, and $-\text{coeff}_{\text{air}} - 1 = -2$ the voxels of the solution. The resulting simulated field map is shown in b). The acquired FM before correction is given in c) for comparison. In b) and c), values outside the shell, and inside the vertebrae are masked.

Although imperfect, this mask allowed the visualization of some of the large gradients generated in the background by both the shell and the external air (**Fig. 4.22 b)**). A strong field decrease (in blue) appeared in the neck region by considering the shell effect, thus masking parts of the susceptibility artifacts generated by the vertebrae in solution. Lower values of the field can also be observed at the same position in the uncorrected acquired FM (**Fig. 4.22 c)**). However, the measured data still exhibits much larger field variations, especially in the anterior and superior regions of the phantom, likely due to the shape of the head and thorax which were not fully accounted for in the simplified mask.

In the absence of exact knowledge on the susceptibility difference between the shell and air, and the solution, different values of $-\text{coeff}_{\text{air}}$ were tested, leading to similar patterns of field variations, but different scales. For visibility reasons, **Fig. 4.22** is presented for $-\text{coeff}_{\text{air}} = 1$.

4.4.3 Multi-Echo GRE Analysis

4.4.3.1 Visual Inspection of the Echoes

Fig. 4.23 a), b) and c) shows phantom multi-echo GRE images from three selected slices, respectively mid-C2, just above the C3/C4 intervertebral junction, and mid-C5. Their magnitude difference with the first echo at $\text{TE} = 4.75$ ms is plotted below the magnitude image for each echo. **Fig. 4.23 d)** gives the exact position of the three transversal slices, in a sagittal plot of the difference magnitude with the first echo. **Fig. 4.23 e) and f)** are in vivo representatives of a mid-C3 slice and an intervertebral (above C3/C4) slice, given for comparison.

The slice located in the middle of C2 and in the lower part of C1 (**Fig. 4.23 a)**), presents a strong signal drop-out along the posterior rim of the spinal canal, similarly to the in vivo slice located in an intervertebral region (**Fig. 4.23 e)**). The C2 and C1 vertebrae are positioned in the phantom very close to the neck. Thus, in addition, a strong signal decrease along the rim of the neck is also visible, following a curve almost superimposed on the one of the signal loss within the C2 vertebra.

The mid-vertebrae slice in **Fig. 4.23 b)** also suffers from a signal decrease along the spinal canal, both anteriorly and posteriorly, with a greater loss along the posterior side. This pattern resembles the in

vivo pattern (Fig. 4.23 e)).

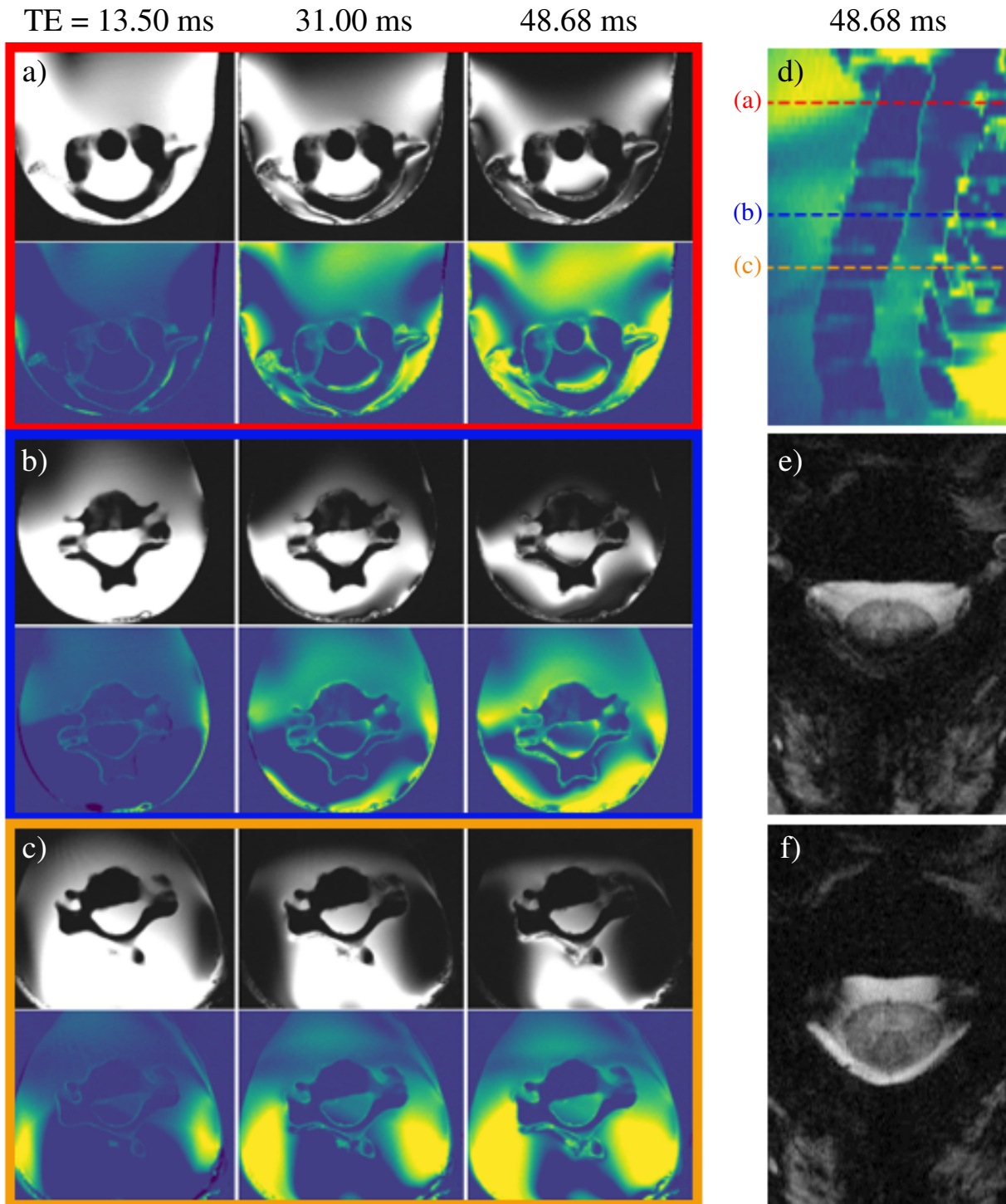


Figure 4.23: Representative transversal slices of the ME-GRE acquisition on the final phantom (a,b,c). The magnitude images are shown for three echo times, and the difference to the first echo, acquired at $TE_1 = 4.75$ ms, is shown below the magnitude image for each echo. The localization of the slices (mid-C2/low C1, upper C4 and mid-C5) is illustrated by the red dotted lines in the sagittal view in d). e) and f) are representative slices from an in vivo GRE acquisition, respectively located above an intervertebral junction (C3/C4) and mid-vertebra (mid-C3) showing different patterns of signal drop-outs.

Only a slight signal loss can be observed in the mid-C5 slice's anterior right corner, far from the significant signal loss observed in vivo in (Fig. 4.23 f) in both anterior corners. In both in vivo and phantom cases, no loss is observed anteriorly.

4.4.3.2 T_2^* -Values

The T_2^* of the solution was computed by exponential fit between the echoes, as it was done for the previous phantoms. However, T_2^* values from 8 to 100 ms can be found depending on the voxel, as Fig. 4.24 shows. The relaxation values seem to follow a gradient of variation in each transversal slice, with lower values around the posterior and anterior parts of the shell, and higher values closer to the vertebrae. The mean and standard deviation of the transversal relaxation time of the slice shown in the T_2^* -map have been computed between the voxels with an associated coefficient of determination $R^2 > R_{\min}^2$ and are given in Table. 4.6.

R_{\min}^2	T_2^* (ms)	Std (ms)
0.85	29	28
0.90	27	26
0.95	25	23

Table 4.6: Mean T_2^* -value on one slice, and its associated standard deviation Std. The values were computed for $R^2 > R_{\min}^2$

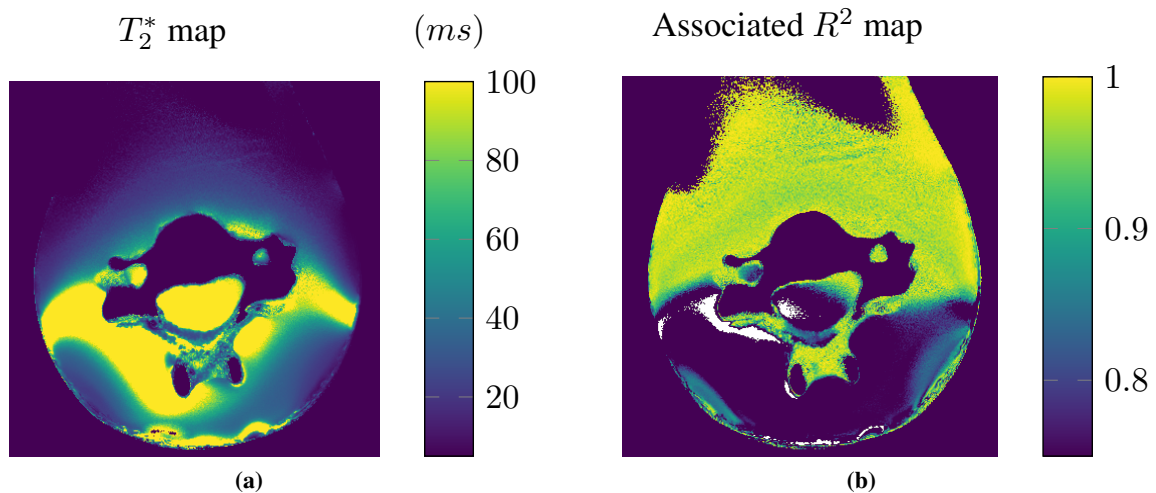


Figure 4.24: (a) Map of the T_2^* values in the external solution of the final phantom, for one slice, and their associated R^2 (b). White voxels in the R^2 -map are voxels that generated an error in the computation of the T_2^* -value.

Discussion

In this master's thesis, step by step, a complete 3D printed phantom of the cervical vertebrae was built, realistically reproducing the static B_0 field inhomogeneities observed in vivo. Different printing materials were first tested, and compared by their cost, availability, susceptibility performance and resolution, leading to the selection of Standard White Resin and nylon. A first phantom of C3-to-C5 vertebrae in a water and salt solution, printed in Standard White Resin, was constructed, already visually reproducing the periodic drop-outs observed in vivo. Different components such as sugar, soap or mouthwash were then proposed to tune the properties of the solution or reduce the air bubbles, and their effects in solution on the relaxation time T_2^* and on the susceptibility were measured. Sugar in particular was shown to have a diamagnetic effect on the solution, drastically reducing its susceptibility, in addition to its T_2^* . A second phantom of C3 to C5 vertebrae in resin, in a solution tuned with sugar, salt and mouthwash, allowed to recover the in vivo susceptibility artifacts, this time matching the expected difference in bone/tissue susceptibility. The relaxation time of the solution, however, was lower than expected. Finally, a final phantom was printed in nylon, and placed inside a head to thorax anthropomorphic shell, in a solution of salt, sugar and soap in water. This phantom was solidified and made watertight by applying a layer of epoxy and fiberglass. It proved to efficiently reproduce the artifacts generated in vivo around the vertebrae, but the shell also generated strong gradient inhomogeneities, increasing the variability of the computed susceptibility difference and T_2^* values.

5.1 Phantom Design

5.1.1 Vertebrae Design

Both the C3-to-C5 and the C1-to-T1 vertebrae were extracted from public CT datasets to STL files by segmentation using the software 3D Slicer (Kikinis et al., 2012; Fedorov et al., 2012).

Given that the aim of the phantom was to represent a typical and disease-free human, the selection of an appropriate dataset was crucial. Specifically, the dataset had to come from a healthy patient without scoliosis, fractures, or abnormal spinal curvature. Moreover, the quality of the dataset, which had to present a good resolution on the whole vertebrae of interest, in order to be able to segment them precisely, was also a key selection criterion. To meet this criterion, we opted to use CT imaging, which is the reference imaging modality for bone analysis. This type of imaging is the most commonly used in literature for the design of anatomical parts for 3D printing, such as in the Clifton et al. (2019) cervical phantom. However, a major limitation of CT imaging is its high level of ionizing radiation exposure. As a result, it is uncommon for healthy individuals to undergo this type of imaging, making it challenging to find public databases with images of healthy spinal columns. The anonymization to which the public data are subjected also led to a loss of information on the healthiness of the different CT imaged patients. To ensure the suitability of the datasets, each set of images then had to be evaluated individually to

determine their quality and the health of the subject. This assessment involved a manual inspection of multiple files, until finding one that minimized the problems, taking a considerable amount of time, and requiring extensive knowledge in anatomy. This issue could have been limited by using images with known pathologies and annotated by St. Olav hospital, but it could unfortunately not be possible due to confidentiality concerns. The printed C3-to-C5 vertebrae were chosen from the Verse dataset (Liebl et al., 2021; Löffler et al., 2020; Sekuboyina et al., 2021) for their relatively good imaging quality, their absence of fracture, and the good curvature of the spine between C3 and C5. However, their use could not be extended to the segmentation of the C1 to T1 vertebrae because of loss of image quality at the level of the last cervical vertebrae, and because of poor curvature of the lower part of the cervical spine (an effect that was negligible for the analysis of only three vertebrae). The vertebrae C1 to T1 were chosen from the dataset and online tutorial of Dr. Mike (2016). Unfortunately, they present a slight scoliosis, but no better spine could be found during our research. The latter also had the advantage of belonging to an acquisition with a large FOV, which could have allowed the export of the associated anthropomorphic human shell, as discussed in **Section 5.1.2**.

The initial stage of the vertebrae segmentation was executed automatically by the software, based on a predefined threshold. Nevertheless, this process is not flawless, mainly because of the intricate nature of the 3D spine and of the inhomogeneity of the bone marrow. Although this initial step did manage to select most of the vertebral bones, it also included fragments of ribs, intervertebral disks, and ligaments. The software also often had difficulty identifying the correct connection points between adjacent vertebrae, and added non-existent points in between the vertebrae. In addition, the software defined holes inside the vertebrae. The segmentation therefore required a lot of manual work to correct for these errors. As unfortunately, some remaining holes were detected inside the printed C3-to-C5 vertebrae during the analysis of the acquired data, extra attention was then paid to the design of the final cervical vertebrae. A small imperfection in the posterior, inside part of the C3 vertebrae printed in resin was also identified when imaging the vertebrae, as shown in the appendix in **Fig. 7.1**. This hole allowed sugar to build up in one area, damaging the FM with a large field drop, as it was observed in **Fig. 4.10**.

It is also interesting to note that 3D Slicer is a very powerful software, but it also requires high computational power to segment large volumes of data. A good computer with a powerful graphics card was useful to reduce segmentation times, thus allowing a more precise segmentation.

To reduce the intervertebral undesired connection artifacts, each vertebra was segmented alone, instead of all together, in both segmentations. Just before the export to STL format, an additional combination of the vertebrae by the software was carried out. This technique was very efficient for the design of the C3-to-C5 vertebrae, removing all the unwanted in between artifacts. However, as some of the vertebrae of the second template had a very tiny intervertebral space, but no defined contact points, the software forced to add badly positioned connecting points. The C1-to-T1 vertebrae were therefore exported separately to an online STL file merger to remove these points. However, some of them had to be added back for the actual 3D printing of the vertebrae to guarantee the solidity of the structure, as discussed in **Section 5.2**.

5.1.2 Shell Design

The human-shaped shell was designed on Solidworks (Dassault Systèmes Solidworks Corporation, 2022) based on the Spinoza phantom by Lopez-Rioz and Cohen-Adad (2023), before being exported to STL format to be 3D printed.

The final phantom shell had many criteria to fulfill. The first priority was to create an anthropomorphic shape that could accurately reflect the effect of susceptibility artifacts observed inside the human body. Due to the complex geometry of the human body, differences in susceptibility between external air and internal tissues can cause background gradients during acquisition, which is particularly challenging for the imaging of the cervical spine, which is closely surrounded by the neck. In addition, the shell had to be MRI-compatible, cost-effective, and watertight to enable the containment of various chemicals and

liquids, as we decided not to use a gel phantom. Finally, the shell had to be empty and to feature an opening system that would allow for the movement and replacement of vertebrae, as well as the change of solution to ensure the flexibility of the phantom's operation. Various options for purchasing possible phantoms were considered, such as a combing head or a pool rescue mannequin, but these options, which were quite expensive, could not guarantee the required criteria. Most of the available structures of this type do not provide information about their composition and do not guarantee the absence of metallic substances. Additionally, the space inside them is usually limited, and the few opening and closing systems available are not suitable for our needs. A manually fabricated, very simple phantom could have been a backup solution, made by combining a jerrycan and one of the plastic spheres used as a first container, roughly modeling a thorax and head shape. However, its strength, water-tightness, and anthropomorphic character would have been greatly compromised. Considering the required criteria, the use of a 3D printed shell was finally decided. Its printing model was first planned to be extracted from a CT file, similarly to the vertebrae. In that way, it could be directly adapted to the printed vertebrae, in size and position. Such a shell was segmented using 3D Slicer and exported as an STL file. However, further modifications were required, such as the addition of a screw cap system, and the extracted shell was therefore imported into Solidworks, a popular and powerful engineering CAD software. As the segmentation required an incredibly complicated number of nodes and points, it could not be modified in the software without crashing it. The shell then had to be fully designed in CAD, based on the CAD Spinoza phantom of Lopez-Rioz and Cohen-Adad (2023). Having this CAD as a starting point was of great utility, as the anthropomorphic representation was already there, and only specific modifications such as closing parts of their phantom, adding a longer thoracic part with a hole and designing the screwing system were left, reducing considerably the amount of work.

The choice not to design a complete hanging system for the vertebrae directly on the CAD model was made deliberately to keep freedom in further modifications of the size of the shell, solution or vertebrae. Only a vertical bar was added under the nose, as a reference position for the C1 vertebra. Five plastic hooks, commonly sold as concrete hooks, were instead glued inside the shell as a final preparation step, after the printing and coating processes commented in the later **Sections 5.2** and **5.4**. This decision proved to be very beneficial, as the shell ultimately had to be printed in a smaller size, as explained in **Section 5.2**, which would have changed the positioning of the attachment systems, as the vertebrae were not reduced in size. Furthermore, this system was contingent on whether the vertebrae would submerge or float, which was dependent on the material of the 3D printed vertebrae.

The Spinoza phantom (Lopez-Rioz and Cohen-Adad, 2023) was limited to a man's head and shoulders. As we were interested in the study of the cervical vertebrae, from C1 to T1, we decided to extend this model to the upper thorax, to limit the impact of the sharp angles of the lower part of the shell on the field map of the vertebrae. Human body is not composed of sharp angles, but rather has a more rounded shape, each of its extremities fitting smoothly into the next. Thus, attention was paid in the design of the template to smooth the transition between the parts of the model, and fillets have been added to all the edges and corners of the CAD.

5.2 3D Printing Process

3D printing was used all along this master's thesis, to print successively material samples, vertebrae, and a human shell. The samples and vertebrae were all printed in one piece by the printing center associated with St Olav's hospital, while the shell was ordered from the online printing company Protototal (PROTOTAL AS), and printed as a jigsaw puzzle before being assembled back and glued by the company.

5.2.1 Printing of the Vertebrae

The C3-to-C5 vertebrae were first printed horizontally inside the printer. Indeed, this orientation minimized the printing time and therefore the costs. However, as can be seen in **Fig. 4.5 a**), small irregularities

due to the printing support, necessary in SLA- printers, couldn't be removed inside the spinal cord canal. They would have needed to be removed manually with a knife or with sanding, but the complex geometry limited it. In a second time, the C3-to-C5 vertebrae were therefore printed upright, to improve the outcome by reorienting the models during printing, and then reduce the support in hard-to-reach places. One can see in **Fig. 4.5 b)** that this reorientation effectively reduced the asperities in the intervertebral canal, which is the region of interest.

The nylon 3D printing resulted in very good quality vertebrae, as **Fig. 4.17 a)** shows. The SLS printing process, a type of powder bed fusion, is based on a high-powered laser sintering layer by layer the powder (here nylon) to gradually form the desired structure, and therefore doesn't need a support structure, on the contrary to SLA processes. This property is reflected in the high quality of these vertebrae, where, as shown in **Fig. 4.17 b)**, no artifacts due to improper removal of a support can be observed, whereas the C3 to C5 vertebrae of the first two phantoms suffered from this problem, especially when the printing orientation was badly chosen. The segmented vertebrae not being all physically in contact, or very little, the printer and his software unfortunately had to add points of connection between the vertebrae. Although most of the imperfections were located on the lateral sides of the vertebrae, which did not pose a problem for our purposes, some were situated at the level of the intervertebral discs when the vertebrae were in close proximity. Ideally, we would have preferred to maintain the spinal canal free of such imperfections. For cost, time, and structural solidity considerations during the initial testing phase, we decided not to reprint the vertebrae with reduced adhesion points.

5.2.2 Printing of the Shell

The shell template represents in scale one a large, tall man's head to thorax. Inspired from the indications of the Spinoza phantom (Lopez-Rioz and Cohen-Adad, 2023), it was first planned to be printed in PLA, the most common and cheapest printing material available in the market, as the shell did not require high resolution printing. This shell, approximately 529 mm long, was too big for the printers from the printing center of St. Olav's hospital, and the decision to order it from an online company was taken, despite the additional costs. A first company, Hubs (HUBS), was selected for their offer of large printers, up to 500 mm long, and of free online price simulations. However, even the industrial PLA printers available online could not print such a big piece, so the decision was made to isometrically reduce the phantom and analyze the relationship between size reduction and price. The price was found to be linear to the volume to print, so reducing the length along each dimension would quickly decrease the price. Ultimately, the decision was made to print the phantom at 80% of its original size, to ensure that it would still realistically represent a smaller human, given that the original phantom was modeled after a large man.

The Fused Deposition Modeling (FDM) is a printing process that uses thermoplastic polymer filaments that are melted and deposited layer by layer to form a selected mesh and progressively build a 3D object (HUBS). This process requires as an entry parameter a choice of the infill percentage, the percentage of the building matrix that will be filled with mater. The infill percentage and layer thickness affect the final strength and weight of the printed object, as well as the time and cost required for printing. In our case, the shell needed to be filled to 100% to restrain the impact of air susceptibility on the observed field artifacts. However, such a complete infilling is not reachable in FDM printing without risking printing errors. The decision to print the shell in nylon instead of PLA was then taken, as the SLS technology can result in a completely filled shell, even if it is more expensive.

Nylon is more expensive than PLA. However, no printing support is needed to print nylon through the SLS process. The powder that is not used can be reused, and all the printer's volume can be used to print different parts of the structure of interest, allowing a reduction in both material loss and printing time. Prototal AS (PROTOTAL AS), another company providing custom support, was contacted to divide the shell into several pieces like a jigsaw puzzle, print them and reassembled them with glue. This process probably has weakened the shell structure, but allowed the saving of more than 10000 NOK, and

a quicker receipt of the shell. During the epoxy coating of the printed shell, commented in **Section 5.4**, extra attention was paid to the proper recovery of the joints where the different pieces were assembled.

A bar was designed below the nose to provide a reference point for the superior anterior part of the C1 vertebra and help with its positioning within the shell. This bar was useful to position the superior part of the vertebrae, as it was positioned vertically to the nose. However, due to the reduction in size of the shell to 80% of its original size, the non-reduced vertebrae could not fit anymore under the marker. If the shell had to be reprinted, this bar should be resized accordingly to fit the size of the vertebrae.

5.3 Selection of Materials for Printing the Vertebrae

Five printing materials were tested in this project. After careful consideration, Standard White Resin was chosen for the C3-to-C5 phantom and nylon for the C1-to-T1 phantom.

We had the opportunity in this thesis to test the susceptibility effect of five different materials from four different processes (FDM, SLA, SLS and material Jet), but several other printing materials and processes exist today. The selected studied materials were conditioned by the ones available in the printing center and by their cost. However, this study could easily be extended to the testing of new materials that could maybe better fit the spine properties.

Initially, nylon was not available as a printing material, so Standard White Resin was chosen to print the C3-to-C5 vertebrae, as it was less expensive than M3 Crystal, but offered better quality and resolution than PLA or Flexible 80A Resin. The susceptibility difference with an external solution of salt and water was, by chance, similar in absolute value to the one between bones and tissues, but with opposite signs. That allowed the visualization of artifacts visually similar to those observed in vivo, regardless of the sign. This sign difference could have been neglected, as a sign can easily be inverted during the post-processing process, if this phantom did not have as a final aim the extension to the modelization of the B_0 inhomogeneities not only static, but also dynamic. Indeed, in the further developments of this project, air volumes will have to be taken into account, and a sign modification will not be doable anymore, as three different susceptibilities will be involved. As explained in **Section 5.5**, sugar was finally used as a contrast agent to decrease the susceptibility and the T_2^* of the solution, allowing the signs of the field variations to be inverted. However, obtaining a susceptibility difference with Standard White Resin vertebrae that was high enough to match in vivo acquisitions resulted in an excessive reduction of T_2^* . Nylon had a susceptibility difference with water much closer to the in vivo difference than Standard White Resin. A smaller amount of sugar could then be used to match the targeted susceptibility difference, thus reducing the transversal relaxation time to a lower extent, but, this time, not enough to match the in vivo properties. It was nevertheless preferred to Standard White Resin in the final phantom for two reasons. Firstly, it is easier to reduce the T_2^* of the solution than to increase it, as we have seen in **Section 4.2.2** with **Table. 4.5**. Another component, having similar properties to soap for example, could be added to further decrease the T_2^* without affecting the solution's susceptibility. In addition, the shell had to be printed in nylon, due to the considerations described in **Section 5.2.2**. If the final vertebrae had been printed in Standard White Resin, the external solution would have had to be of higher sugar concentration, thus increasing the shell artifacts to higher artifacts than the one produced by the vertebrae. By printing the vertebrae in nylon, we limited the amount of sugar used, and therefore the shell's artifacts.

5.4 Shell Preparation

To ensure the solidity and the water-tightness of the printed human shell, it was covered with roving fiberglass and epoxy. One layer of epoxy was also applied inside to smooth the gluing imperfections.

A first attempt of epoxy and fiberglass coating was done on the spherical plastic sphere used for the C3-to-C5 phantoms. The sphere was successfully covered with the two solidifying materials. However,

we chose to use small pieces of fiberglass measuring approximately $15 \times 15 \text{ cm}^2$, to prevent folding imperfections on the spherical structure. This approach proved to be challenging as the fibers at the ends of each fiberglass piece were more difficult to glue, creating protrusions at each overlap, and combining two negative effects. First, the outer surface was no longer homogeneous, thus presenting more risks of creating point artifacts on the MRI images. In addition, these unglued fibers were sharp, creating a risk of injury, and a risk of tearing the sealing system. Sanding the fiberglass, once dry, helped to polish the phantom and therefore decrease the number of imperfections, but was insufficient to remove all of them, especially on the top edges of the sphere. Indeed, one of the reusable IKEA plastic lids that we used to close the device was torn by one of these "spikes" of fiberglass. Air bubbles in the epoxy layer could also be remarked. No strong effect of the coating could be observed in the acquired data on the last C3-to-C5 phantom. Based on these useful observations, extra attention was paid to avoid air bubble formation while making the final phantom. Moreover, larger fiberglass pieces were used to reduce the number of joining sections in the phantom.

This first experiment with fiberglass and epoxy also allowed us to realize that the epoxy we used was very liquid, and flowed by gravity from the upper to the lower parts of the inside of the epoxide structure. For the final phantom, we tried to get a less liquid epoxy by waiting for it to dry a bit before applying it. Thanks to this technique, some epoxy could remain on the upper part of the final phantom. However, a large portion of the solution still leaked and accumulated in the posterior side of the shell. Only one brand of epoxy was tested, and the proportions recommended by the manufacturer were followed in the preparation of the epoxy solution. Other brands or dosages could, however, be evaluated to minimize flow concerns. Streaks of liquid epoxy also ran down the outside of the phantom, causing epoxy bubbles that could not be removed, even by sanding.

The decision to request the online company that we ordered the shell from to glue the upper cap onto the head was made in order to ensure the structural integrity and water-tightness of the head, more fragile than the thorax. This opening, designed for the Spinoza phantom (Lopez-Rioz and Cohen-Adad, 2023), could nevertheless have been useful to ensure a good epoxy application process of the top part of the shell. Indeed, this part was difficult to reach, especially because we decreased the size of the phantom, then reducing the width of the neck.

Plastic bags were used as protective support on which the shell was put during the drying processes. They have, however, faded, and have partially stuck to the phantom, probably due to their poor quality, even though they were, of course, placed on the dry side of the structure. If adding additional colors to the shell is not really a problem, even a hard sanding could not remove all these extra pieces bonded to the phantom, thus preventing a smoother surface. Images of the shell can be found in **Fig. 4.18**.

5.5 Tuning the Solution

Several solutions containing soap, sugar, salt and mouthwash were studied to determine how to dope the water solution to match the *in vivo* properties, as described in **Section 3.2**. Finally, a solution of $C = 75 \text{ g/L}$ sugar, salt and soap was chosen to simulate the tissues in the cervical phantom.

The choice of the components to study was inspired from the components used in the Spinoza phantom (Lopez-Rioz and Cohen-Adad, 2023), and of the recipe from Duan et al. (2014) (AMRI, 2016), who propose to use NaCl as a conductivity modifier, sucrose and agar or agar-agar as relaxation times reducers, and respectively as permittivity controllers and gel agents. In addition, they both added a conservative agent, either benzoic acid or mouthwash. Based on this, we decided to investigate the properties of sugar, salt, and mouthwash with and without alcohol. Soap was added during the first phantom acquisition due to the formation of air bubbles around the vertebrae in solution, perturbing the field in the spinal canal. It was found out not to modify the susceptibility very strongly, but instead reducing the T_2^* of the solution.

Sugar was proven to efficiently linearly lower the susceptibility value of water. This discovery was very beneficial, as we couldn't find another non-toxic, soluble contrast agent with a diamagnetic effect.

In addition, it has been demonstrated to shorten the T_2^* time.

Higher T_2^* values were found during the study of the solutions effects than during the vertebral phantom's acquisitions. This, although quite surprising, could come from various reasons. First, the analysis of the solutions containing the mouthwashes suffered from a high variability due to relaxation time values much higher than the chosen ME-GRE TEs. Another reason could possibly be explained by the T_2^* map in **Fig. 4.15 a)**, where flowing patterns can be observed in the higher part of the image, suggesting a poor mixing of the components. This could maybe come from chemical interactions reducing the miscibility between sugar and mouthwash, or simply from a poor manual mixing of the solution during its preparation. Regarding the efforts and time put in the mix of the components, a poor miscibility of mouthwash in the solution seems more probable. To limit this effect by restringing the number of components, mouthwash was not added to the final solution.

The composition of the final solution is a compromise between susceptibility difference, T_2^* , bubble removing and choice of material. As explained in **Section 5.3**, nylon was chosen as the final vertebrae printing material. A sugar amount insufficient to reduce the T_2^* enough, but correctly matching the susceptibility difference bones/tissues was preferred to a more sugary solution that would better match the T_2^* , but increase the susceptibility difference, as the main goal of this thesis was to reproduce the B_0 susceptibility artifacts. In addition, another component such as soap could possibly be added to modify the transversal relaxation time without modifying the susceptibility difference. Soap could have been one of those relaxing agents, but the decision to limit its use was taken, as we feared that it could produce the same artifacts as the mouthwash. However, the analysis of the phantom finally showed unexpected results, with both a lower T_2^* and a lower susceptibility difference than predicted. This could be due to the possibility that the shell was not completely cleaned inside after the epoxy treatment, leading to some molecules dissolving in the solution.

5.6 Pre-Acquisition Preparations and Phantoms Set-ups

Practical issues had to be overcome in the preparation and set-up of the phantoms and experiments.

Hanging the material samples, simple smooth spheres of 1 cm diameter, inside the plastic container, was far from easy. A thread had to be precisely tied around the material to be able to hang it, while minimizing the number of turns made to limit the effects of the thread on the susceptibility. The vertebrae were easier to hang, because a thread could be passed through the side holes of each one. On the other hand, care had to be taken to ensure that the vertebral column was aligned with the B_0 field, horizontal and not inclined. This, combined with the necessity of moving the phantom to the scanner room, caused several acquisitions to be interrupted by intermediate repositioning steps after running the localizer, which sometimes led to considerable waste of time and to imperfect positioning of the vertebrae within the phantoms. The problem of the variable flotation of the tested structures should also be mentioned. Indeed, if nylon always floats, Standard White Resin sinks in water, but floats when enough sugar is added. When the C3-to-C5 vertebrae were floating, a rubber had to be attached to the vertebrae and immersed in the bottom of the solution. The plastic tubes used to test the different solutions in **Section 3.2** also float. They thus had to be inserted inside a plastic film partially stuck to the edges of the container. This process was, however, quite laborious, as the verticality of the samples was complicated to ensure, while the film prevented the water from spreading evenly around the samples, hindering the study of their susceptibility difference with the solution. Finally, the T1 vertebra broke just before the last phantom acquisition. Luckily, it could be rapidly glued back to the cervical vertebrae, and didn't seem to have an effect on the generated field inhomogeneities.

The final cervical phantom, reduced to 80% of its original size, had quite a small opening, further complicating the task of correctly positioning the vertebrae inside the shell. In the last acquisition, even though we tried several times to position the vertebrae correctly, they always moved to an unrealistic position, as the lower vertebrae came up too much, and moved away from the back of the phantom. This

bad positioning can be seen in both the mask and the FM of **Fig. 4.22**. In further acquisitions on this phantom, a more practical and more precise way to hang the vertebrae will have to be organized.

5.7 Analysis of the Data

5.7.1 Field Maps

Field maps of both the tested materials samples, the tested solutions and the phantoms were acquired, and linearly compared to a simulation run on a magnitude-based extracted mask of the component of interest. The slope of this regression was then used to determine the susceptibility difference between the component and the external solution.

5.7.1.1 Simulation of the Artifacts

In most cases of this thesis, the shell containing the solution and the component to study was neglected in the simulation, allowing a good visualization of the spatial field variations generated by the object only, inside the solution. This method was a good approximation when the container was far from the studied component, or generated few artifacts, as it was the case in the study of small spherical samples with a diameter of 1 cm. It also worked reasonably well in the study of the three C3 to C5 vertebrae because the background generated by the container, which had a simple spherical shape, could be easily removed in the post-processing by using a reference field map. For the last phantom, the use of this simple two-color mask allowed for an easy simulation of the vertebral field, but it was a highly simplistic approximation that could not be very accurate due to the proximity of the vertebrae to the edges of the phantom. Additionally, the complex shape of the phantom resulted in the generation of more artifacts, more difficult to correct by a simple reference background removal.

In a second time, a three-color mask of the final phantom was defined, still based on the magnitude information of the acquisition. By simulating on this mask, one could immediately remark the huge impact of the shell on the field variations, masking parts of the artifacts generated by the vertebrae. The mask, nonetheless, exhibited significant imperfections since it was solely generated from the magnitude data obtained from the field map acquisition, which had a reduced field of view and hence failed to consider the entire phantom. In addition, due to the presence of large gradients likely caused by the shell and air, it was not feasible to generate a three-color mask simply by setting magnitude thresholds, and instead multiple steps were required to clean the mask. Despite these efforts, the resulting mask was still incomplete and imprecise. In a later stage of this project, a more complete and precise three-color mask could be generated by importing the STL templates of the shell and vertebrae to Matlab. Different values of susceptibility difference between the solution and the external air and shell were tested, as the susceptibility of the shell is unknown, and as the aim was only to obtain a qualitative understanding of the field variations induced by a system taking into account the shell, without attempting to extract numerical values. Regardless of the coefficient used, obtaining precise measurements would have been impossible due to the mask's intrinsic imprecision.

5.7.1.2 Background Correction

Different methods of background correction were tested to remove the unwanted field variations, as **Fig. 4.6** illustrates. For all the acquisitions using the plastic sphere as a container, subtracting a background reference appeared to be the best and simplest way to remove most of the unwanted artifacts in the background, and thus properly compute the susceptibility difference between the vertebrae or the material, and the external solution. However, to calculate the susceptibility difference between the C1-to-T1 phantom and the external solution, this method was insufficient. Linear gradient correction had to be implemented in addition to visualize some of the expected periodic drop-outs along the spinal canal. As the field variability was high, and the FOV, from C1 to T1, quite large, restricted regions of interest also

had to be defined to apply the linear corrections on restricted FOVs, thus reducing the non-linearity of the variations.

As it is certainly not possible to acquire a reference background by removing the vertebrae in vivo, it would have been preferable for this final phantom not to require such a correction process in order to better match in vivo conditions. However, given the high variability of the regression results and the significant field variations generated by the background, this process was necessary in order to compare the field generated by the vertebrae to the simulation on the two-color mask, which neglected the impact of the background. If a high-quality quantitative simulation taking into account the air and the shell, as described in **Section 5.7.1.1**, could be performed, then it would no longer be necessary to acquire a reference background.

5.7.1.3 Susceptibility

The main aim of this thesis was to create a phantom of the cervical column matching the in vivo susceptibility difference between vertebrae and tissues. As both the spine and its surrounding tissues are complex and non-uniform mixtures, with nonconstant susceptibility, the first difficulty was to define which value to define as the average target susceptibility. The paper from Schenck (1996) was chosen as a reference, as it gives an averaged susceptibility value for tissues and bones, and thus a target value $\Delta\chi = \chi_{\text{cortical bone}} - \chi_{\text{soft tissues}} = +0.19$ ppm. However, these values may not be exactly identical for vertebral bones, and a more precise determination of the matching susceptibility difference could be an advantage in the future. Moreover, this value is likely to vary between patients and across different age groups. Thus, in this thesis, a susceptibility difference value ranging from +0.18 to +0.25 was targeted.

Throughout the different phantoms constructed during this thesis, we gradually approached the desired value of susceptibility difference. The first phantom, composed of C3 to C5 vertebrae printed in Standard White Resin within a saline solution, already had the right susceptibility difference, with the sign inverted. Keeping this sign inversion was undesirable for the subsequent steps of developing the phantom, when the impact of air would be considered, as explained in **Section 5.3**. The discovery of the diamagnetic effect of sugar in water enabled the construction of a second phantom modeling the C3 to C5 vertebrae, matching the desired vertebrae/tissues susceptibility difference with a value of +0.23 ppm. Thus, this second phantom already demonstrated the feasibility of reproducing realistic B_0 field patterns from the spine using a 3D printed model. In the final cervical phantom, the determination of the susceptibility was complicated by the artifacts generated by the outer shell, and the computed susceptibility difference value varied a lot with the selected region of interest, from 0.07 to 0.13 ppm in average. These values are lower than expected, as the susceptibility difference between nylon and water was found to be +0.15 by computing it on the nylon sample in **Section 4.1.2.2**. Considering the fact that adding sugar reduces the susceptibility of water, it was expected that the susceptibility difference between the nylon vertebrae and the final sugary solution would be closer to +0.25 to +0.30.

As the strength of the artifacts generated by the vertebrae is not much higher than the systematic effects from the gradient field, the linear regression between acquired and simulated data had to be restricted to the strict spinal canal to reduce the additional and unwanted noise of the voxels far from the vertebrae.

5.7.1.4 Z-Gradients

Z-gradients appeared to be a very useful way to remove the large field variations in the background, thus allowing revealing more clearly the susceptibility artifacts generated by the vertebrae themselves. Indeed, two types of unwanted artifacts blurred the acquired FMs, systematic effects from the background field, on which the z-gradients were useless, and larger field variations generated by the shell and the external air. Computing the z-gradients could nearly completely eliminate these final artifacts because their scale was far larger than that of a single pixel.

5.7.2 Multi-echo GRE

A Multi-echo 2D GRE was acquired for all the studied phantoms and tuning solutions. Various transversal sections of the vertebral phantoms were compared to in vivo reference images, and the T_2^* of the solutions were computed by exponential fits between the echoes.

5.7.2.1 Visualization of the Images and Comparison to in vivo Artifacts

Patterns of signal drop-outs similar to in vivo acquisitions appeared along the rim of the spinal canal for all three phantoms. The slices placed at junctions between two vertebrae showed the largest signal loss, notably along the posterior side, resembling the in vivo inter-vertebra slices, while in contrast, the slices from the middle of a vertebra got substantially less signal loss, although marginally along the anterior left and right corners. In the final phantom, the influence of the anthropomorphic shell on the signal loss was significant, especially for the first cervical vertebrae, located closer to the back of the neck, as **Fig. 4.23 a)** shows. Indeed, a large signal loss also appeared along the shell. The results of these ME-GRE acquisitions suggest that the geometry of the vertebrae themselves plays a crucial role in the signal decay and artifact generation. Furthermore, with the final phantom, the influence of surrounding tissues and organs, as well as the particular human anatomy, especially in the tight neck region, was highlighted.

It was observed in the study of the second phantom in **Fig. 4.14** and in the analysis of the several tuning solutions in **Section 4.2.2** that the signal loss between the 12 echoes did not follow a perfect exponential decay, some later echoes having a higher magnitude than the previous ones. This could suggest that the dephased spins re-phase partially after some time, and that there might therefore be additional spectral peaks arising from the sugar. It is possible that these peaks could be attributed to the chemical shift of hydrogen in the sugar itself or to water molecules bound to the sugar in the solution.

5.7.2.2 T_2^*

As the first phantom was composed of a solution of salted water, its T_2^* -value was much higher than the chosen TEs of the multi-echo acquisition, making it more difficult to fit an exponential, the decay curve being nearly linear in the acquisition time window. The same issue happened for the measurement of the relaxation times of the several tuning solutions, especially the ones including mouthwashes. In the second phantom, the addition of sugar successfully reduced the transversal relaxation time, allowing a better estimation of it.

The uncertainty and variability of the measured T_2^* of the solution used in the final phantom do not allow a precise estimation of the transverse relaxation time. The addition of the anthropomorphic shell seems to have generated a lot of additional gradients of dephasing, as can be seen in **Fig. 4.24**. The accuracy of the estimated relaxation time of the solution was limited due to the inability to estimate its value inside voxels close to the shell's rim with a satisfactory coefficient of determination. By computing the mean T_2^* value of the solution using the voxels having an associated R^2 greater than a threshold value R_{\min}^2 , the relaxation time T_2^* was estimated to be between 25 and 30 ms, even though these values presented a big standard deviation preventing from a precise estimate. The signal of the voxels in the center of a slice, far from the phantom shell, seems to have much higher relaxation times, between 60 and 100 ms. However, these values are also influenced by the presence of the vertebrae. To get a better value of the relaxation time of the solution, an ME-GRE reference acquisition could also be done to get the value of the final solution only. Based on Peters et al. (2007), a target value $T_2^* \in [20, 45]$ ms would be ideal.

5.8 Innovative Contributions of this Phantom

In this study, a 3D printed anthropomorphic phantom of the cervical spine was built, successfully reproducing some of the susceptibility effects of the B_0 field commonly observed in vivo. To the author's

knowledge, this work is the first 3D printed spinal cord phantom focusing on the reproduction of the susceptibility artifacts (Filippou and Tsoumpas, 2018).

Only few MRI-compatible anthropomorphic phantoms of the spinal cord exist, and even fewer are 3D printed. In Kobe et al. (2019), a phantom of the vertebrae L1 to L5 based on resins and agarose gels successfully reproduced similar relaxation times of the vertebrae as observed in vivo, but did not account for the interaction between the spine and the surrounding tissues. In addition, 3D printing using real CT data allows the building of a more realistic and reproducible phantom. Two 3D printed spine phantoms stand out in the literature. First, Mitsouras et al. (2017) demonstrated the feasibility of using 3D printing materials for building a cervical MRI-visible phantom. Clifton et al. (2019) then compared ex-vivo C3 to C7 vertebrae to a 3D printed model designed by segmentation of CT data in 3D Slicer (Kikinis et al., 2012; Fedorov et al., 2012), similarly as what was done in this thesis. This phantom accurately reproduced the bio-mechanical and anatomical properties of the spine, but was not used in a larger context of the full body, and none of its MR-properties was tested.

The pneumatic phantom created by Tillieux et al. (2018) is the only anthropomorphic cervical phantom really focusing on the influence of the various susceptibilities of the spine and of the tissues on the B_0 field inhomogeneities in spinal cord imaging. Thanks to the combination of an ex vivo human spine and a pneumatic system, this phantom is able to reproduce air variations in the lungs, and therefore mimic both the static and dynamic inhomogeneities. Although our phantom cannot yet take into account the respiratory motion, it presents several advantages over this phantom. Indeed, the final phantom designed in this thesis also successfully reproduce the drop-out patterns observed in vivo, while being more easily preservable than an ex-vivo spine, more flexible to changes and improvements. By printing a human-shaped shell and positioning the vertebrae inside, our final design enhances the complexity and accuracy of our phantom compared to the simple cubic box used as a shell in the pneumatic phantom, by taking into account the complex human shape, and especially the narrowness of the neck. This design also allows for the acquisition of images using the exact cervical coil used in vivo, enabling the testing of sequences under similar conditions to in vivo settings.

We chose to restrict the final phantom, in a first step, to the only model of the vertebrae in a surrounding environment, without taking into account the spinal cord or the intervertebral disks, whereas other published phantoms added an ex-vivo spinal cord (Tillieux et al., 2018) or intervertebral disks and nerve tissues (Kobe et al., 2019). This choice, although restrictive, allowed us to focus on the geometrical susceptibility artifacts generated by the vertebrae inside a homogeneous environment, but the phantom could easily be extended to take into account these components of an in vivo spine, as it is dismountable and adjustable.

By its liquid nature, this phantom allows modularity and can be improved to include dynamic inhomogeneities. However, the choice of a liquid solution also has some disadvantages, such as lower strength, risk of leakage in the MRI, and potential mis-mixing of components, and therefore the appearance of undesired inhomogeneities in the background as observed in **Fig. 4.15 a**).

Future Work

The final phantom exhibited qualitatively similar local B_0 field inhomogeneity as commonly observed in vivo, including similar patterns of signal drop-outs in GRE acquisitions. However, the shell appeared to produce strong background field variations, that could be taken into account in further work, by quantitatively including the shell and the external air in the simulation of the artifacts. That could increase the accuracy of the measured susceptibility difference between the vertebrae and the solution, while allowing a better visual and quantitative prediction of the artifacts, in order to develop more accurate B_0 -shimming techniques.

To study the geometric impact of the shape of the vertebrae, and to start with a simplified model, we have chosen in this master's thesis to restrict the research to the study of 3D printed vertebrae within a tissue modeling environment, thus neglecting the modeling of the intervertebral discs and the spinal cord in itself. The field maps acquired on the phantoms led to signal loss comparable to in vivo imaging. However, in futur work, the phantom accuracy in reproducing the field variations could be quantitatively assessed by comparison with in vivo field maps. To further improve the accuracy, the phantom could then be made more complex by taking into account a greater diversity of spine components. The addition of vertebral discs could for example be the next step, either by printing them, for example in flexible material, or manually by adding a new material.

This phantom was designed to be very flexible and easy to modify. Therefore, we chose to put the vertebrae inside a liquid solution. This was very practical, and will allow further improvements and complexification. Additionally, it presents the opportunity to 3D print vertebrae specific to individual subjects, which could be used to validate the B_0 field against in vivo measurements or to evaluate the impact of different anatomical structures and positioning on the B_0 field. In such cases, it would be preferable to create the vertebral model using MR images, instead of CT images. Nevertheless, once this phantom has achieved its final form, transforming it into a gel phantom could be beneficial to reduce the diffusivity effects (Duan et al., 2014) and increase its solidity. The solidity of the vertebral structure would then become less important, as they would be immobilized by the gel, so the vertebrae could be reprinted with deleting the additional connecting points between the vertebrae, reducing the unwanted artifacts. In a final step, the phantom could also be printed again with a 1:1 scaling, instead of in an 80% size, to increase its realism.

During this master's thesis, we chose to only focus on the static B_0 inhomogeneities around the spinal cord, caused by the variations of susceptibility between the various components of the spine. However, spinal cord imaging also largely suffers from dynamic field inhomogeneities caused by the respiratory motion. As the patient breathes, the volume of air in the lungs changes, causing the field inhomogeneities to vary periodically (Tillieux et al., 2018). This phantom has therefore the potential to be extended to the wider reproduction of inhomogeneities both static and dynamic, in order to reproduce realistically the artifacts observed in vivo, and to be able to really be used for the development of efficient B_0 -shimming methods.

Conclusion

In this work, an anthropomorphic MRI phantom of the human cervical spine was progressively built by 3D printing a model of the C1-to-T1 vertebrae generated from CT images, and positioning them inside a 3D printed human-shaped shell filled with a solution of water, salt, sugar and soap. The phantom exhibited qualitatively similar local B_0 field inhomogeneity as commonly observed in vivo, including similar patterns of signal drop-outs in GRE acquisitions.

The phantom solution was tuned to approximately match both the T_2^* of tissues and the susceptibility difference observed in vivo between the spinal cord and the surrounding tissues. We managed to accurately generate the susceptibility gradients of the vertebrae in solution, and compared them with a field simulation, getting similar periodic drop-out patterns. However, the susceptibility difference between the 3D-printed shell and the solution was higher than expected, leading to strong background field variations.

In future work, the simulations of the artifacts will be extended to take into account the influence of the shell on the B_0 field. In addition, a dynamic system will be installed to represent the air volume variation in the lungs due to respiratory motion. Such an anthropomorphic spine phantom may serve to test new acquisition strategies to tackle the persistent challenges of both static and dynamic B_0 field distortion in spinal cord imaging. Moreover, the phantom developed in this work already allows for a better understanding of the impact of the vertebral geometry on susceptibility artifacts, and validates the feasibility of building a reproducible, modifiable, nontoxic anthropomorphic phantom by 3D printing that accurately reproduces B_0 field patterns from the spine.

Bibliography

- AMRI, 2016. Dielectric phantom recipe generator. URL: <https://amri.ninds.nih.gov/cgi-bin/phantomrecipe>.
- Aspose, . Free online stl file merger. <https://products.aspose.app/3d/merger/stl>. Accessed: 2023-10-08.
- Baba, Y., Lerch, M.M., Stark, D.D., Tanimoto, A., Kreft, B.P., Zhao, L., Saluja, A.K., Takahashi, M., 1994. Time after excision and temperature alter ex vivo tissue relaxation time measurements. *Journal of Magnetic Resonance Imaging* 4, 647-51. doi:<https://doi.org/10.1002/jmri.1880040504>.
- Barry, R.L., Vannesjo, S.J., By, S., Gore, J.C., Smith, S.A., 2018. Spinal cord mri at 7t. *NeuroImage Elsevier* 168, 437-451. doi:<https://doi.org/10.1016/j.neuroimage.2017.07.003>.
- Bennett, D., 2011. Nacl doping and the conductivity of agar phantoms. *Materials Science and Engineering C31*, 494-98. doi:<https://doi.org/10.1016/j.msec.2010.08.018>.
- Biltema, a. Glass fiber fabric (roving) for epoxy and polyester reinforcement. <https://www.biltema.no/bygg/maling/maletilbehor/glassfibervev/glassfibervev-2000023907>.
- Biltema, b. Laminating epoxy. <https://www.biltema.no/en-no/boat/boat-care/epoxy/laminating-epoxy-2000020523>. Accessed: 2023-05-08.
- Clas Ohlson, . Lampekuppel. <https://www.clasohlson.com/no/Lampekuppel/p/Pr324391000>.
- Clifton, W., Nottmeier, E., Damon, A., Dove, C., Pichelmann, M., 2019. The future of biomechanical spine research: Conception and design of a dynamic 3d printed cervical myelography phantom. *Cureus* 11. doi:<https://doi.org/10.7759/cureus.4591>.
- Czervionke, L.F., Daniels, D.L., Wehrli, F.W., Mark, L.P., Hendrix, L.E., Strandt, J.A., Williams, A.L., Haughton, V.M., 1988. Magnetic susceptibility artifacts in gradient-recalled echo mr imaging,. *American Society of Neuroradiology* , 1149-55.
- Dance, D.R., 2014. *Diagnostic Radiology Physics: A Handbook for Teachers and Students*. IAEA.
- Dassault Systèmes Solidworks Corporation, 2022. Solidworks 2022. URL: <https://www.solidworks.com/>.
- Deshmane, A., Gulani, V., Griswold, M.A., Seiberlich, N., 2012. Parallel mr imaging. *Journal of magnetic resonance imaging* 36, 55-72. doi:<https://doi.org/10.1002/jmri.23639>.

-
- Dogger Schmidt, A., 2022. Modeling Susceptibility-induced Magnetic Field Distortion in the Human Head at 7 Tesla Using a Fourier-based Method. Norwegian University of Science and Technology.
- Douglas, N.H.M., Winfield, J.M., deSouza, N.M., Collins, D.J., Orton, M.R., 2013. Development of a phantom for quality assurance in multi-centre clinical trials with diffusion-weighted mri. *ISMRM* 21, 3114.
- Dr. Mike, 2016. File pack for muscle and skin stl creation tutorial. <https://www.embodi3d.com/files/file/6970-file-pack-for-muscle-and-skin-stl-creation-tutorial/>.
- Duan, Q., Duyn, J.H., Gudino, N., de Zwart, J.A., van Gelderen, P., Sodickson, D.K., Brown, R., 2014. Characterization of a dielectric phantom for high-field magnetic resonance imaging applications. *Medical Physics* 41, 102303. doi:<https://doi.org/10.1118/1.4895823>.
- Durrant, C., Hertzberg, M., Kuchel, P., 2003. Magnetic susceptibility: Further insights into macroscopic and microscopic fields and the sphere of lorentz. *Concepts in Magnetic Resonance Part A* 18A, 72–95. doi:<https://doi.org/10.1002/cmr.a.10067>.
- Décorps, M., 2011. *Imagerie de Résonance Magnétique - Bases physiques et méthodes*. EDP Sciences.
- Elster, A., 2021. Questions and answers in mri. <https://www.mriquestions.com>.
- Fedorov, A., Beichel, R., Kalpathy-Cramer, J., Finet, J., Fillion-Robin, J.C., Pujol, S., Bauer, C., Jennings, D., Fennessy, F., Sonka, M., Buatti, J., Aylward, S., Miller, J.V., Pieper, S., Kikinis, R., 2012. 3d slicer as an image computing platform for the quantitative imaging network. *Magnetic resonance imaging* 30, 1323–41. doi:<https://doi.org/10.1016/j.mri.2012.05.001>.
- Filippou, V., Tsoumpas, C., 2018. Recent advances on the development of phantoms using 3d printing for imaging with ct, mri, pet, spect, and ultrasound. *Medical Physics* 45, 740–60. doi:<https://doi.org/10.1002/mp.13058>.
- Finsterbusch, J., 2014. B_0 inhomogeneities and shimming. *Quantitative MRI of the Spinal Cord* , 68–90doi:<https://doi.org/10.1016/B978-0-12-396973-6.00006-X>.
- Finsterbusch, J., Eippert, F., Büchel, C., 2012. Single, slice-specific z-shim gradient pulses improve t_2^* -weighted imaging of the spinal cord. *NeuroImage* 59, 2307-15. doi:<https://doi.org/10.1016/j.neuroimage.2011.09.038>.
- Formlabs, . Form 3b+: Industrial-quality dental 3d printer. <https://dental.formlabs.com/products/form-3b/>.
- Fortin, M.A., 2021. Fat-water separated T1 mapping with inversion-prepared multi-echo MRI. McGill University.
- HUBS, . Hubs, a protolabs company. URL: <https://www.hubs.com/>.
- Ianniello, C., de Zwart, J.A., Duan, Q., Deniz, C.M., Alon, L., Lee, J.S., Lattanzi, R., Brown, R., 2018. Synthesized tissue-equivalent dielectric phantoms using salt and polyvinylpyrrolidone solutions. *Magnetic Resonance in Medicine* 80, 413–19. doi:<https://doi.org/10.1002/mrm.27005>.
- IKEA, . ÖvermÅtt - food cover, set of 3, silicone multicolor. URL: <https://www.ikea.com/us/en/p/oevermaett-food-cover-set-of-3-silicone-multicolor-80417311/>.
- Ikemoto, Y., Takao, W., Yoshitomi, K., Ohno, S., Harimoto, T., Kanazawa, S., Shibuya, K., Kuroda, M., Kato, H., 2013. Development of mri phantom equivalent to human tissues for 3.0-t mri. *Medical Physics* 40, 032303. doi:<https://doi.org/10.1118/1.4790023>.
-

-
- Islam, H., Law, C.S.W., Weber, K.A., Mackey, S.C., Glover, G.H., 2019. Dynamic per slice shimming for simultaneous brain and spinal cord fmri. *Magnetic Resonance in Medicine* 81, 825–38. doi:<https://doi.org/10.1002/mrm.27388>.
- Juchem, C., Nixon, T.W., McIntyre, S., Boer, V.O., Rothman, D.L., de Graaf, R.A., 2011. Dynamic multi-coil shimming of the human brain at 7 tesla. *Journal of magnetic resonance* 212, 280-88. doi:<https://doi.org/10.1016/j.jmr.2011.07.005>.
- Kato, H., Kuroda, M., Yoshimura, K., Yoshida, A., Hanamoto, K., Kawasaki, S., Shibuya, K., Kanazawa, S., 2005. Composition of mri phantom equivalent to human tissues: Composition of mri phantom equivalent to human tissues. *Medical Physics* 32, 3199–3208. doi:<https://doi.org/10.1118/1.2047807>.
- Keereman, V., Mollet, P., Fierens, Y., Espana, S., Vandenberghe, S., 2011. Design of a realistic pet-ct-mri phantom. *IEEE Nuclear Science Symposium Conference Record* , 3173–77doi:<https://doi.org/10.1109/NSSMIC.2011.6153651>.
- Kenhub., 2023. Anatomy: Study course. <https://www.kenhub.com/en/start/anatomy>.
- Kikinis, et al., 2012. 3d slicer image computing platform. <https://www.slicer.org/>.
- KindPNG.com, . Nerves of the spine png - gross anatomy of adult spinal cord, transparent png @kindpng.com. https://www.kindpng.com/imgv/TRJmiJx_nerves-of-the-spine-png-gross-anatomy-of/.
- KindPNG.com, 2022. Spinal cord cervical region cross section, hd png download - kindpng. https://www.kindpng.com/imgv/ionmxxmw_spinal-cord-cervical-region-cross-section-hd-png/.
- Kluyver, T., Ragan-Kelley, B., Pérez, F., Granger, B., Bussonnier, M., Frederic, J., Kelley, K., Hamrick, J., Grout, J., Corlay, S., Ivanov, P., Avila, D., Abdalla, S., Willing, C., 2016. Jupyter notebooks – a publishing format for reproducible computational workflows, in: Loizides, F., Schmidt, B. (Eds.), *Positioning and Power in Academic Publishing: Players, Agents and Agendas*, IOS Press. pp. 87 – 90.
- Kobe, A., Zadory, M., Hamie, Q.M., Froehlich, J.M., Klarhöfer, M., Elsässer, T., Pfammatter, T., Guggenberger, R., 2019. Development of an anthropomorphic spine phantom suitable for fusion of mr neurography with interventional flat-panel ct. *European Journal of Radiology* 112, 153–160. URL: <https://www.sciencedirect.com/science/article/pii/S0720048X19300269>, doi:<https://doi.org/10.1016/j.ejrad.2019.01.019>.
- Le Bihan, D., 1985. *Imagerie par résonance magnétique, bases physiques*. Masson.
- Lennie, E., Tsoumpas, C., Sourbron, S., 2021. Multimodal phantoms for clinical pet/mri. *EJNMMI Physics* 8, 8–62. doi:<https://doi.org/10.1186/s40658-021-00408-0>.
- Liebl, H., Schinz, D., Sekuboyina, A., Malagutti, L., Löffler, M.T., Bayat, A., El Hussein, M., Tetteh, G., Grau, K., Niederreiter, E., Baum, T., Wiestler, B., Menze, B., Braren, R., Zimmer, C., Kirschke, J.S., 2021. A computed tomography vertebral segmentation dataset with anatomical variations and multi-vendor scanner data. *Scientific Data* 8, 284. doi:<https://doi.org/10.1038/s41597-021-01060-0>.
- Lopez-Rioz, N., Cohen-Adad, J., 2023. Phantom-spinoza. <https://github.com/neuropoly/phantom-spinoza>.
-

-
- Löffler, M.T., Sekuboyina, A., Jacob, A., Grau, A.L., Scharf, A., El Hussein, M., Kallweit, M., Zimmer, C., Baum, T., Kirschke, J.S., 2020. A vertebral segmentation dataset with fracture grading. *Radiology: Artificial Intelligence* 2, e190138. doi:<https://doi.org/10.1148/ryai.2020190138>.
- Markl, M., Leupold, J., 2012. Gradient echo imaging. *Journal of Magnetic Resonance Imaging* 35 , 1274–89doi:<https://doi.org/10.1002/jmri.23638>.
- Marques, J., Bowtell, R., 2005. Application of a fourier-based method for rapid calculation of field inhomogeneity due to spatial variation of magnetic susceptibility. *Concepts in Magnetic Resonance Part B: Magnetic Resonance Engineering* 25B, 65–78. doi:<https://doi.org/10.1002/cmrb.20034>.
- Martin, P., Bender, B. and Focke, N.K., 2015. Post-processing of structural mri for individualized diagnostics. *Quantitative Imaging in Medicine and Surgery* 5, 188–203. doi:<https://doi.org/10.3978/j.issn.2223-4292.2015.01.10>.
- McRobbie, D.W., Moore, E.A., Graves, M.J., Prince, M.R., 2017. *MRI from Picture to Proton*. 3 ed., Cambridge University Press. doi:10.1017/9781107706958.
- Micheau, A., Hoa, D., 2022. e-mri / mri step-by-step, interactive learning on magnetic resonance imaging. <https://www.imaios.com/en/e-mri>.
- Mitsouras, D., Lee, T.C., Liacouras, P., Ionita, C.N., Pietilla, T., Maier, S.E., Mulkern, R.V., 2017. Three-dimensional printing of mri-visible phantoms and mr image-guided therapy simulation. *Magnetic Resonance in Medicine* 77, 613–22. doi:<https://doi.org/10.1002/mrm.26136>.
- Mitsouras, D., Liacouras, P., Imanzadeh, A., Giannopoulos, A.A., Cai, T., Kumamaru, K.K., George, E., Wake, N., Catterson, E.J., Pomahac, B., Ho, V.B., Grant, G.T., Rybicki, F.J., 2015. Medical 3d printing for the radiologist. *Radiographics* 35, 1965–88. doi:<https://doi.org/10.1148/rg.2015140320>.
- Nall, R., 2019. Spinal cord: Anatomy, functions, and injuries. <https://www.medicalnewstoday.com/articles/326984>.
- Nishimura, D., 1996. *Principles of Magnetic Resonance Imaging*. Stanford University.
- NITRO, 2014. Mricrogl v1.2.20220720. URL: <https://www.nitrc.org/projects/mricrogl/>.
- Pan, D., Schmieder, A.H., Wickline, S.A., Lanza, G.M., 2011. Manganese-based mri contrast agents: past, present, and future. *Tetrahedron* 67, 8431–8444. URL: <https://www.sciencedirect.com/science/article/pii/S0040402011011409>, doi:<https://doi.org/10.1016/j.tet.2011.07.076>.
- Peters, A.M., Brookes, M.J., Hoogenraad, F.G., Gowland, P.A., Francis, S.T., Morris, P.G., Bowtell, R., 2007. T_2^* measurements in human brain at 1.5, 3 and 7T. *Magnetic Resonance Imaging* 25, 748–753. URL: <https://www.sciencedirect.com/science/article/pii/S0730725X07001701>, doi:<https://doi.org/10.1016/j.mri.2007.02.014>. proceedings of the International School on Magnetic Resonance and Brain Function.
- Port, J.D., Pomper, M.G., 2000. Quantification and minimization of magnetic susceptibility artifacts on gre images. *Journal of Computer Assisted Tomography* 24, 958–64. doi:<https://doi.org/10.1097/00004728-200011000-00024>.
- PROTOTAL AS, . Prototal as. URL: <https://www.prototal.no/>.
-

-
- Queensland Brain Institute, 2017. The spinal cord. <https://qbi.uq.edu.au/brain/brain-anatomy/spinal-cord>.
- Rai, R., Wang, Y.F., Manton, D., Dong, B., Deshpande, S., Liney, G.P., 2019. Development of multi-purpose 3d printed phantoms for mri. *Physics in Medicine Biology* 64, 075010. URL: <https://dx.doi.org/10.1088/1361-6560/ab0b49>, doi:10.1088/1361-6560/ab0b49.
- Saritas, E.U., Holdsworth, S.J., Bammer, R., 2014. Chapter 2.3 - susceptibility artifacts , 91–105URL: <https://www.sciencedirect.com/science/article/pii/B9780123969736000071>, doi:<https://doi.org/10.1016/B978-0-12-396973-6.00007-1>.
- Schenck, J.F., 1996. The role of magnetic susceptibility in magnetic resonance imaging: Mri magnetic compatibility of the first and second kinds. *Medical Physics* 23 , 815–50doi:<https://doi.org/10.1118/1.597854>.
- Schäfer, A., Wharton, S., Gowland, P., Bowtell, R., 2009. Using magnetic field simulation to study susceptibility-related phase contrast in gradient echo mri. *NeuroImage* 48, 126–137. URL: <https://www.sciencedirect.com/science/article/pii/S1053811909006065>, doi:<https://doi.org/10.1016/j.neuroimage.2009.05.093>.
- Sekuboyina, A., Hussein, M.E., Bayat, A., Löffler, M., Liebl, H., Li, H., Tetteh, G., Kukačka, J., Payer, C., Štern, D., Urschler, M., Chen, M., Cheng, D., Lessmann, N., Hu, Y., Wang, T., Yang, D., Xu, D., Ambellan, F., Kirschke, J.S., 2021. Verse: A vertebrae labelling and segmentation benchmark for multi-detector ct images. *Medical Image Analysis* 73, 102166. doi:<https://doi.org/10.1016/j.media.2021.102166>.
- The MathWorks Inc., 2022. Matlab version: 9.12.0.1956245 (r2022a) update 2. URL: <https://www.mathworks.com>.
- Tillieux, P.D., Topfer, R., Foias, A., Leroux, I., Maâchi, I.E., Leblond, H., Stikov, N., Cohen-Adad, J., 2018. A pneumatic phantom for mimicking respiration-induced artifacts in spinal mri. *Magnetic Resonance in Medicine* 79, 600–6051. doi:<https://doi.org/10.1002/mrm.26679>.
- Wang, I., Alexopoulos, A., 2016. Mri post-processing in pre-surgical evaluation. *Current Opinion in Neurology* 29, 168–74. doi:<https://doi.org/10.1097/WCO.0000000000000305>.
- Weishaupt, D., Köchli, V.D., Marincek, B., 2006. How Does MRI Work? An Introduction to the Physics and Function of Magnetic Resonance Imaging. 2nd ed. Springer.

Appendix

Appendix 1: Codes and Notebooks

The analysis of the different acquisitions made during this master's thesis can be found in the GitHub repository https://github.com/BrunnhildePonsi/Masterthesis_Spine_Phantom.

Appendix 2: Imperfection on the C3 Vertebra

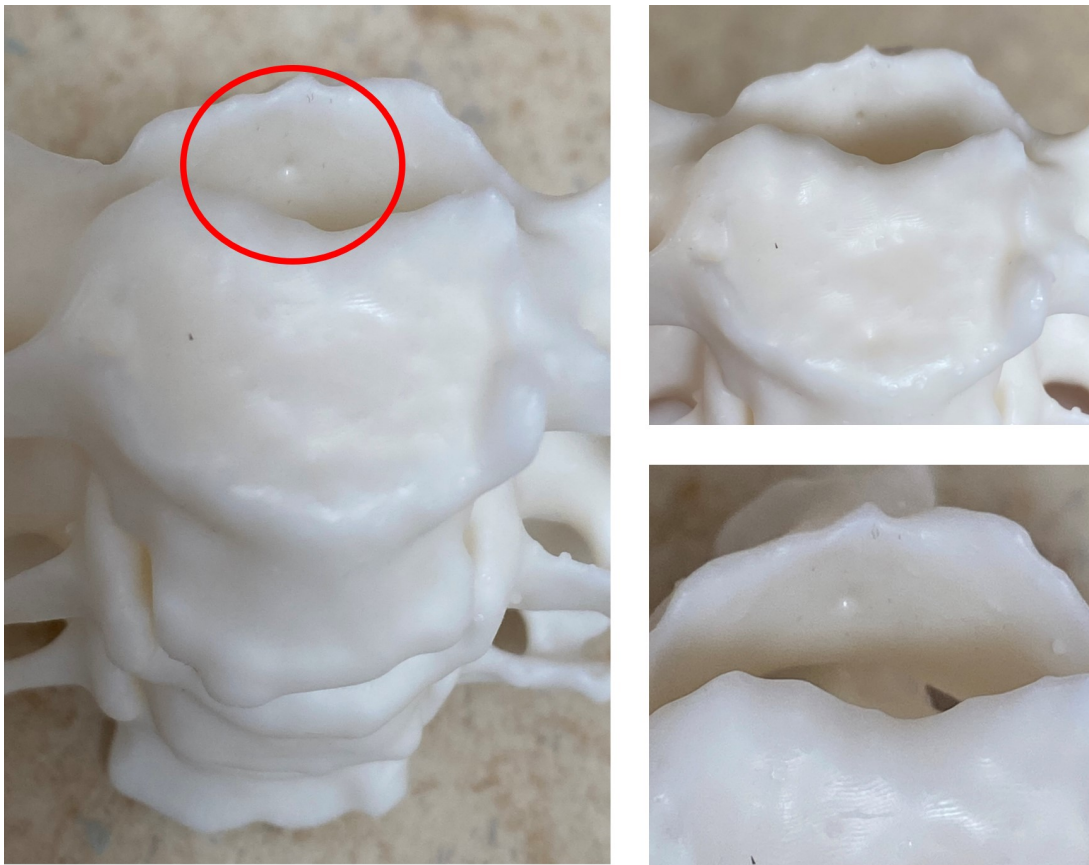
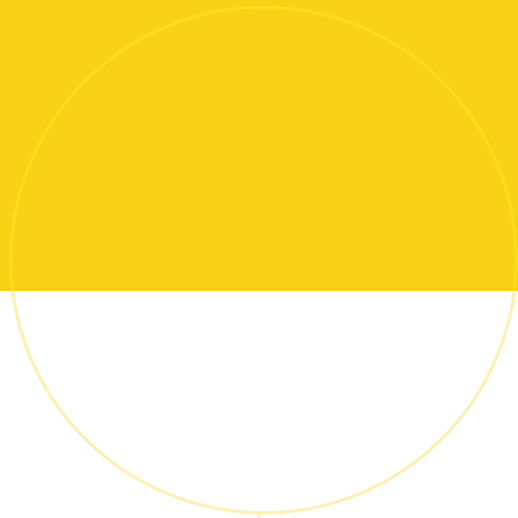


Figure 7.1: A small hole can be observed in the interior, posterior part of the C3 printed vertebrae in Standard White Resin. This imperfection remains sticky even after cleaning the vertebrae, suggesting that an accumulation of sugar is blocked in this area.



 **NTNU**

Norwegian University of
Science and Technology